159 p

(NASA-CR-199120) NUMERICAL THERMAL ANALYSES OF HEAT EXCHANGERS FOR THE STIRLING ENGINE APPLICATION (Cleveland State Univ.) 159 p

N95-33398

Unclas

G3/34 0063066

```
                    MANAGEMENT: DOCUMENT STATUS SCREEN

DOC NUMBER  63066        FILE: 1N     ACCESSION: 9533398     ISSUE: 12

      HAS BEEN IN IPS SINCE 19950825 (FOR 32  DAYS)
      IT HAS BEEN IN THE PUBQ QUEUE SINCE 19950925 AT 638
      SUBQUEUE OWNER IS                  SINCE 0         AT 0

  -------------------------------------------------------------------
 |            LAST ACTION BY CEL          ON 19950920     AT 935      |
 |              EVALUATED BY PNF          ON 19950825                 |
 |              CATALOGED BY DMK          ON 19950829                 |
 |           DUPE-CHECKED BY              ON 19950829                 |
 |          ABSTR. ENTERED BY JXP         ON 19950830                 |
 |          ABSTR. INDEXED BY NAH         ON 19950912                 |
 |           QASS REVIEWED BY RAM         ON 19950914                 |
 |          REPRO ADVANCED BY CEL         ON 19950920                 |
  -------------------------------------------------------------------

  SNAP( QUEUE: ____  SUBQUEUE: ________   PROB: _   DOC NR: _______    )
  PF1=HELP; PF3=SELECTION SCREEN
```

NAG3-955

CSU Cleveland State University

University Office of Research and Economic Development

Sponsored Programs and
Research Development
Fenn Tower 1010
1983 East 24th Street
Cleveland, Ohio 44115

Telephone: (216) 687-3630
FAX: (216) 687-9214

July 27, 1995

Ms. Saundra Gage
Administrative Grants Officer, MS 500-309
NASA Lewis Research Center
21000 Brookpark Road
Cleveland, Ohio 44135

Re: Closeout Documents for NAG 3-955

Dear Ms. Gage:

In accordance with the closeout procedures cited in the Research Grant Handbook (NHB 5800.1C), the following closeout documents for NAG 3-955 which expired on March 31, 1995 are submitted:

1) One copy of the Final Summary of Research
2) One copy of the Federal Cash Transaction Report (SF 272)

Appropriate distribution of the Summary of Research will be made to the NASA Technical Monitor and the NASA Center for Aerospace Information Office. Per the delegation letter dated March 16, 1995, the remaining closeout documentation (Summary of Research, New Technology Report, Final Property Inventory, and the Federal Cash Transaction Report) will be forwarded to ONR.

Sincerely,

K Watkins

Kathryn Watkins
Grants Manager

cc: NASA Technical Monitor/Roy Tew/MS 301-2
Principal Investigator/M. Ibrahim
NASA Center for Aerospace Information
CSU/NASA Grant File/ORS # IBR-R3
CSU/NASA Closeout File
CSU Controller's Office/G. Chromik
ONR/Todd Frye

NASA-CR-199120

NAG3-955

NUMERICAL THERMAL ANALYSES OF HEAT EXCHANGERS FOR THE STIRLING ENGINE APPLICATION

6-3-93

FINAL

IN-34-CR

OCIT

63066

p. 159

MOHAN RAJ KANNAPAREDDY

ABSTRACT

The Regenerator, Cooler and Heater for the NASA Space Power Research Engine (SPRE) have been analyzed in detail for laminar, incompressible and oscillatory flow conditions. Each component has been analyzed independently and in detail with the regenerator being modeled as a two-parallel-plates channel with a solid wall. The ends of the channel are exposed to two reservoir maintained at different temperature thus ~~facilitating~~ providing ~~a~~ an axial temperature gradient along the channel. The cooler and heater components have been modeled as circular pipes with isothermal walls. Two different types of thermal boundary conditions have been investigated for the cooler and heater, namely, symmetric and asymmetric temperature inflow. In symmetric temperature inflow the flow enters the channel with the same temperature in throughout the velocity cycle whereas, in asymmetric temperature inflow the flow enters with a different temperature in each half cycle. The study was conducted over a wide range of Maximum Reynolds number (Re_{max}) varying from 75 to 60000, Valensi number (Va) from 2.5 to 800, and relative amplitude of fluid displacement (A_r) from 0.357 to 1.34.

A two dimensional Finite Volume method based on the SIMPLE algorithm was used to solve the governing partial differential equations. Post processing programs were

developed to effectively describe the heat transfer mechanism under oscillatory flows. The computer code was validated by comparing with existing analytical solutions for oscillating flows.

The thermal field have been studied with the help of temperature contour and three dimensional plots. The instantaneous friction factor, wall heat flux and heat transfer coefficient have been examined. It has been concluded that in general, the frictional factor and heat transfer coefficient are higher under oscillatory flow conditions when the Valensi number is high. Also, the thermal efficiency decreases for lower A_r values. Further, the usual steady state definition for the heat transfer coefficient does not seem to be valid.

TABLE OF CONTENTS

Page

ACKNOWLEDGEMENTS

ABSTRACT

TABLE OF CONTENTS

LIST OF FIGURES

LIST OF TABLES

NOMENCLATURE

I. INTRODUCTION 1

1.1 Research Objectives 5

II. LITERATURE REVIEW 7

2.1 Analytical Solutions 9

Two Dimensional Geometries 10

2.2 Numerical Simulations 12

2.3 Experimental Studies 13

III. MATHEMATICAL DESCRIPTION OF THE PHYSICAL PHENOMENON 16

3.1 Governing Equations 16

3.2 Constitutive Relations and Fundamental Assumptions 18

IV. NONDIMENSIONAL PARAMETERS AND BOUNDARY CONDITIONS 24

4.1 Valensi Number 25

4.2 Maximum Reynolds Number 27

4.3 Geometric Similarity Parameters 27

4.4 Derived Similarity/Nondimensional Parameters 28

Relative Amplitude of Fluid Displacement 28

Strouhal Number 29

4.5 Boundary Conditions for the Governing Equations 30

Solid Walls 30

Symmetry Planes 30

Inlet Plane 32

Outlet Plane 32

Solid-Fluid Interface 33

V. NUMERICAL SOLUTION TECHNIQUE 34

5.1 Principle of Finite Volume Method 35

5.2 Control Volume Variable Storage 39

5.3 Integro-Differential Equation 39

5.4 Discretization Scheme 41

First Level Approximations 42

Discretization of Convective Fluxes 43

Discretization of the Diffusive Fluxes 44

Discretization of the Source Terms 44

Discretization of the Time Derivative 45

The Final Form of the Discretization Equation 45

5.5 Solution Algorithm 46

SIMPLE algorithm 46

5.6 Code Modifications for Oscillating Flows 48

VI. OPERATING CONDITIONS AND GEOMETRIC MODELING 50

6.1 Operating Conditions 50

6.2 Geometric Modeling 57

VII. OSCILLATING FLUID FLOW ANALYSIS 58

7.1 Fluid Flow in Parallel-Plates channel and Code Validation 59

Analytical Solution for the Velocity 59

Reformulation of the Analytical Solution 60

Comparison with Numerical Simulation 65

7.2 Comparison with Experimental Data 73

Description of the Experimental Setup 73

Experimental Observations 75

Numerical Results and Comparison 76

Brief Summary 80

7.3 Entrance Effects 81

VIII. OSCILLATING FLOW HEAT TRANSFER 86

8.1 Conjugate Heat Transfer and Code Validation 86

Kurzweg Analysis (Analytical Solution) 87

Numerical Predictions and Comparison 88

8.2 Symmetric Temperature Inflow 93

Temperature Profiles 93

Contour Plots 99

Section Average Temperature 107

Bulk Temperature 110

Wall Heat Flux 114

Heat Transfer Coefficient 118

8.3 Asymmetric Temperature Inflow 124

IX. CONCLUSIONS 134

9.1 Scope for further Research 137

BIBILIOGRAPHY 139

APPENDICES 142

A. Generalized system of P.D.E 143

B. Derivation of Pressure Correction Equation 144

LIST OF FIGURES

Page

Figure 1.1 Cross sectional view of the NASA Stirling Space Power Research Engine. 2

Figure 1.2. A schematic representation of Free-Piston Stirling Engine showing the location of the Heat exchangers and the power and displacer pistons. The heater is located close to the Expansion space and the cooler close to the compression space with the regenerator in between the two 4

Figure 4.1. A typical integration domain with the boundary types. 31

Figure 5.1. Control Volume arrangement and grid numbering. 38

Figure 5.2. Dependent variable control volume storage location for various physical quantities. 40

Figure 6.1. Envelope in which different Stirling Engines operate, together with: i) Criterion for transition from laminar to turbulent flow, ii) Different test cases studied in the present work. 55

Figure 7.1. The geometry for parallel-plates problem (conjugate heat transfer) with the inlet and outlet boundary conditions 61

Figure 7.2. Shear stress and Pressure drop augmentation factors, σ_τ and σ_P respectively plotted versus the Va for oscillating flow between parallel-plates channel 66

Figure 7.3. Shear stress and Pressure drop lead phase angles, ϕ_τ and ϕ_P respectively plotted versus Va for oscillating flow between parallel-plates channel 67

Figure 7.4. Comparison between analytical and numerical velocity profiles at different velocity phase angles for the conjugate heat transfer problem, Case R_1 :Re_{max}=75 and Va=2.5. [Symbols : Analytical-Kurzweg Dotted Lines : Numerical] 69

Figure 7.5. Comparison between analytical and numerical velocity profiles at different velocity phase angles for the conjugate heat transfer problem, Case R_2 :Re_{max}=12000 and Va=400. [Symbols : Analytical-Kurzweg Dotted Lines : Numerical] 70

Figure 7.6. Comparison between Analytical and Numerical normalized Wall shear stress (τ_w) versus the velocity phase angle for Case R_1 : Re_{max} = 75 and Va = 2.5.[Symbol : Analytical Solid Line : Numerical] 71

Figure 7.7. Comparison between Analytical and Numerical normalized Wall shear stress (τ_w) versus the velocity phase angle for Case R_2 : Re_{max} = 12000 and Va = 400. [Symbol : Analytical Solid Line : Numerical] 71

Figure 7.8. Comparison between Analytical and Numerical normalized Pressure Drop ($\Delta P/L$) versus the velocity phase angle for Case R_1 : Re_{max} = 75 and Va = 2.5. [Symbol : Analytical Solid Line : Numerical] 72

Figure 7.9. Comparison between Analytical and Numerical normalized Pressure Drop ($\Delta P/L$) versus the velocity phase angle for Case R_2 : Re_{max} = 12000 and Va = 400. [Symbol : Analytical Solid Line : Numerical] 72

Figure 7.10. Side view of the oscillating flow rig at the University of Minnesota. (Taken from Seume et. al.,1992) 74

Figure 7.11a. Comparison between Experimental and Numerical Moody friction factor plotted versus velocity phase angle at four different axial locations, namely,at x/D = 0.33,16.0,30.0,44.0 respectively . 78

Figure 7.11b. Comparison between Experimental and Numerical Moody friction factor plotted versus velocity phase angle at four different axial locations, namely,at x/D = 0.33,16.0,30.0,44.0 respectively . 78

Figure 7.11c. Comparison between Experimental and Numerical Moody friction factor plotted versus velocity phase angle at four different axial locations, namely,at x/D = 0.33,16.0,30.0,44.0 respectively . 79

Figure 7.11d. Comparison between Experimental and Numerical Moody friction factor plotted versus velocity phase angle at four different axial locations, namely,at x/D = 0.33,16.0,30.0,44.0 respectively . 79

Figure 7.12 Normalized friction factor (C_f) versus the dimensionless axial distance at different velocity phase angles. Case C_2 :: Re_{max} = 30000, Va = 350 and A_r = 0.714 84

Figure 7.13 Normalized friction factor (C_f) versus the dimensionless axial distance at different velocity phase angles. Case C_5 :: Re_{max} = 20000, Va =

400 and A_r = 0.357 84

Figure 7.14 Normalized friction factor (C_f) versus the dimensionless axial distance at different velocity phase angles. Case H_2 :: Re_{max} = 16500, Va = 88 and A_r = 1.34 85

Figure 8.1. Comparison between analytical and numerical temperature profiles at different velocity phase angles for the conjugate heat transfer problem, Case R_1 :Re_{max}=75 and Va=2.5 90

Figure 8.2. Comparison between analytical and numerical temperature profiles at different velocity phase angles for the conjugate heat transfer problem, Case R_2 :Re_{max}=12000 and Va=400 91

Figure 8.3. Geometry for flow inside Circular tube showing the computational domain and Symmetric temperature inflow conditions 96

Figure 8.4. Three-Dimensional normalized temperature plots at different velocity phase angles for symmetric inflow temperature problem. Case C_2 : Re_{max} = 30000 and Va = 350 97

Figure 8.5. Three-Dimensional normalized temperature plots at different velocity phase angles for symmetric inflow temperature problem. Case C_1 : Re_{max} = 15000 and Va = 175 98

Figure 8.6. Three-Dimensional normalized temperature plots at different velocity phase angles for symmetric inflow temperature problem. Case H_2 : Re_{max} = 16500 and Va = 88 100

Figure 8.7. Three-Dimensional normalized temperature plots at different velocity phase angles for symmetric inflow temperature problem. Case C_5 : Re_{max} = 20000 and Va = 400 101

Figure 8.8. Temperature contours at different velocity phase angles for the symmetrical temperature inflow problem: Case C_2 Re_{max} = 30000 and Va = 350 104

Figure 8.9. Temperature contours at different velocity phase angles for the symmetrical temperature inflow problem: Case H_2 Re_{max} = 16500 and Va = 88 105

Figure 8.10. Temperature contours at different velocity phase angles for the symmetrical temperature inflow problem: Case C_5 Re_{max} = 20000 and Va = 400 106

Figure 8.11. Normalized Section averaged temperature (T_a) versus the dimensionless axial distance (x/D_h) at different velocity phase angles. Case C_2 :: $Re_{\max}$= 30000, Va= 350 and A_r= 0.714 108

Figure 8.12. Normalized Section averaged temperature (T_a) versus the dimensionless axial distance (x/D_h) at different velocity phase angles. Case C_5 :: $Re_{\max}$= 20000, Va= 400 and A_r= 0.357 108

Figure 8.13. Normalized Section averaged temperature (T_a) versus the dimensionless axial distance (x/D_h) at different velocity phase angles. Case H_2 :: $Re_{\max}$= 16500, Va= 88 and A_r= 1.34 109

Figure 8.14. Normalized Bulk temperature (T_b) versus the dimensionless axial distance (x/D_h) at different velocity phase angles. Case C_2 :: $Re_{\max}$= 30000, Va= 350 and A_r= 0.714 111

Figure 8.15. Normalized Bulk temperature (T_b) versus the dimensionless axial distance (x/D_h) at different velocity phase angles. Case C_5 :: $Re_{\max}$= 20000, Va= 400 and A_r= 0.357 111

Figure 8.16. Normalized Bulk temperature (T_b) versus the dimensionless axial distance (x/D_h) at different velocity phase angles. Case H_2 :: $Re_{\max}$= 16500, Va= 88 and A_r= 1.34 112

Figure 8.17. Normalized Wall heat flux ($\dot{q}_w''$) versus the dimensionless axial distance (x/D_h) at different velocity phase angles. Case C_2 :: $Re_{\max}$= 30000, Va= 350 and A_r= 0.714 116

Figure 8.18. Normalized Wall heat flux ($\dot{q}_w''$) versus the dimensionless axial distance (x/D_h) at different velocity phase angles. Case C_5 :: $Re_{\max}$= 20000, Va= 400 and A_r= 0.357 116

Figure 8.19. Normalized Wall heat flux ($\dot{q}_w''$) versus the dimensionless axial distance (x/D_h) at different velocity phase angles. Case H_2 :: $Re_{\max}$= 16500, Va= 88 and A_r= 1.34 117

Figure 8.20. Ratio of Numerical Wall heat flux to the correlated wall heat flux versus the dimensionless axial distance (x/D_h) at different velocity phase angles. Case C_2 :: $Re_{\max}$= 30000, Va= 350 and A_r= 0.714 119

Figure 8.21. Ratio of Numerical Wall heat flux to the correlated wall heat flux versus the dimensionless axial distance (x/D_h) at different velocity phase angles. Case C_5 :: $Re_{\max}$= 20000, Va= 400 and A_r= 0.357 119

Figure 8.22. Ratio of Numerical Wall heat flux to the correlated wall heat flux versus the dimensionless axial distance (x/D_h) at different velocity phase angles. Case H_2 :: Re_{max}= 16500, Va= 88 and A_r= 1.34 120

Figure 8.23a. Normalized values for Nusselt's number (Nu), Wall heat flux ($\dot{q}_w''$) and Temperature Difference ($\Delta T = T_a - T_w$) based on the *section average* temperature. Case C_2 :: Re_{max}= 30000, Va= 350 and A_r= 0.714 122

Figure 8.23b. Normalized values for Nusselt's number (Nu), Wall heat flux ($\dot{q}_w''$) and Temperature Difference ($\Delta T = T_b - T_w$) based on the *bulk* temperature. Case C_2 ::Re_{max}= 30000, Va= 350 and A_r= 0.714 122

Figure 8.24a. Normalized values for Nusselt's number (Nu), Wall heat flux ($\dot{q}_w''$) and Temperature Difference ($\Delta T = T_a - T_w$) based on the *section average* temperature. Case H_2 :: Re_{max}= 16500, Va= 88 and A_r= 1.34 123

Figure 8.24b. Normalized values for Nusselt's number (Nu), Wall heat flux ($\dot{q}_w''$) and Temperature Difference ($\Delta T = T_b - T_w$) based on the *bulk* temperature. Case H_2 :: Re_{max}= 16500, Va= 88 and A_r= 1.34 . 123

Figure 8.25. Asymmetrical temperature inflow boundary conditions representation for the heater 126

Figure 8.26a. Three-Dimensional Temperature plots at different velocity phase angles for asymmetric temperature inflow problem. Case CA_2 :: Re_{max}= 30000, Va= 350, A_r= 0.714, T_h =350 °K and T_c =330 °K . . 128

Figure 8.26b. Three-Dimensional Temperature plots at different velocity phase angles for asymmetric temperature inflow problem.[contd.] Case CA_2 :: Re_{max}= 30000, Va= 350, A_r= 0.714, T_h =350 °K and T_c =330°K 129

Figure 8.27a. Three-Dimensional Temperature plots at different velocity phase angles for asymmetric temperature inflow problem. Case HA_2 :: Re_{max}= 16500, Va= 88, A_r= 1.34, T_h =630 °K and T_c =610 °K . . . 132

Figure 8.27b. Three-Dimensional Temperature plots at different velocity phase angles for asymmetric temperature inflow problem.[contd.] Case HA_2 ::Re_{max}= 16500, Va= 88, A_r= 1.34, T_h =630 °K and T_c =610 °K . . . 133

LIST OF TABLES

Page

5.1 Interpretation of ϕ, Γ_ϕ and S_ϕ in the transport eq. (5.1) 36

6.1 Test cases investigated in the present study for fluid flow analysis 54

7.1 Experimental and Numerical operating parameters 75

8.1 Test cases investigated for the conjugate heat transfer 88

8.2 Test cases investigated for symmetric temperature inflow 94

8.3 Test cases investigated for asymmetric temperature inflow 125

NOMENCLATURE

a	Half channel width in the conjugate problem.
A_r	Relative amplitude of fluid motion.
b	Half solid thickness in the conjugate problem.
C_p	Specific Heat of the fluid or solid.
D_h	Hydraulic diameter of the tube or channel.
k	Thermal conductivity.
L	Length of the channel or tube.
Nu	Nusselts's number.
P	Hydrodynamic pressure in the momentum equations.
Pe	Peclet number used in the analytical solution, $=\frac{U_0 a}{\nu} Pr$.
Pr	Prandtl number of the fluid.
$\dot{q}''$	Heat flux.
r	Radial coordinate distance and direction for Axisymmetric cases or, the radius of the tube.
Re_{max}	Reynolds number based on the maximum velocity $[u_{ma}]$.
t	Time [s].
T	Temperature in °K, $T(x,y,t)$ *or* $T(x,r,t)$.
T_a	Section averaged temperature of the fluid, $T_a(x,t)$ $=\frac{\int T\,r\,dr}{\int r\,dr}$.
T_b	Bulk temperature of the fluid weighted by the absolute velocity, $T_b\,(x,t) \quad = \frac{\int \lvert u(r) \rvert\, T\, r dr}{\int \lvert u(r) \rvert\, r\, dr}$.
T_x	Time averaged temperature, $T_x(x,y)$, $= [T_{west} + \gamma\, x]$.
U	Axial velocity in the x coordinate direction, $u\,(x,y,t)$ *or* $u\,(x,r,t)$.
U_0	Representative axial velocity for the analytical solution.
U_{in}	Axial velocity at the inlet, $u_{in}(t)$.
U_{max}	Maximum input velocity in a cycle.
v	Control volume.
V	Normal velocity of the fluid in the y coordinate direction.
Va	Valensi Number.

x	Axial coordinate distance and direction.
y	Normal coordinate distance and direction for Cartesian Coordinate, system.

SUBSCRIPTS

c	Cold end or east side.
h	Based on hydraulic diameter or hot end reservoir.
i	Instantaneous values.
in	Inlet condition.
m	Mean or averaged over the cross-section value.
max	maximum value during the cycle.
fd	based on fully developed flow conditions.
w	At the wall.

SUPERSCRIPTS

$*$	Guessed or lagged quantity.

GREEK SYMBOLS

ω	Angular frequency in rad/sec.
μ	Dynamic viscosity of the fluid.
γ	$= -(\partial T/\partial x) = [T_{west} - T_{east}]/L$,time averaged constant axial temperature-gradient.
ν	Kinematic viscosity of the fluid.
ρ	Density of the fluid.
σ	Ratio of fluid to solid thermal diffusivity, $=(k/\rho C_p)_f/(k/\rho C_p)_s$.
κ	$=k_f/k_s$,ratio of fluid to solid thermal conductivity.
ϵ	$=b/a$,ratio of half solid to half fluid thickness.
λ	Non-dimensional Pressure gradient in the analytical solution, $=\lvert\partial p/\partial x\rvert a^2/\rho u_0 \nu$.
α	Womerseley number used in the analytical solution, $=a\sqrt{\omega/\nu}$.
η	$=y/a$, nondimensional normal direction.

CHAPTER I

INTRODUCTION

The Stirling engine is a efficient power producing device based on the stirling thermodynamic cycle. A few of its distinct features include high efficiency, very long life, high reliability, and low noise. But, the most important feature which makes it a strong candidate for a viable power source in the future is its ability to driven by virtually any power source such as solar energy. Thus it is seen as a ideal power source for remote applications such as space systems and remote terrestrial applications.

The Stirling Technology branch of NASA Lewis Research Center, Cleveland, have been working on developing free-piston Stirling engines for both space and civil applications (high and low power technology). Currently, research is going on to better understand the thermodynamic losses in the NASA SPRE (Space Power Research Engine), such that the efficiency can be maximized. A team from Cleveland State University have been working on two dimensional modelling and analysis of the SPRE

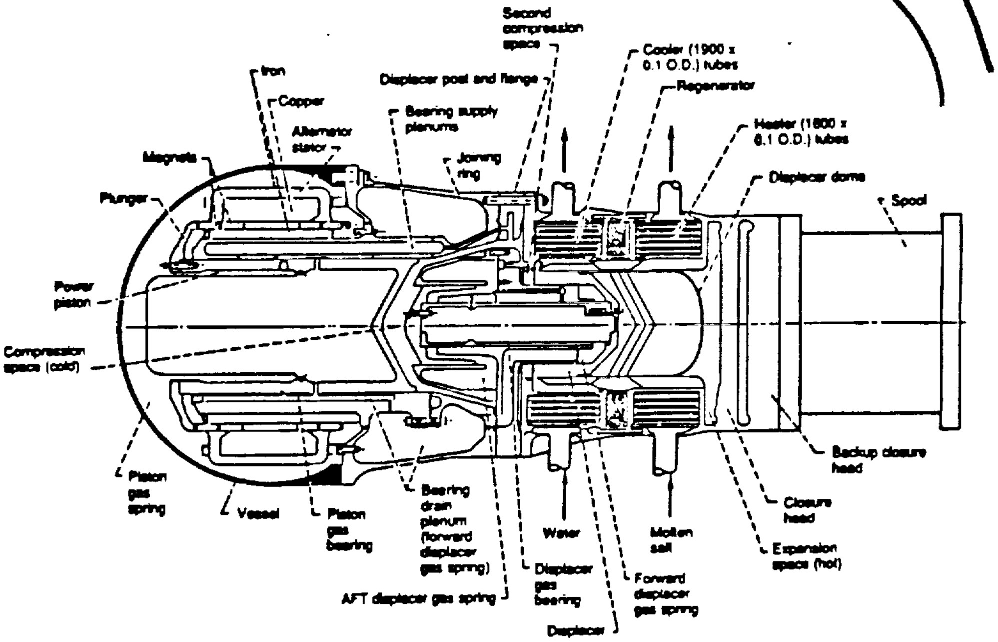

SPRE cross section.

Figure 1.1 Cross sectional view of the NASA Stirling Space Power Research Engine.

heat exchangers to get a feel for the flow and heat transfer phenomenon occurring in the heat exchangers. The thermal analysis of the heat exchangers done in this study is based on the operating conditions of SPRE. Figure 1.1 shows a quarter sectional view of the NASA's SPRE and its various components.

Figure 1.2 is a schematic representation of the major components of the free-piston Stirling showing the basic components and their relative locations. The basic power output of the engine is based on the net work done *on* the piston by the working fluid or gas. The energy inputs include the heat input to the heater for heating the gas. This heat input is reduced by the addition of the regenerator thus making it a highly efficient thermodynamic cycle. The oscillatory motion is achieved by the pressure changes in the piston and displacer gas-springs thereby shuttling the working fluid to and fro from the compression to the expansion space. In the shuttling process the gas absorbs heat energy from the heater part of which is absorbed by the regenerator when the gas is on its way to the cooler. And when the gas flows from the cooler to the heater the regenerator releases this stored energy thereby reducing the net heat input to the cycle or engine.

The location of the heat exchangers between the compression and expansion space results in an oscillatory flow in the heat exchangers. Therefore the design of the heat exchangers (heater, cooler or regenerator) needs to consider the effect of oscillatory flows on the thermal losses. Due to lack of sufficient data and analysis the heat exchangers designers still use unidirectional, steady state correlations for the friction factor and heat transfer coefficient. Since the flow losses and thermal losses work against each other the phenomenon has to be understood to optimize the engine working conditions.

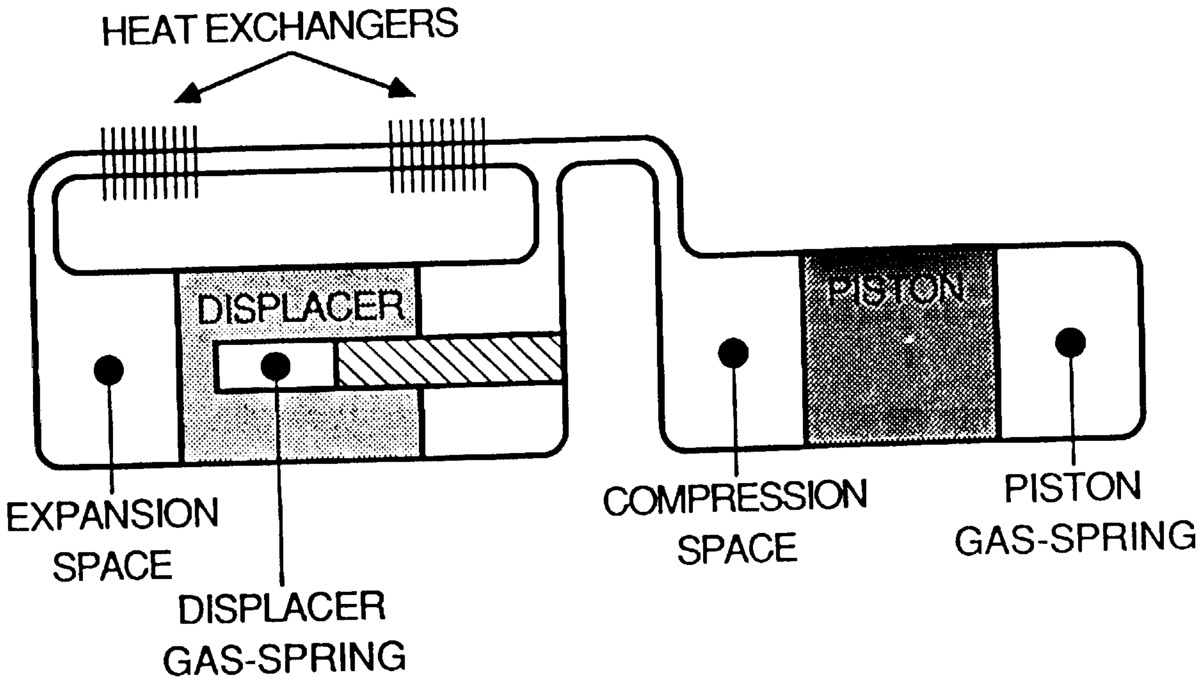

Figure 1.2. A schematic representation of Free-Piston Stirling Engine showing the location of the Heat exchangers and the power and displacer pistons. The heater is located close to the Expansion space and the cooler close to the compression space with the regenerator in between the two.

Some analytical solutions have been derived for the flow between constant area ducts assuming fully developed flows. But the thermal analysis and analytical solution has been restricted to the presence of a linear axial temperature gradient (Kurzweg, 1985a). No thorough analysis has been done on different temperature boundary conditions as present in the Stirling engine heat exchangers.

1.1 Objectives of the research

The present study concerns itself with the time dependent flow and thermal fields in the heat exchangers of the NASA SPRE, namely the, cooler, heater and regenerator. The flow in all the components was assumed to be laminar and incompressible. For the analysis effort was made to model the appropriate geometry for each of the heat exchangers and choose an efficient and reliable numerical method to solve for the governing equations needed for the analysis. Once the flow and thermal fields were established, the study focussed on the behavior of the instantaneous friction factor and heat transfer coefficient with the:

- Maximum Flow Reynolds Number ($Re_{\max}$)
- Valensi Number or dimensionless frequency (Va)
- Relative amplitude of fluid displacement (A_r).

The study was conducted over a wide range of the above mentioned parameters in order to correctly assess the effect of these parameters on the flow and thermal field. Also, different thermal boundary conditions namely, the conjugate heat transfer type, symmetric temperature inflow and asymmetric temperature inflow were also explored under oscillating flow conditions. Special efforts were made to validate the numerical method by comparing the predictions with existing analytical solutions.

CHAPTER II

LITERATURE REVIEW

The aim of this chapter is to synopsize the past work done on oscillatory flows. The survey discusses any analytical solutions and experimental data available on oscillatory flows. Also numerical simulations that have been done on oscillatory flows have been addressed and finally there is a discussion on further investigations that are needed to understand the effects of oscillatory flows.

There are two kinds of unsteady (cyclic) flows that one can find in the literature, pulsatile and oscillatory flows. In pulsatile flows the fluid is set to motion by a sinusoidally varying pressure gradient or velocity which has a *non zero* mean, which means in a complete cycle there exists a net mass transfer across any cross section normal to the primary flow direction. The non zero mean also implies that the primary direction of the inflow does not change in a cycle. Whereas in oscillatory flows the flow is driven by a harmonically varying pressure gradient or velocity that has a *zero* mean. Given the definitions of these two types of unsteady flows one is easily led to conclude that oscillatory flows are a special case of pulsatile flows when the driving pressure gradient or velocity approaches zero mean, which is not true at least mathematically since zero mean flow is a singularity point. This singularity makes the oscillatory flows phenomena a very complex one, although qualitatively one can observe similar behavior between the two kinds od flows. Since the present study concerns itself with only oscillatory flows the review of pulsatile flows has been left out and interested readers can find an extensive review of pulsatile flows in Köhler (1990) and Kwan (1992).

Before the survey is presented a brief description about the meaning of the term "oscillatory flows" in the present context needs to be elaborated. One can find in the literature about oscillatory flows in external flows (see Schlichting) where the flow pattern around a harmonically oscillating body immersed in a fluid are discussed. That situation is different from the one encountered in this study which is mainly concerned with internal flows. The characteristic of oscillatory flows in a internal flow situation is that the periodic driving force has a zero mean for a complete cycle, physically this means in a whole cycle there is no net mass transfer across any cross section perpendicular to the direction of the periodic input. Furthermore, in oscillatory flows because of the zero mean the direction of the flow is actually reversed from one half cycle to the other half cycle.

As the effects of oscillatory flows are completely different from unidirectional flows which means the transition from laminar to turbulent oscillating flow is different.

Many experimental studies have been done on the transition criterion from laminar to turbulent flow in oscillatory flows and a comprehensive review can be found in Seume and Simon (1986a). Only a brief review of the experimental work directly related to the present study will be presented.

2.1 Analytical Solutions

One of the first analytical solution for the oscillatory flow problem was derived by Stokes, who obtained the flow field about an infinite flat wall which executes a sinusoidal motion (See Schlichting) in a stagnant fluid. The effect of the unsteady motion on the flow field was recognized by the presence of what is now known as the Stoke's layer. This layer is a small region close to the wall where the viscous diffusion is concentrated and the region away from it is not effected at all by the motion of the plate. Kurzweg and Chen (1988) did a heat transfer analysis on the above harmonically oscillating plate when it is subjected to a constant axial temperature gradient.

Richardson (1928) in an acoustic experiment measured the velocity distributions across an orifice of circular cross section and he found the peak velocity close to the wall instead of the centerline of the orifice. This was theoretically verified by Sexl(1930) and experimentally corroborated by Richardson and Tyler (1929-30) for the flow produced by the reciprocating motion of a piston. They had mistakenly characterized the velocity peaks as "annular effect" due to the circular geometry. But it has been shown later these velocity shoots near the wall are characteristic of oscillatory flows even in parallel plates situation and not due to any particular geometry.

From the literature surveys it appears that the laminar fully developed oscillatory flows are fairly well documented. The fully developed solutions were derived analytically by using parallel flow assumption and neglecting the initial conditions such that the flow develops into periodically steady state. All the analytical work has been done for constant area ducts and these are reviewed next including relevant numerical simulations and experimental studies.

2.1.1 Two Dimensional Geometries

Uchida (1956) calculated the velocity profiles for laminar incompressible flow in a circular tube subjected to a arbitrarily varying time dependent pressure gradient. He linearized the Navier-Stokes equation by assuming parallel flow thereby dropping the axial diffusion terms and was able to exactly solve the momentum equations by Fourier decomposition of the time dependent pressure gradient term. His paper also appears to be one of the first to distill out practically useful quantities as the wall shear stress.

Kurzweg (1985a,1985b) was one of the first to extend the analysis to include heat transfer for both parallel plate and circular geometry. It is appropriate to mention that all the analytical heat transfer solutions were derived for a thick walled 2D geometry, that is for the conjugated heat transfer problem. Kurzweg's analysis was based on the earlier works of Chatwin (1975), Watson(1983), Joshi et al. (1983) whom found the diffusion of contaminants in gases were greatly enhanced when subjected to flow oscillations. Drawing an analogy for the diffusion of heat Kurzweg was able to arrive at a closed-form solutions for the temperature distribution in the channel. His findings indicate that in oscillatory flows if the fluid entering the channel has different specific enthalpy in one-half period than the other half,then the axial heat transfer is greatly enhanced due to fluid oscillations. This heat transfer is further augmented if the channel wall has a finite thickness as it increases the heat storage/release capability of the wall. Kaviany (1990) and Zhao Ling-de et al. (1991) did a similar analyses for circular tubes with similar qualitative findings and in addition they also verified their theoretical predictions with experiments. It should be mentioned here that this enhanced axial heat diffusion is an undesirable effect for Stirling Engine application as the function of the regenerator (which is sandwiched between the Heater and Cooler maintained at different temperatures) is to minimize the axial transfer of heat from the Heater to Cooler and vice-versa.

Gideon (1986) using a mean parameter approach (average over cross section) technique was able to arrive at practically useful relationships such as friction factor and heat transfer coefficient for the oscillating flow in a channel, but in general the results were not in agreement with the exact solutions. Although the technique proved useful for one dimensional modeling of the flow field in the Stirling Engine Heat Exchangers.

Ozawa and Kawamoto (1991) correlated this enhanced axial diffusion in terms of an effective Nusselt Number for a range of Prandtl numbers (Pr) and Reynolds Number. They observed that for higher Pr the lateral diffusion of heat and momentum penetrated the same distance in other words the fluid behaved as though its Pr was unity for sinusoidal motion of fluid in a pipe. Based on this observation they used a lumped-parameter approach (two layered model) and arrived at a closed-form solution for the heat transfer coefficient also they validated these correlations experimentally.

Kaviany (1986) extended the analytically investigations to include the effects of: (i) viscous dissipation, (ii) channel spacing (height of the channel), and (iii) wall thickness (Solid Thickness).

The above analytical investigations for laminar oscillating flows in constant area two dimensional ducts with parallel flow assumptions can be summarized as follows:

- Additional external work is needed to sustain this type of flow due to higher friction losses as the wall shear stress is augmented.
- When the frequency of oscillation is low the fully developed velocity profile approaches the parabolic shape found in steady, whereas at high frequencies the lateral momentum diffusion is restricted to the Stoke's layer.
- Large quantities of heat can be transported across reservoirs maintained at different temperatures connected by a channel without convective transport of mass (Oscillatory flows).
- There exists a particular frequency when the axial heat transport is maximized.

2.2 Numerical Simulations

Ibrahim et al. (1989,1990) carried out numerical simulations assuming hydrodynamically developed flow and confirmed the analytical findings. Further more the effect of constant temperature boundary conditions on the heat transfer coefficient was also presented. Devalba M. et al. (1991) also simulated the conjugate heat transfer problem under oscillating flow conditions using a finite element code and confirmed the analytical predictions.

Ahn (1990) and Köhler (1990) conducted extensive numerical investigations under turbulent flow conditions utilizing various turbulence models. Their findings indicate that the two equation turbulence models are inadequate to correctly capture the effects of accelerating and decelerating flows. Further turbulent and transition studies in oscillating flows are documented in Koehler's doctoral thesis.

Recently Patankar and Oseid (1992) carried out a two dimensional heat transfer analysis in a pipe under turbulent flow conditions. The boundary conditions were similar to that of the Heater in the Stirling Engine and their study indicates the sensitivity of the Nusselt number (lateral) to the phase shift between the wall heat flux and the bulk temperature.

Hashim (1992) studied the effect of fluid oscillations on the heat transfer and skin friction coefficient for various configurations of backward facing steps. Kwan (1992) investigated the compressibilty effects in a channel for oscillating and pulsatile flows.

2.3 Experimental Studies

A large part of the experimental research has been devoted to study the stability and transition mechanisms of oscillatory flows and can be found in Seume (1988). Seume (1988) carried out a number of experimental runs for different operating parameters in order to understand the transition mechanisms in oscillatory flows and eventually came out with an envelope identifying the laminar and fully turbulent regimes on a $Re_{\max}$ (Reynolds number based on the maximum velocity input and hydraulic diameter) and Va (Valensi number) plot. Friedman (1991) later made detailed 3measurements at a particular operating point and with that database was able to extract useful information about the effect of fluid oscillations on wall bounded flows.

Yuan and Dybbs (1992) experimentally studied and simulated the regenerator of a Stirling engine under oscillatory flow conditions. The study was mainly concentrated on the effect of high frequency and high pressure on the heat transfer coefficient between the working fluid and solid matrix in the regenerator. Their findings indicate oscillation frequency effects both the temperature and heat transfer coefficient while the pressure effects only the heat transfer coefficient. Furthermore the heat transfer coefficient is enhanced significantly compared to that in unidirectional flows.

2.4 Summary

The survey presented above can be summarized as follows:

- Laminar fully developed flows seems to be well understood for oscillatory flows. But the heat transfer analysis has been concentrated mainly on the constant heat flux (boundary condition) problem.
- Currently there seems to no general consensus on the non dimensional parameters to be used especially when it comes to the dimensionless frequency. It has been referred to as Kinetic Reynolds number, Valensi Number and Womersely number. But the trend among the Stirling engine researchers seems to be adopt the definition of Valensi number.
- Because of the fluid oscillations the velocity profile and hence the temperature profile take different shape as compared to unidirectional flow except at low oscillation frequencies.
- In general all the physical quantities such as the pressure,velocities,temperature etc. are out of phase relative to each

significantly alter the friction factor and heat transfer coefficient.

- As far as laminar to turbulence transition is concerned the respective regions are fairly well charted out and documented.

CHAPTER III

MATHEMATICAL DESCRIPTION OF THE PHYSICAL PHENOMENON

In order to quantitatively predict the physical phenomena one needs to describe it in mathematical terms and measurable physical quantities. Once a mathematical description is established (usually in the form of governing equations for the dependent variables) the solution of these equations are sought. An important intermediate step between the description and solution is the nondimensionalization of the governing equations. This not only simplifies the equation and in some instances even reduce the number of dependent variables, but also filters the natural physical parameters effecting the phenomena. The following sections concern themselves with the above issues with particular emphasis on the fundamental assumptions and approximations.

3.1 Governing Equations

Most real life fluid flow phenomena are mathematically represented by the well known Navier-Stokes (N-S) equations which are based on the continuum hypothesis. The N-S equations are a set of nonlinear partial differential equations arrived at by the conservation of transport properties such as mass,momentum and energy for an infinitesimal control volume. In vector notation they are as follows:

Conservation of mass,

$$\frac{\partial \rho}{\partial t} + \nabla.(\rho \vec{u}) = 0 \qquad (3.1)$$

Conservation of momentum,

$$\rho \frac{\partial \vec{u}}{\partial t} + \rho\,(\vec{u} \bullet \nabla)\,\vec{u} = -\nabla p + \nabla \bullet \vec{\vec{\tau}} + \vec{f}_g \qquad (3.2)$$

Conservation of Energy in terms of the enthalpy,

$$\rho \frac{\partial h}{\partial t} + \rho(\vec{u} \bullet \nabla)h = -\nabla \bullet \vec{q} + \left[\frac{\partial p}{\partial t} + (\vec{u} \bullet \nabla)p\right] + \Phi \qquad (3.3)$$

where

$\bullet$: is the divergence operator

∇ : represents the gradient vector operator

ρ : is the density

p : is the thermodynamic pressure

$\vec{u}$: stands for the velocity vector

$\bar{\bar{\tau}}$: is the stress tensor

$\vec{f}_g$: stand for additional body forces

h : is the specific enthalpy of the fluid

$\vec{q}$: is the heat flux vector

Φ : is the dissipation function

The dissipation function is defined as,

$$\Phi = \frac{1}{2}\,\bar{\bar{\tau}} \bullet def(\vec{u}) \tag{3.4}$$

Here $def(\vec{u})$ stands for the rate of deformation tensor and is defined as,

$$def(\vec{u}) = \frac{1}{2}\left[\,\nabla\vec{u} + (\nabla\vec{u})^{*}\,\right] \tag{3.5}$$

The superscript "*" denotes the transpose of a tensorial quantity. Some points to note in the above equations are when the gradient operator (∇) acts on a vector quantity it results in a tensorial quantity. The continuity and energy equations are scalar whereas the conservation of momentum is a vector equation out of which follow three scalar equations (assuming Euclidian space) depending upon the choice of coordinate system. The above set of equations together with the boundary conditions are necessary to solve the problem completely, but they are insufficient as there are more unknowns than the number of equations. The following section wrestles with this problem by invoking some fundamental assumptions and constitutive relations.

3.2 Constitutive Relations And Fundamental Assumptions

The flow field is determined by the velocity $\vec{u}$ and the thermal field by the temperature T, therefore constitutive relations are used to reduce the equations (3.1)-(3.3) in terms of these dependent variables. Firstly the stress tensor $\bar{\bar{\tau}}$ is expressed in terms of the velocity gradients by assuming the working fluid to be Newtonian which along with the Stoke's hypothesis is given by:

$$\bar{\bar{\tau}} = \mu\, def(\vec{u}) - \frac{2}{3}\mu I(\nabla\cdot\vec{u}) \tag{3.6}$$

Here " I " denotes the unit tensor which is like the Kronecker delta in cartesian tensor notation. Substituting the definition of rate of deformation tensor $def(\vec{u})$ in the stress tensor and then taking its divergence the conservation equation of momentum reduces to what is normally called the Navier-Stokes equations:

$$\rho\frac{\partial\vec{u}}{\partial t} + \rho(\vec{u}\cdot\nabla)\vec{u} = -\nabla p + \nabla\cdot[\mu(\nabla\vec{u})] + \nabla\cdot[\mu(\nabla\vec{u})^{*}] + \vec{f}_g - \frac{2}{3}\nabla[\mu(\nabla\cdot\vec{u})] \tag{3.7}$$

Since the present study is not concerned with buoyancy effects the body forces due to gravity is assumed to be negligible and defining the pressure as:

$$P = p + \frac{2}{3}\mu(\nabla\cdot\vec{u}) \tag{3.8}$$

equation (3.2) can be reformulated in the following form:

$$\rho\frac{\partial\vec{u}}{\partial t} + \rho(\vec{u}\cdot\nabla)\vec{u} = -\nabla P + \nabla\cdot[\mu(\nabla\vec{u})] + \nabla\cdot[\mu(\nabla\vec{u})^{*}] \tag{3.9}$$

As far as the conservation of energy equation (eq. 3.3) is concerned the first simplification is done by using the Fourier heat conduction law which gives a relationship between the heat flux vector ($\vec{q}$) and the temperature gradient is:

$$\vec{q} = -k\,[\,\nabla(\,T\,)\,] \tag{3.10}$$

The specific enthalpy of the fluid h is changed to temperature by using the thermodynamic identity:

$$\rho\frac{Dh}{Dt} = \rho c_p\frac{DT}{Dt} + (1-\beta T)\frac{Dp}{Dt} \tag{3.11}$$

where $\frac{D(\,)}{Dt}$ stands for the substantial derivative given by:

$$\frac{D(\,)}{Dt} = \frac{\partial(\,)}{\partial t} + (\vec{u}\bullet\nabla)(\,) \tag{3.12}$$

and β denotes the *bulk expansion coefficient* (or thermal expansion coefficient) defined as:

$$\beta \equiv -\frac{1}{\rho}\left[\frac{\partial\rho}{\partial T}\right]_p \tag{3.13}$$

And it is zero for incompressible *fluids* and $1/T$ for ideal gases. Substituting equations (3.11) and (3.13) in the conservation of energy equation (3.3) and with some algebraic manipulations it reduces to:

$$\rho\, c_p\frac{\partial T}{\partial t} + \rho\, c_p(\vec{u}\bullet\nabla)\,T = \nabla\bullet[k\nabla(\,T\,)\,] + \beta\,T\left[\frac{\partial p}{\partial t} + (\vec{u}\bullet\nabla)p\right] + \Phi \tag{3.14}$$

For an ideal gas the energy equation takes the form of:

$$\rho\, c_p \frac{\partial T}{\partial t} + \rho\, c_p (\vec{u} \bullet \nabla)\, T = \nabla \bullet [\, k \nabla(T)\,] + \left[\frac{\partial p}{\partial t} + (\vec{u} \bullet \nabla) p \right] + \Phi \qquad (3.15)$$

Equations (3.1),(3.7) and (3.15) are sufficient to solve for the flow and thermal field, but there are situations where they can be further simplified by the *type* of flow. In this study two such classes of flows have been studied, namely *incompressible flows* and *thermally expandable flows*. The necessary condition for the establishment of incompressible flows is that the Mach Number is much less than one ($M \ll 1$) and if the temperature gradients are low in the domain considered the fluid properties (ρ, μ, β, k, c_p) are constant. Under this situation the continuity and momentum equations are greatly simplified with lot of terms dropping out such as $\partial\rho / \partial t$ in eq. (3.1) and $\nabla \bullet [\, \mu (\nabla \vec{u})^{*}\,]$ in eq. (3.9). An important implication of this is that the continuity and momentum equations are decoupled from the energy equation, hence can be solved independently for the velocity field without worrying about the thermal effects.

When there exists substantial temperature gradients in the domain at low Mach numbers then the fluid properties are no longer constant and vary with temperature (only). Such low speed compressible flows are called *thermally expandable flows* or *anelastic flows*. It usually implies the density of the working fluid varies only as a result of isobaric thermal expansion; in effect removing any *acoustic* phenomena from theoretical considerations. Under this situation no terms in equations (3.1) and (3.7) drop out unlike in the incompressible flow situation and further the energy equation now is coupled with momentum equations now due to temperature dependent fluid properties.

If the Mach number is low ($M \ll 1$) an interesting formulation for the energy equation (eq. 3.15) results, the second term on the right hand side of eq. (3.15) and the viscous dissipation function (Φ) becomes negligible and they drop out of the equation. Then the energy equation is reduced to:

$$\rho c_p \frac{\partial T}{\partial t} + \rho c_p (\vec{u} \cdot \nabla) T = \nabla \cdot [k \nabla (T)] \qquad (3.16)$$

The above equation states that the energy equation in low speed flows is strictly a balance between the convective and diffusive (conduction) processes. It should be noted that the above formulation is the same for both *incompressible flow* and *anelastic* or *thermally expandable flow*, but with the difference that in the former type of flow the energy equation is *uncoupled* from the other the conservation equations, whereas in the latter type of flow all the equations are coupled together and therefore must be solved simultaneously. In the Stirling engine heat exchangers the flow speeds are very low compared to the speed of sound (i.e low Mach number) and the above formulation for the energy equation suffices.

Equations (3.1),(3.7) and (3.15) provide four equations for the four dependent variables U, V, P and T for a two dimensional cartesian or axisymmetric coordinate system. These equations are listed in the Appendix A in one generalized formulation. The complete set of partial differential equations as described in Appendix B together with the boundary conditions are necessary and sufficient to describe the fluid flow and heat transfer in oscillatory flows. The basic assumptions used to derive the theoretical equations are summarized as follows:

- The fluid is a continuum.

- Newtonian Fluid.

- Stoke's hypothesis.

- Low Mach number.

- No body forces or gravitational effects.

- Axisymmetric or two dimensional geometry.

- Fourier heat conduction law.

- No internal heat sources. - No radiation heat transfer.

CHAPTER IV

NONDIMENSIONAL PARAMETERS AND BOUNDARY CONDITIONS

Nondimensionalization of the physical problem is one of the most important steps in the solution process of the governing equations. The nondimensional variables which arise from this process not only simplify the problem but also serve to reveal key physical aspects of the phenomena. Also normalization of the physical problem provides the natural scales for the problem as dictated by the boundary conditions, physical constants, and geometry. A dimensional analysis of the governing equations has not been presented in this report although the various nondimensional variables are described in detail along with their physical significance.

As mentioned earlier (Chapter II) in this report there seems to be no consensus on the standardization of the dimensionless frequency in oscillatory flows and this is highly desirable in order to correctly interpret the results and for future reference. It is the aim of this chapter to clearly group the nondimensional parameters for oscillatory flows found in the literature and physically interpret them so as to make a case for consistent usage in the future.

4.1 Valensi Number (Va)

There are the three different nomenclatures one comes across in the literature for the dimensionless frequency in oscillatory flows. This nondimensional variable is the natural outcome of oscillatory flows equations due to the presence of the unsteady term in the Navier-Stokes equations. To be precise, it weighs the strength of the time derivative term in the governing equations just as the Reynolds numbers weighs the relative strengths of the convection and diffusion terms. The three definitions of the above variable are as follows:-

Valensi number,

$$Va = \frac{\omega \ (\frac{D_h}{2})^2}{\nu} \tag{4.1}$$

Kinetic Reynolds number,

$$Re_\omega = \frac{\omega \ . \ (\frac{D_h}{2})^2}{\nu} \tag{4.2}$$

Womersely number,

$$\alpha = (\frac{D_h}{2}) \ . \sqrt{\frac{\omega}{\nu}} \tag{4.3}$$

It should be mentioned that Kurzweg (1985a) with whose results the present numerical simulations are compared with has used $D_h/4$ in the definition of Womersely number instead of $D_h/2$ in his investigations of oscillatory flows in a parallel plate channel.

From the above definitions of the Valensi number (Va) and Kinetic Reynolds number (Re_ω) it is shown that they are the same but differ in the vocabulary. The motivation to define it as the Kinetic Reynolds number (Re_ω) can be traced to its similarity in structure with the well known definition of Reynolds number. The Valensi number can be physically interpreted as the ratio of viscous diffusion time scale ($D_h^2/4\nu$) to the oscillation period ($1/\omega$). When the Va is low implies $1/\omega \to \infty$ or the viscous diffusion is fast relative to the oscillation frequency and the velocity profile approaches the familiar parabolic shape as seen in steady flows. For higher Va due to high frequency the viscous effects do not have the time to diffuse across the duct before the convected fluid arrives, hence instead of the parabolic profile one sees the presence of a small Stokes layer near the wall where the viscous effects are concentrated.

The Womersely number (α) on the other hand gives a very geometrical interpretation, it is the ratio of the width of the duct ($D_h/2$) to the viscous penetration depth $\sqrt{\nu/\omega}$.

Despite the various meaningful definitions for the dimensional frequency, the definition of Valensi Number (Va) has been adopted by the Stirling Engine researchers and this definition will be used throughout this report.

4.2 Maximum Reynolds Number ($Re_{\max}$)

Maximum Reynolds Number is the second similarity parameter or the dimensionless variable which arises out the normalization of the governing equations. For oscillating flows it is defined as follows:

$$Re_{\max} = \frac{\rho U_{\max} D_h}{\mu} \tag{4.4}$$

The velocity is scaled by the maximum velocity amplitude ($U_{\max}$) instead of the mean velocity since the mean velocity is zero in oscillatory flows.

The Maximum Reynolds Number ($Re_{\max}$) and Valensi Number (Va) together make up the dynamic similarity parameters for two dimensional oscillatory flows.

4.3 Geometric Similarity Parameters

This similarity parameters arise when the length scales are normalized as dictated by the geometry of the problem. Since this work concerns itself with plane flows or two dimensional geometries. The axial length (L) of the Heat Exchangers are normalized with the Hydraulic diameter (D_h). Therefore the dimensionless axial length which reveals itself after the normalization is L/D_h .

4.4 Derived Similarity Or Nondimensional Parameters

In oscillatory flows it is not unusual to find in the literature additional nondimensional variables, derived from the fundamental variables described above.

4.4.1 Relative Amplitude of Fluid Displacement (A_r)

Relative amplitude of fluid displacement (A_r) is one such derived parameter and it is defined as the maximum axial fluid displacement during one cycle divided by the length of the duct. Essentially, it states how far the fluid is pushed into the duct compared to the axial length of the duct for one oscillation period (if the fluid oscillated inviscidly).

$$A_r = \frac{2\ X_{max}}{L} \tag{4.5}$$

Under the plug flow assumption (uniform velocity across the cross section of the duct), the A_r values indicate three different physical situations for a cycle:

$A_r < 1$	Some fluid does not leave the heat exchanger referred to as "dead Volume" by some researchers.
$A_r = 1$	All the fluid initially in the heat exchanger moves the length of the channel in a oscillation cycle.
$A_r > 1$	All of the fluid initially contained in the channel, at any time during the cycle, is outside of the channel at some other time during the cycle.

From a different perspective A_r indicates the volume of fluid displaced in one-half cycle divided by the total volume of fluid contained in the duct. Since it is an geometric similarity parameter it plays an important role in characterizing entrance effects.

4.4.2 Strouhal Number (Str)

Strouhal number is another derived parameter widely used in external flows as a nondimensional parameter for the frequency of vortex shedding. Analogously for internal oscillatory flows the frequency of fluid oscillation $\bar{\omega}$ is scaled by the U_{max}/D_h to arrive at Strouhal number (Str):

$$Str = \frac{\omega}{\left(\frac{U_{max}}{D_h}\right)} \tag{4.6}$$

By a little algebraic manipulations it can be shown that the Strouhal number is not an independent dimensionless parameter and relates the Valensi number (Va) and Maximum Reynolds number (Re_{max}) by the equation,

$$Str = \frac{4\ Va}{Re_{max}} \tag{4.7}$$

Earlier Stirling Engine Heat exchangers were designed and operated based on the Str and Re_{max} values.

4.5 Boundary Conditions For The Governing Equations

The governing equations presented above mathematically describe a whole class of fluid flow problems, the way problems are differentiated from one another are by the application of boundary conditions. Since the equations are solved in a finite domain the boundary conditions for each of dependent variable needs to be specified along the boundaries of the domain. For the present situation four different types of boundary conditions were used to close the problem. All the boundary conditions for the particular boundary is based on the Figure 4.1.

4.5.1 Solid Walls

Along the walls by virtue of no-slip, the fluid velocity is zero assuming the walls are impermeable. For the energy equation the walls can either be maintained at constant temperature or be a source of constant heat flux. Mathematically this can be expressed as,

$$U_{wall} = V_{wall} = 0,\ T = T_{wall} \quad OR \quad -k\frac{\partial T}{\partial n})_{wall} = Q_{wall} \tag{4.8}$$

where the partial derivative w.r.t n implies gradient normal to the wall.

4.5.2 Symmetry Planes

On symmetry planes or axis of symmetry the normal gradient of the tangential velocity and the normal velocity are zero as far as the momentum equations are

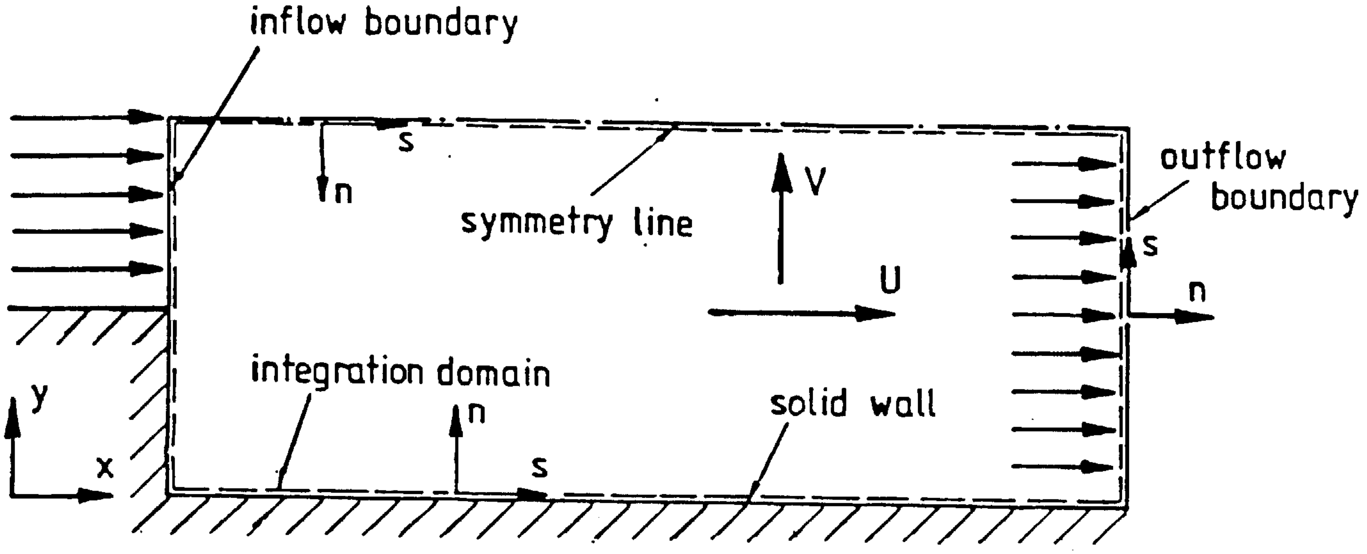

Figure 4.1. A typical integration domain with the boundary types.

concerned. By symmetry the normal gradient of the temperature is also zero for the energy equation, physically this implies the symmetry plane behaves as an adiabatic wall. These can be formulated for the plane shown in figure 4.1 as:

$$\frac{\partial U}{\partial y} = V = \frac{\partial T}{\partial y} = 0 \tag{4.9}$$

4.5.3 Inlet Plane

On the inlet planes mathematically the boundary conditions are of Dirichlet type i.e. values of the dependent variables are specified. Thus

$$\begin{aligned} U_{in} &= U_{\max} Sin(\omega t) \\ V_{in} &= 0 \\ T &= T_{in} \end{aligned} \tag{4.10}$$

It should be noted that the above equations are based on the inlet plane as shown in Fig. 4.1. The *U* velocity is time dependent and varying sinusoidally whereas the temperature is fixed w.r.t time.

4.5.4 Outlet Plane

At the outlet plane one does not know the boundary conditions *apriori* the normal practice is to keep the domain long enough such that the diffusive fluxes are negligible normal to the plane. Additional physical constraint for the momentum equations is derived by observing that for incompressible flows the mass fluxes are conserved. The mathematical formulation for the boundary conditions are:

$$\frac{\partial U}{\partial x} = \frac{\partial V}{\partial x} = \frac{\partial T}{\partial x} = 0 \tag{4.11}$$

For oscillating flows the inlet and outlet plane are reversed after each half cycle due to the zero mean flow restriction. For instance if the cycle begins with the flow entering from the East side after half period the flow enters from the west side.

4.5.5 Solid-Fluid Interface

This boundary condition is needed in the conjugate heat transfer problem, where there is an interaction between the fluid within the channel and the surrounding solid region. At a solid-fluid interface the heat flux across the interface is conserved by energy conservation principle and the temperature is continuous. These two boundary conditions have been implicitly implemented in the code since the solid-fluid domain has been solved together.

CHAPTER V

NUMERICAL SOLUTION TECHNIQUE

The governing partial differential equations (PDEs) which are generally elliptic in nature, are not tractable to analytical solving procedures.They are numerically integrated by one of the many discretization procedures. In this chapter,the solution methodology is discussed.

Currently, there are numerous methods and ways to solve the partial differential equations arising in fluid mechanics, some of the existing popular and fairly standard methods are based on one of the following discretization schemes:

i) Finite Volume Methods (FVM)
ii) Finite Element Methods (FEM)
iii) Finite Difference Methods (FDM)

The underlying principle behind all these methods are one and the same, which is dividing the domain into smaller subdomains and thereby reduce the partial differential equations into a set of linearized algebraic equations. The differences among the methods arise from the way these algebraic equations are arrived at from the original PDEs. Since no single method has till now been proven to be superior to the other, the finite volume method (FVM) has been chosen in this study. One of the distinct advantages of the finite volume method is that it lends itself naturally to the PDEs arising in fluid mechanics problems.

The code developed to solve the governing equations is based on the research code called C.A.S.T (Computer Aided Simulation of Turbulent Flows) developed by Peric and Scheuerer (See Peric et al.). The original code limited in its ability to handle variety of thermal and time dependent boundary conditions has been broadened to include these type of flows. Further the numerical formulation of the energy equation has been revised to handle conjugate heat transfer problem such as that occurring in the regenerator of the Stirling engine. The objective of the following description is (i) to briefly describe the discretization technique (ii) solution technique employed to solve the algebraic equations and (iii) discuss the convergence criterion employed.

5.1 Principle Of Finite Volume Method

The finite volume method in general is based on the conservative property of the partial differential equations (PDEs) since the equations which themselves are derived from the conservation of certain physical quantities. This important attribute of the equations makes it possible to collapse all the individual equations into a generalized transport equation, thus facilitating one common algorithm for all the PDEs. Therefore for any generalized scalar variable ϕ the transport equation can be written as:

$$\frac{\partial(\rho\phi)}{\partial t} + \frac{\partial}{\partial x}(\rho U\phi - \Gamma_\phi \frac{\partial\phi}{\partial x}) + \frac{1}{r^n}\frac{\partial}{\partial r}(\rho r^n V\phi - \Gamma_\phi \frac{\partial\phi}{\partial r}) = S_\phi \qquad (5.1)$$

Here the value of n determines the type of axes system used, when $n = 0$ then the transport equation reduces to the cartesian coordinate system with the independent variable r being changed to the more familiar y. And, when $n = 1$ the equation represents the transport equation for a axisymmetric coordinate system. All the individual differential equations for each conservation equation (e.g. mass,momentum) can be recovered from equation (5.1) by choosing appropriate physical quantity for ϕ, Γ_ϕ and S_ϕ which are given in Table 5.1 below:

Table 5.1: Interpretation of ϕ ,Γ_ϕ and S_ϕ in the transport eq. (5.1)

Equation	ϕ	Γ_ϕ	S_ϕ
Continuity	1	0	0
x-Momentum	U	μ	$-\frac{\partial P}{\partial x} + \frac{\partial}{\partial x}(\mu\frac{\partial U}{\partial x}) + \frac{1}{r^n}\frac{\partial}{\partial x}(\mu r^n \frac{\partial V}{\partial x})$
r-Momentum	V	μ	$-\frac{\partial P}{\partial r} + \frac{\partial}{\partial x}(\mu\frac{\partial U}{\partial r}) + \frac{1}{r^n}\frac{\partial}{\partial r}(\mu r^n \frac{\partial V}{\partial r}) - n\cdot(\frac{2\mu V}{r^2})$
Energy	$C_p T$	k	0

The general discretizing procedure for the transport equation given in eq. (5.1) is as follows. In the first step, the computational domain is divided into small rectangular control volumes. The grid points where the dependent variables are solved for lie at the geometric centre of the control volume. Then the transport equation 5.1 is integrated over each control volume. By applying Gauss's theorem to the integral equation results in a integro-differential equation. Physically the integro-differential equation is a relation between the net increase of the considered quantity per unit time, the total net convective and diffusive *fluxes* across the control volume boundaries and the source (or sink) terms within the control volume. This integro-differential equation is then discretized with some assumptions and linearization to arrive at the linear algebraic equation for the control volume. If the above process is repeated for all the control volumes one arrives at a set of linear algebraic equations for the transport equation 5.1. The natural appearance of the fluxes at the control volume faces makes the whole scheme globally conservative. These set of equations are then solved to give the values of the considered quantity at the grid point locations. Special coupling algorithm is used to link all the sets of algebraic equations for a given physical quantity. A brief outline of the above described is as follows for a detailed explanation the reader is referred to Perić and Scheuerer (1989).

The outline will be presented with reference to the Cartesian coordinate system, which means in the transport equation (5.1) $n=0$ and $r=y$.

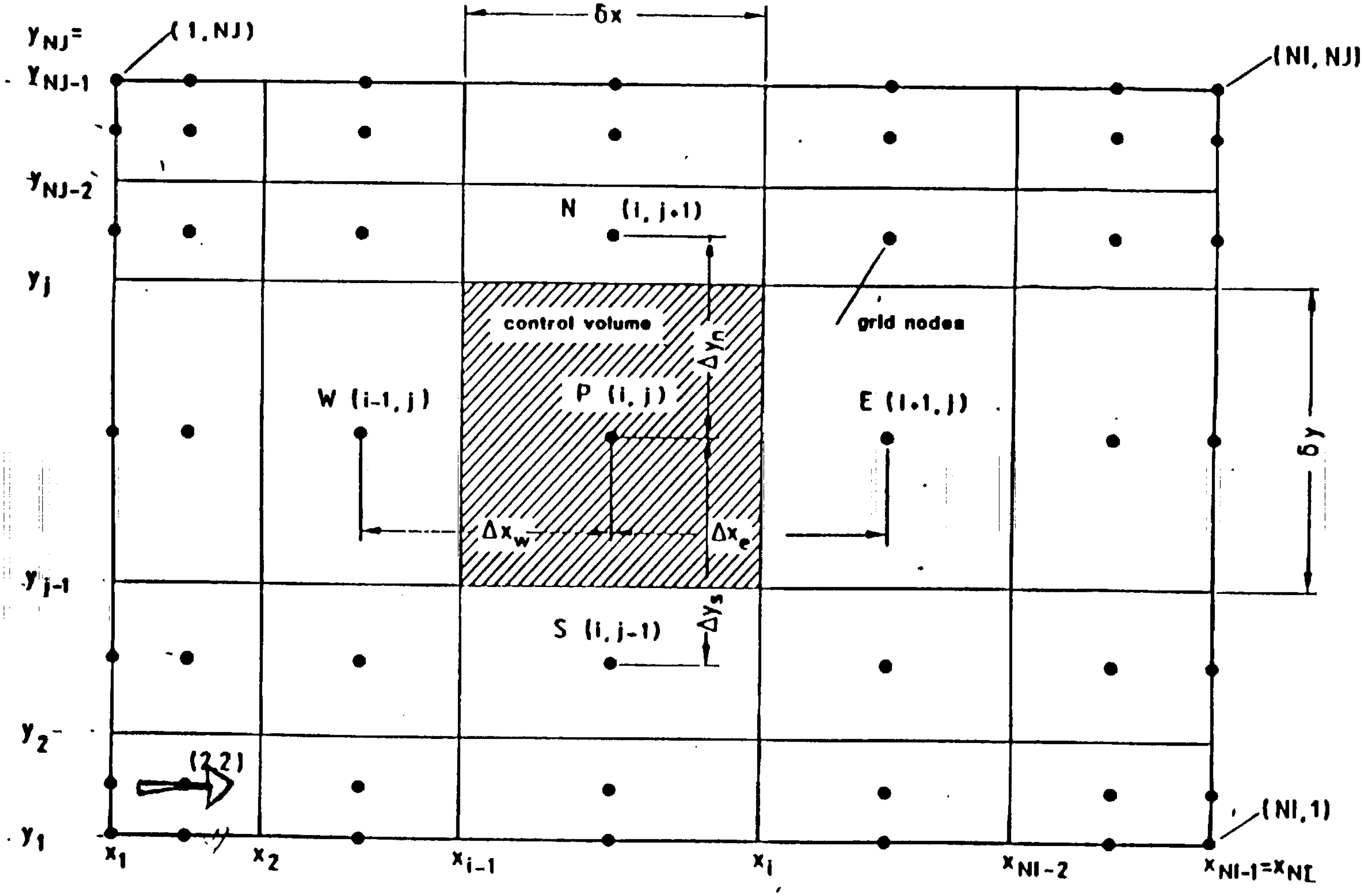

Figure 5.1. Control Volume arrangement and grid numbering.

5.2 Control Volume Variable Storage

Figure 5.1 show a part of the integration domain which is subdivided into small rectangular control volumes by the intersection of x and y lines. The code used in this study uses the so called co-located variable grid arrangement. In the co-located variable arrangement all the dependent variables (U , V ,T,...etc) are stored in the *same* location as shown in figure 5.2. Patankar (1980) had shown how the co-located variable arrangement gives rise to oscillatory (checkerboard) solutions but a special interpolation procedure is used in the present code to determine the cell-face velocities (the main reason for unphysical solutions) to suppress the checkerboard solution. In the discretization scheme to be discussed next, a typical control volume (CV) containing the grid point **P** (see figure 5.2) is integrated. All the surrounding grid points are identified by their sense of direction relative to the grid point **P**, such as the grid point **E** located to the right of point **P**. All the quantities calculated at the CV faces are denoted by lower case subscripts such as "e" for the quantity calculated at the east side cell face. The open arrows denote the mass fluxes at the CV faces in the x and y directions.

5.3 Integro-Differential Equation

The first step in the discretization of the transport equation (eq. 5.1) is to integrate it over a control volume (δv) to yield:

$$\int_{\delta v}\frac{\partial(\rho\phi)}{\partial t}dv+\int_{\delta v}[\frac{\partial}{\partial x}(\rho U\phi-\Gamma_{\phi}\frac{\partial\phi}{\partial x}) + \frac{\partial}{\partial y}(\rho V\phi-\Gamma_{\phi}\frac{\partial\phi}{\partial y})]dv=\int_{\delta v}[S_{\phi}]dv \qquad (5.2)$$

Where

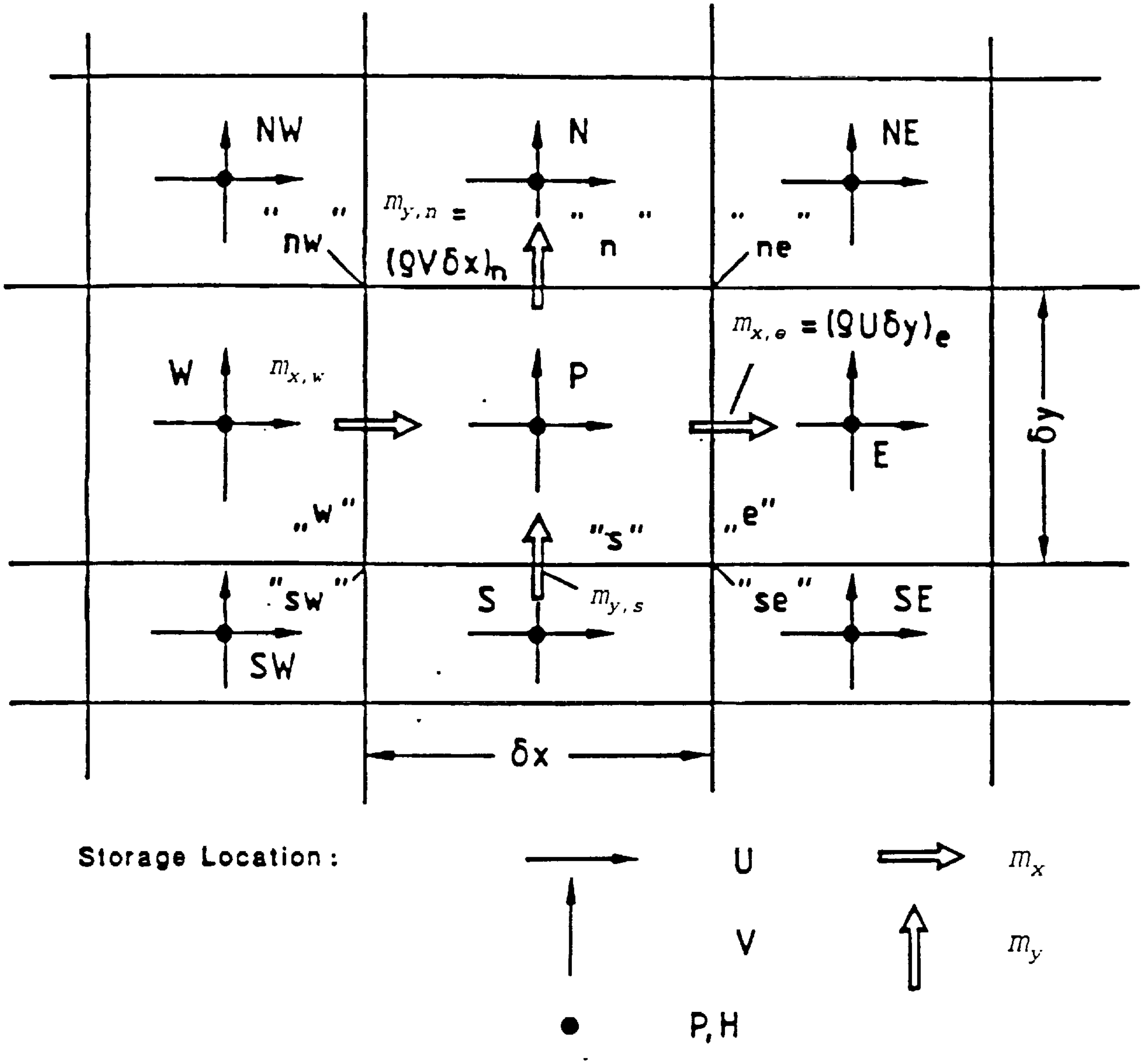

Figure 5.2. Dependent variable control volume storage location for various physical quantities.

$$\delta v = \delta x \delta y \tag{5.3}$$

is the two dimensional "volume" element in the cartesian coordinate system. The second term in eq. (5.2) is the volume integral over the divergence of the convective and diffusive fluxes. Applying Gauss's divergence theorem it is transformed into a surface integral resulting in:

$$\begin{aligned}\int_{\delta v} \frac{\partial(\rho\phi)}{\partial t} dv &+ \int_s^n [(\rho U\phi - \Gamma_\phi \frac{\partial\phi}{\partial x})_e - (\rho U\phi - \Gamma_\phi \frac{\partial\phi}{\partial x})_w] dy \\ &+ \int_w^e [(\rho V\phi - \Gamma_\phi \frac{\partial\phi}{\partial y})_n - (\rho V\phi - \Gamma_\phi \frac{\partial\phi}{\partial y})_s] dx \\ &= \int_{\delta v} [S_\phi] dv\end{aligned} \tag{5.4}$$

A closer look at equation (5.4) reveals that it is nothing but a balance between the rate of accumulation of ϕ within the CV and the net transport of ϕ by convection and diffusion across the CV faces plus the source or sink terms within the CV. Further the eq. (5.4) is still exact in the sense no approximations have yet been introduced. The next step is the discretization of the eq. (5.4) thus introducing the approximations.

5.4 Discretization Scheme

The discretization of eq. (5.4) is done in two steps. In the first step the surface and volume integrals appearing in are approximated by utilizing the mean value theorem. The linearization of the coefficient are also done in this step. In the second step the mean values of various transport quantities arrived at in the first step are discretized and related to the CV grid points.

5.4.1 First Level Approximations

The approximations for the integrals appearing in eq. (5.4) using the mean value theorem involves two crucial assumptions, viz:

- the fluxes through the CV faces are approximated as the product of the mean flux per unit area going through the centre of the particular CV *face* and the CV face area.
- the integrals involving the time derivative and the source terms are approximated as the product of the mean value of the integrand associated with the CV centre and the CV.
- the coefficients are also linearized in this step. All the mass fluxes and the diffusivities are evaluated with values from previous iteration.

Using the above three assumptions eq. (5.4) can be written as:

$$\begin{aligned}\frac{\partial(\rho^{*}\phi)}{\partial t}\delta v &+ [m^{*}_{x,e}\phi_{e} - \Gamma^{*}_{\phi,e}(\frac{\partial\phi}{\partial x})_{e}\delta y] - [m^{*}_{x,w}\phi_{w} - \Gamma^{*}_{\phi,w}(\frac{\partial\phi}{\partial x})_{w}\delta y] \\ &+ [m^{*}_{y,n}\phi_{n} - \Gamma^{*}_{\phi,n}(\frac{\partial\phi}{\partial y})_{n}\delta x] - [m^{*}_{x,s}\phi_{s} - \Gamma^{*}_{\phi,s}(\frac{\partial\phi}{\partial y})_{s}\delta x] \\ &= S_{\phi}\delta v\end{aligned} \tag{5.5}$$

Where

$$m_{x} = \rho U(\delta y) \quad ; \quad m_{y} = \rho V(\delta x) \tag{5.6}$$

are the mass fluxes across the control volume faces in the x and y directions respectively. Also the starred ("*") variables indicate values obtained from previous iteration.

The second step of approximations involves the discretization of the convective fluxes, diffusive fluxes, source terms and time derivative.

5.4.2 Discretization of Convective Fluxes

This step involves the discretization of the convective fluxes or the mass fluxes found in eq. (5.5). Special care has to be taken to find the values of the dependent variables at the CV face (e.g. ϕ_e, etc) with respect to the values at the grid nodes (i.e the centre of the CV). The code used in this study uses a flux-blending approach or a hybrid method to evaluate the variable at CV faces which is linear combination of two methods with different order of accuracy, namely

- the first-order Upwind Differencing Scheme (UDS), and
- the second-order Central Differencing Scheme (CDS).

A pure CDS cannot be used in flow situations where there is a flow reversal and recirculation as it can give rise to unphysical solutions (see Patankar, 1980), whereas UDS albeit lower in accuracy ensures a diagonally dominant, positive definite coefficient matrix. This is achieved in UDS by replacing the cell face value by the grid point or node value closest to the CV face depending on the flow direction, unlike in CDS where the cell face value is evaluated from a linear interpolation of adjacent grid point values. Using the hybrid approach the value of the dependent variable at the east cell face can be written as:

$$\phi_e = \phi_e^{UDS} + \gamma(\phi_e^{CDS} - \phi_e^{UDS})^* \tag{5.7}$$

Here γ weighs the contributions of UDS and CDS and is 0 for a pure UDS and 1 for pure CDS. The "*" implies the values evaluated at a previous iteration level thus making it a "deferred correction" approach. The deferred correction ensures the diagonal dominance required for the solution of the algebraic equations even for a pure CDS. In the present study a pure UDS ($\gamma = 0$) was used for all the cases investigated.

5.4.3 Discretization of the Diffusive fluxes

The diffusive fluxes are the first derivative terms (gradient terms) in eq. (5.5) multiplied by the diffusivity (Γ_ϕ). A second order central difference discretization method is used to evaluate these terms and a typical form of it for the gradient at the "east" cell face would be:

$$\left(\frac{\partial\phi}{\partial x}\right)_e = \frac{\phi_E - \phi_P}{\Delta x_e} \tag{5.8}$$

It is important to note the ϕ are evaluated at the grid node value (upper case). Similar formulations can be derived for the gradients at other cell faces.

5.4.4 Discretization of the Source Terms

The source terms appearing in the right hand side of eq. (5.5) is replaced by the value obtained at the centre of control volume (or grid node **P**, see fig. 5.2), i.e.:

$$S_\phi \delta v \approx S_{\phi,P} \delta v \tag{5.9}$$

In case of non-linear special care has to be taken to linearize the source terms such that only the positive contributions are added to the algebraic equation. For further details regarding this see Perić and Scheuerer(1989).

5.4.5 Discretization of the Time Derivative

Two basic assumptions are utilized to discretize the time derivative term in eq. (5.5). First, CV mean value of ϕ is approximated as the grid node value ϕ_P and secondly, the value of dependent variable is assumed to be varying linearly with time. Utilizing these two assumptions one gets:

$$\frac{\partial(\rho\,\phi)}{\partial t} \approx \frac{\rho\,\phi_P - \rho^0{}_P\phi^0{}_P}{t - t^0} \tag{5.10}$$

The superscripts "*0*" stands for the values obtained from previous time step.

Since all the space derivatives and source terms are evaluated at the new or current time level it makes the whole discretizing scheme fully implicit. In other words there is no restriction on the time-step chosen.

5.4.6 The Final Form of the Discretization Equation

After substituting for the approximations described in Sections 5.4.1-5.4.6 into the eq. (5.5) one gets the final discretization equation for grid node **P** as:

$$a_P\phi_P = a_W\phi_W + a_E a_E + a_S\phi_S + a_N\phi_N + b_P \tag{5.11}$$

A look at eq. (5.11) reveals that the value of the dependent variable at the grid node **P** is dependent on the surrounding grid nodes. The coefficients "a" contain the contributions from the convective and diffusive fluxes and "b_P" contains the source term.

The detailed formulations of the coefficients can be found in Perić and Scheuerer (1989).

5.5 Solution Algorithm

The governing equations presented in Chapter III (eqs. 3.1-3.4) are all coupled together for a general fluid flow problem. For incompressible low speed flows the momentum and continuity equations are strongly coupled together. Hence special algorithms need to be used to solve for the dependent variables, in the numerical code used in the present study the well known and tested SIMPLE algorithm (Semi-Implicit Method for Pressure-Linked Equations) has been implemented. A brief outline of the SIMPLE algorithm will be presented next. For unsteady flows the solution algorithm is applied to each time step.

5.5.1 SIMPLE algorithm

The SIMPLE algorithm is sequential step by step solution procedure where each of the governing equations (e.g. continuity,x-momentum, etc.) are solved one after another and then coupled together by physically derived algebraic relations. The algorithm consists of the following steps:

0) First step consists of initialization of all the dependent variables such that the finite volume coefficients (the fluxes) and the pressure difference (source term) in the momentum equations can be evaluated. Any sensible initial guess value can be used, for unsteady flows such as the present problem values from previous time step can be used as a good initial estimate.

1) Next the finite volume coefficients of the x-momentum equations are assembled. Then the resulting set of linear algebraic equations are solved to yield the axial

velocity U^*. Since the resulting new velocity is only approximate (based on initial guessed pressure), the algebraic equations have been solved by an iterative solution algorithm instead of direct matrix inversion algorithm. These iterations are called "inner" iterations and the number of these "inner" iterations can be user controlled.

2) The same procedure (Step 1) is used to obtain the normal velocity V^* from the y-momentum equation.

3) Since the initial pressure is guessed, the velocities U^* and V^* will not satisfy the continuity equation even though they will satisfy the momentum equations. In this step a pressure correction equation is derived (see Appendix B) to estimate the pressure and its associated velocity and mass fluxes from the continuity and momentum equations. These corrected velocities will then satisfy the continuity equation but will throw the momentum equations out of balance in the process.

4) Once the velocities satisfying the continuity equations are found all the scalar transport equations are solved in the present case the energy equation. The energy equation is solved in the same process as described in Step 1. As the energy equation is decoupled only one "inner" iteration is performed, although i could have been solved after the true velocities have been found.

5) The residual norms are computed for all the conservation equations which in an ideal case of correct solution should go to zero. These residual norms are

normalized by appropriate reference quantities. If any of the normalized residual norms is greater than the user specified convergence criterion the algorithm returns to Step 1 and uses the current values to evaluate the new finite volume coefficients.

6) If all the normalized residuals norms are smaller than the specified convergence criterion than convergence is declared. For unsteady problems, the time counter is incremented by the time step size (δt) and the algorithm return to Step 0 with the initial guesses for the dependent variables taken from the previous time step.

In the present study the convergence criterion was choosen to be 0.1% of the reference residual norms. Further, special care has to be taken for oscillatory flows when evaluating the reference mass flux for the residual normalization(Step 6). Since at the instant of flow reversal the mean flow velocity is zero. In these situations the code has been modified to use the reference mass flux based on the maximum inlet velocity (U_{max}).

5.6 Code Modifications For Oscillating Flows

The computer code CAST has been modified to account for the cyclical nature of the oscillatory flows and the switch in the boundary conditions. Although care has been taken to retain the structure of the code and utilize the Vectorizing capabilities of the Cray YMP supercomputer. Briefly, few of the major changes include:

▸ At flow reversal (0°,180°,360°) the inlet and exit boundary *planes* are switched to account for the zero mean flow situation.

▸ A new energy equation (assembly & evaluation of the FV coefficients) routine has been written along with the proper boundary condition to solve for the heat transfer problem.

- The code has also been modified to solve the conjugate heat transfer. The change has been made such that the numerical code is transparent to the presence of solid and fluid region (i.e. the energy equations is solved together for the solid and fluid regions. This has been achieved through modifications of the diffusive coefficients and source terms details of which can be found in the book by Patankar (1980).

In addition to these, minor modifications have been done to accelerate the convergence of the equations.

CHAPTER VI

OPERATING CONDITIONS AND GEOMETRIC MODELING

This chapter concerns itself with the nondimensional parameters conditions under which the Stirling engine heat exchangers operates. This chapter also addresses the way the heat exchangers are modelled numerically such that the geometry closely approximates to the one found in the engine. The operating parameters are given specifically for the NASA SPRE (Space Power Research Engine), the object of present study. Figure 1.2 showed how the heat exchangers in the SPRE are located, the cooler starts from the compression space and opens into the regenerator which in turn is connected to the heater and which opens into the expansion space.

6.1 Operating conditions

The parameters under which the SPRE operates were taken from the one dimensional code GLIMPS, which simulates a Stirling cycle engine and has been used extensively by researchers at NASA. The numerical simulation of the heat exchangers used in the present study were based on GLIMPS and these are listed below in columar format for the Regenerator, Cooler and Heater respectively.

Regenerator

PARAMETER	GLIMPS CODE	PRESENT STUDY	
Hyd. Diameter D_h, (m)	0.133 3×10^{-2}	0.10	?
Wire Diameter D_w, (m)	2.54×10^{-5}	5.0×10^{-3}	
Matrix Length L, (m)	24.63×10^{-3}	12.00	
Mean Pressure (MPa)	15	n/a	
Gas Temp. (Hot side) (~~°~~K)	$617.2+(12.6)\,Sin(\omega t+2.07)$	274	
Gas Temp. (Cold side) (~~°~~K)	$345.1+(2.10)\,Sin(\omega t+2.31)$	273	
Valensi Number (Va)	1.5	2.5,400	
Re_{max}	265	75,12000	
A_r	0.478	0.25	

Cooler

PARAMETER	GLIMPS CODE	PRESENT STUDY	
Hyd. Diameter D_h, (m)	1.524×10^{-3}	5.0×10^{-2}	?
Tube Length L, (m)	95.25×10^{-3}	6.0	
Number of Tubes	1584	1	
Mean Pressure (MPa)	15	n/a	

Gas Temp. (Hot side) (°K)	345.1+(2.1) $Sin(\omega t-2.31)$	340,350
Gas Temp. (Cold side) (°K)	332.7+(12.9) $Sin(\omega t+0.13)$	330,340 &
Wall Temp. (°K)	324.3+7.5x10^{-5} $Sin(\omega t+0.77)$	330,340
Valensi Number (Va)	350	175,350,700
Re_{max}	300000	15000,30000 & 60000
A_r	0.686	0.714

Heater

PARAMETER	GLIMPS CODE	PRESENT STUDY
Hyd. Diameter D_h, (m)	1.27x10^{-3}	5.0x10^{-2}
Tube Length L, (m)	90.17x10^{-3}	7.0
Number of Tubes	1632	1
Mean Pressure (MPa)	15	n/a
Gas Temp. (Hot side) (°K)	625.8+(29.1) $Sin(\omega t+0.33)$	630,620
Gas Temp. (Cold side) (°K)	617.2+(12.6) $Sin(\omega t+2.07)$	610,620
Wall Temp. (°K)	324.3+1.4x10^{-4} $Sin(\omega t+0.76)$	650
Valensi Number (Va)	88	44,88 & 176
Re_{max}	16500	8250, 16500 & 33000
A_r	0.686	0.714

The regenerator parameters used in this study are diffrent from that predicted by the GLIMPS code since the regenrator was modelled as a seperate entity. Whereas the operating conditions for the regenerator got from GLIMPS is based on a complete simulation of the Stirling engine i.e. including the cooler and heater. Also the wall temperature fluctuations were assumed to be zero in the present study as they are small.

Working Fluid

The working fluid used in the numerical simulations was helium which is the same as used in the SPRE. The following properties of helium at standar atmospheric pressure were used for all the numerical simulations conducted in this study:

Density (kg/m^3)	0.200
Dynamic Viscosity (N.s/m^2)	2.83x10^{-5}
Specific Heat, c_p (J.kg^{-1}/K^{-1})	5200.00
Thermal Conductivity, k,(W.m^{-1}.°K)	0.20439
Prandtl Number (Pr)	0.72

Regenerator Metal

The regenerator metal used in the conjugate heat transfer problem was chosen to be aluminum and the following properties at 20°C were used in this study:

Density (kg/m^3)	2707.0
Specific Heat, c_p (J.kg^{-1}/K^{-1})	896.00
Thermal Conductivity, k,(W.m^{-1}/K)	20.4

Table 6.1: Test cases investigated in the present study for fluid flow analysis.

TEST CASES	$Re_{\max}$	Va	L/D_h	A_r
R_1	75	2.5	60	0.250
R_2	12000	400	60	0.25
C_1	15000	175	60	0.714
C_2	30000	350	60	0.714
C_3	60000	700	60	0.714
C_4	10000	200	70	0.357
C_5	20000	400	70	0.357
C_6	40000	800	70	0.357
H_1	8250	44	70	1.340
H_2	16500	88	70	1.340
H_3	33500	176	70	1.340

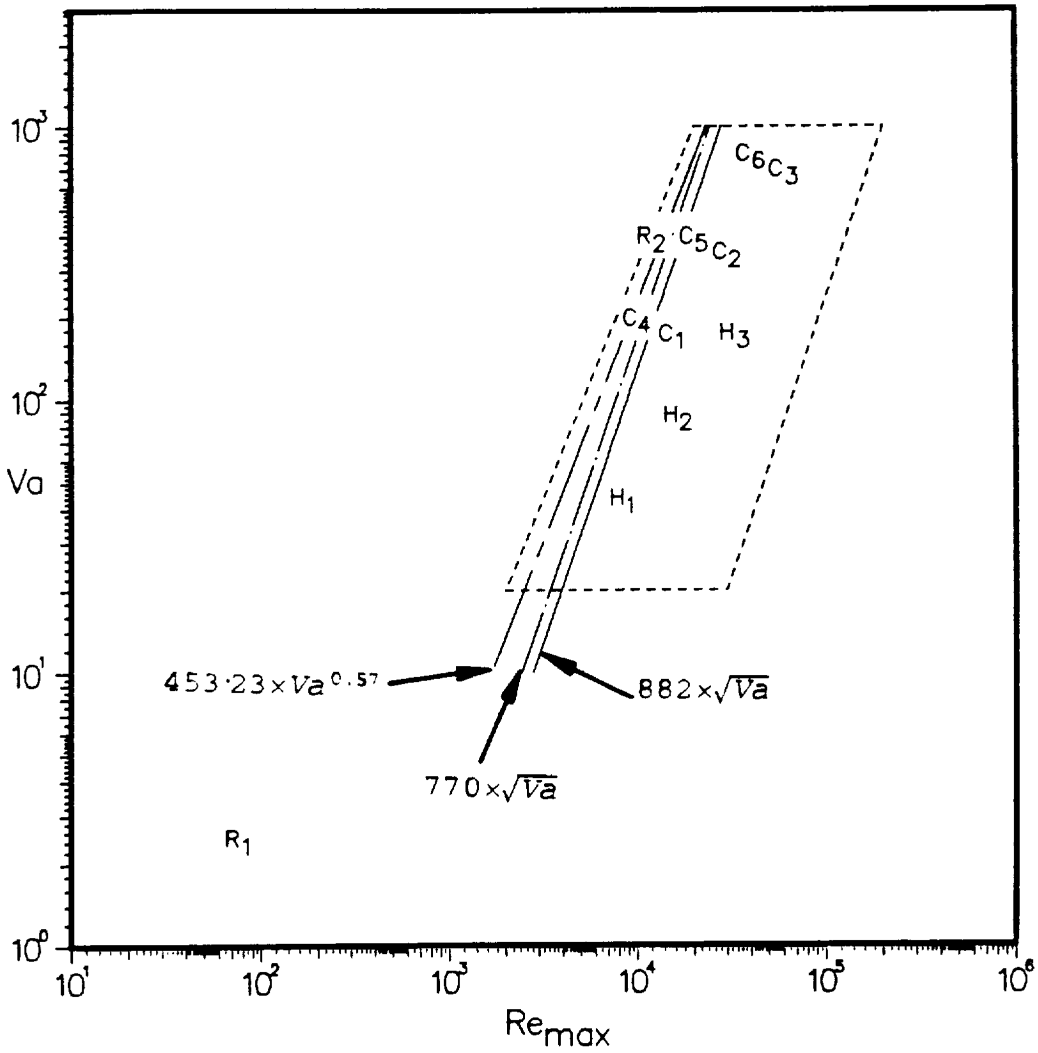

Figure 6.1. Envelope in which different Stirling Engines operate, together with: i) Criterion for transition from laminar to turbulent flow, ii) Different test cases studied in the present work.

Table 6.1 lists all the cases studied in the present work. All the cooler cases begin with the letter "C", the heater with "H" and the regenerator with "R" respectively. Figure 6.2 shows these cases on a Re_{max} and Va plot with various transition criterion found in the literature for laminar to turbulent transition. As it can be seen the SPRE heater and cooler heat exchangers operate on the transition regime. But a laminar analyis is still pertinent since the flow inside the heat exchangers is part laminar and part turbulent within an oscillation cycle.

6.2 Geometric Modeling

Figure 1.2 showed an conceptual geometry of the SPRE, the heater and cooler components consists of bundles of tubes and the regenerator is a foil type matrix. The heater and cooler are modeled as circular tube with a finite length. Only one tube for each component was considered since a through analysis involving all the tubes is beyond the scope of the present study. The regenerator is one of the most important in the Stirling engine and is also one of the most difficult to model since it is a matrix. In the present study this is resolved by modeling it as a parallel-plates channel with geometric similarity i.e. the matrix is replaced by a solid plates of finite thickness with the same hydraulic diameter. In summary :

Heat Exchanger	**Geometry Modelled**
Regenerator	Parallel-Plates Channel
Heater	Circuler Tube
Cooler	Circular Tube

CHAPTER VII

OSCILLATING FLUID FLOW ANALYSIS

In this chapter results for the effect of flow oscillations on the velocity field and associated friction losses are presented and discussed. The investigation has been carried out for a wide range of nondimensional parameters with an eye on the Stirling engine heat exchangers operating conditions. The cases investigated and their operating parameters are given in Table 6.1 (Chapter VI).

Any numerical discretization method gives rise to so called truncation and discretization errors. Hence, code validation is an important element in any numerical simulation, in the present study the results of the numerical simulations have been compared with existing analytical and experimental efforts. The first two sections (7.1,7.2) deal with this aspect concurrently with the fluid flow analysis.

7.1 Fluid Flow in Parallel-Plates Channel and Code Validation

Since the regenerator is modelled as a parallel-plates channel, the fluid flow results for this component are presented next.

7.1.1 Analytical Solution For The Velocity

Kurzweg (1985a) analytically solved the N-S equations governing the oscillatory for flow between two-parallel-plates channel. The geometry investigated is shown in Figure 7.1, where an array of parallel-plates channel are connected at ends, to reservoirs maintained at different temperatures (only part of the geometry as simulated numerically is shown). The flow is set to motion inside the channel by a sinusoidally varying pressure gradient and a temperature difference between the end reservoirs ensures that a constant axial linear temperature gradient is maintained along the channel throughout the cycle. Also, he assumed the walls of the channel to be thick thus signifying a conjugate heat transfer problem or a special case of the generalized constant heat flux thin wall problem.

The channels were assumed to be long such that the fluid flow is "fully developed" or to be more precise, the axial velocity profile is constant along the channel. Under this assumption the momentum equations simplify considerably — in fact, only the axial momentum remains — and are tractable to analytical solution techniques. By neglecting the initial conditions he solved for the quasi-steady axial velocity distributions, i.e, the velocity distributions does not change from one cycle to another cycle at any instant in the cycle and is given by:

Where $i = \sqrt{-1}$ is the imaginary unit, $\Re$ denotes the real part of a complex

$$U(\eta, t) = U_0 \, f(\eta) \, e^{i\omega t} = U_0 \, \Re \left\{ \frac{i\lambda}{\alpha^2} \left[1 - \frac{\cosh(\sqrt{i}\alpha\eta)}{\cosh(\sqrt{i}\alpha)} \right] e^{i\omega t} \right\} \qquad (7.1)$$

quantity, U_0 is an arbitrary velocity scale, $\eta = y / a$ the normalized coordinate distance [y] normal to the flow direction, t the time, $\alpha = a\sqrt{\omega / \nu}$ the Womersley number or the nondimensional frequency (note $Va = 4\,\alpha^2$), and $\lambda = |\partial p / \partial x|_{\max}\, \alpha^2 / \rho U_0 \nu$ the nondimensional amplitude of the imposed sinusoidal pressure gradient. Once the velocity distribution is established practically useful quantities such as the wall shear stress can now be established. The temperature profile is discussed in the heat transfer section to be presented later in this report.

7.1.2 Reformulation of The Analytical Solution

In order to compare the velocity profiles by the numerical solutions with the analytical solution presented above special attention has to be given to carefully match the boundary conditions. A direct comparison with the above solution could not be made because of the different boundary conditions and the two-dimensionality of the numerical simulations. In the derivation of the analytical solution the parallel-plates channel was assumed to be infinetly long (thus rendering it a one dimensional) and more importantly the flow was established by applying a sinusoidally varying pressure gradient [$\partial p / \partial x = |\partial p / \partial x|_{\max} \cos(\omega t)$]. But in the numerical solution the domain is two dimensional and finite in length with the flow being established by a sinusoidally varying velocity [$U_{in} = U_{\max} Sin(\omega t)$] at the inlet, the reason for choosing a velocity boundary condition instead of a sinusoidally varying pressure boundary condition was the ease of implementation numerically. Hence the analytical solution for a periodic velocity

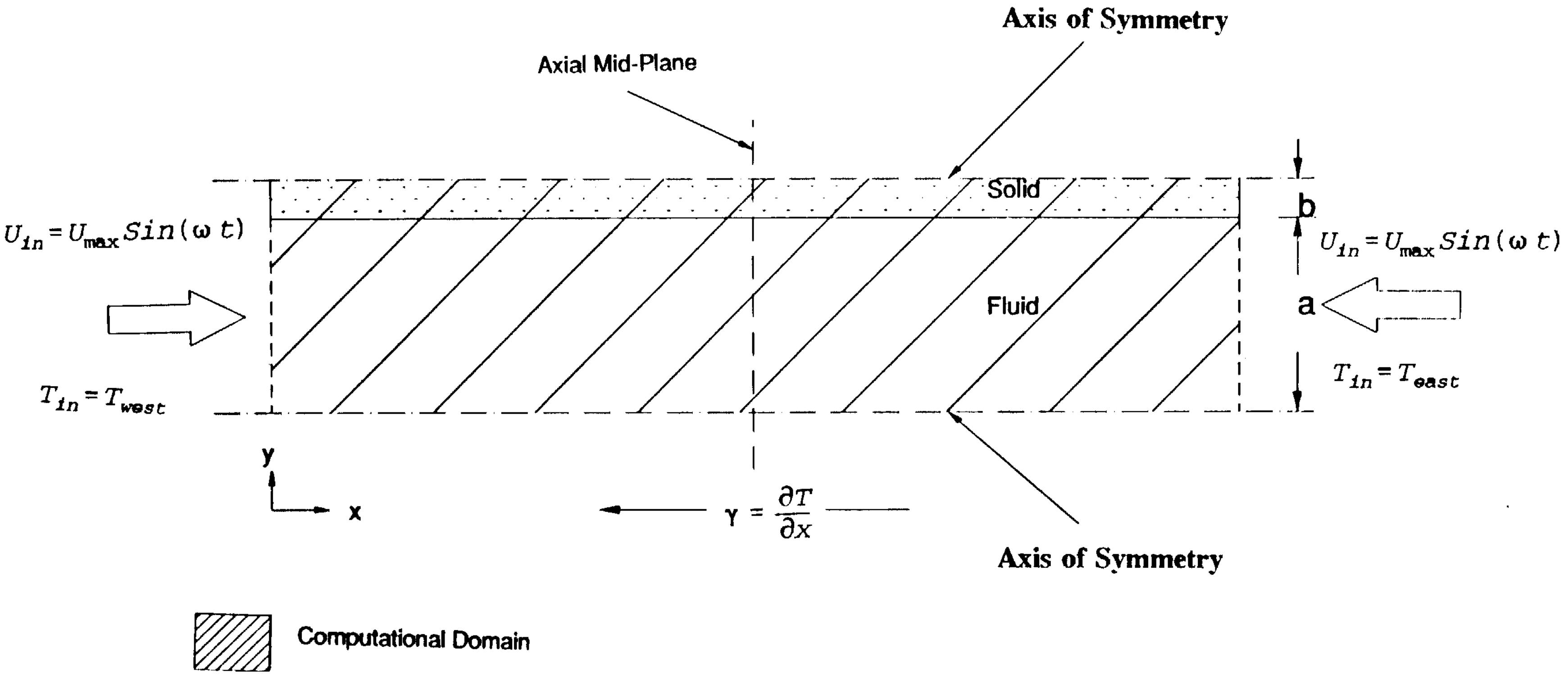

Figure 7.1. The geometry for parallel-plates problem (conjugate heat transfer) with the inlet and outlet boundary conditions.

boundary condition has to be derived first and the proper axial location chosen. The axial center of the channel was chosen for comparing with the theory since it is far away from both the ends the effects of finite channel length can be assumed to be negligible at this location. The solution for the velocity profile [Eq. (7.1)], essentially, stays the same but a phase difference has to be added to account for the velocity bounadary condition. The following equations outline the procedure to derive the phase difference ϕ_u to be added in order to correspond to the numerical simulations:

Given,

$$U_{in} = U_{\max} Sin(\omega t) \tag{7.2}$$

Now defining the U_0 given in Eq. (7.1) to be the same as $U_{\max}$ (maximum inlet velocity), the reference parameter used in numerical solution, or:

$$U_0 \equiv U_{\max} \tag{7.3}$$

and with little algebraic manipulations the nondimensional pressure gradient λ in Eq. (7.1) can now be related to the known numerical parameter α (or Va) by the expression:

$$\lambda = \frac{\alpha^2}{\|\delta_u\|} \tag{7.4}$$

Here δ_u is a *complex quantity* and the double vertical lines ($\|\ \|$) stands for the absolute value or modulus of the complex quantity. Its given by the expression,

$$\delta_u = 1 - \frac{tanh(\sqrt{i\alpha})}{\sqrt{i\alpha}} \tag{7.5}$$

Also the phase difference ϕ_u to be added to the analytical solution for a sinusoidally varying velocity input is given by:

$$\phi_u = 90 + \tan^{-1}\left[\frac{\Im(\delta_u)}{\Re(\delta_u)}\right] \tag{7.6}$$

Where symbols $\Re$ and $\Im$ denote the real and imaginary parts of a complex number. Finally, the velocity distribution corresponding the boundary condition given by Eq. (7.2) is given by:

$$U(\eta, t) = U_{\max} f_n(\eta)\, e^{(\omega t + \phi_u)} = U_{\max} \Re\left\{\frac{i}{\|\delta_u\|}\left[1 - \frac{\cosh(\sqrt{i\alpha\eta})}{\cosh(\sqrt{i\alpha})}\right] e^{i(\omega t + \phi_u)}\right\} \tag{7.7}$$

Where $f_n(\eta)$ is a complex function varying with the normal distance (y) and given as:

$$f_n(\eta) = \frac{i}{\|\delta_u\|}\left[1 - \frac{\cosh(\sqrt{i\alpha\eta})}{\cosh(\sqrt{i\alpha})}\right] \tag{7.8}$$

Equation (7.7) was used to compare with the numerical velocity predictions at the mid-plane of the channel as the entrance effects due to the finiteness of the computational domain can be assumed to be negligible at this axial location. The practically useful quatities such as the wall shear stress (τ_w) (directly related to the friction factor) and the pressure drop across the channel were also compared with the numerical predictions. The corresponding equations for these two quantities can be easily derived from their definitions and for a sinusoidal velocity input are given by:

$$\tau_w = 12\left(\frac{\mu}{D_h}\right)\sigma_\tau\, U_{\max} \sin(\omega t + \phi_\tau) \tag{7.9}$$

Here σ_τ is called as the wall shear stress augmentation factor which can be shown to be:

and ϕ_τ the lead phase angle to be added to the wall shear stress can be expressed as :

$$\sigma_\tau = \left\| \frac{z_\tau}{\delta_u} \right\| \quad ; \quad z_\tau = \frac{1}{3}\left[i\sqrt{i\,\alpha} - \tanh\left(\sqrt{i\,\alpha}\right) \right] \tag{7.10a,7.10b}$$

$$\phi_\tau = \phi_u - \tan^{-1}\left[\frac{\Im\,(Z_\tau)}{\Re\,(Z_\tau)}\right] \tag{7.11}$$

The instantaneous pressure gradient across the channel can be obtained by integrating the axial momentum equation across the channel and with little algebraic manipulations one obtains:

$$-\frac{dP}{dx} = 48\left(\frac{\mu}{D_h^2}\right)\sigma_P\, U_{\max}\, \sin\left(\omega t + \phi_P\right) \tag{7.12}$$

Here σ_P and ϕ_P are the pressure gradient augmentation factor and lead phase angle respectively, and are given as:

$$\sigma_P = \sqrt{\left[\sigma_\tau \cos\phi_\tau\right]^2 + \left[\frac{Va}{12} + \sigma_\tau \sin\phi_\tau\right]^2} \tag{7.13}$$

$$\phi_P = \tan^{-1}\left[\frac{\frac{Va}{12} + \sigma_\tau \sin\phi_\tau}{\sigma_\tau \cos\phi_\tau}\right] \tag{7.14}$$

Few interesting points need to be mentioned about the effects of Valensi number on the augementation factors and phase angles for the wall shear stress and pressure drop. When the Valensi number (Va) is low the augentation factors (σ_τ and σ_P) approaches unity and reduce to the familiar steady state formulations. For high Va the phase angles ϕ_τ and ϕ_P asymptotically reach 45° and 90° respectively or the wall shear stress and pressure drop are out of phase with the inlet velocity by these angles. In addition for high Va the augmentaion factors σ_τ and σ_p reach as high as 8 and 120 times the steady state value. Figures (7.2) and (7.3) graphically demonstrates these effects, the augmentation factors are show in Fig. 7.2 and the phase angles in Fig. 7.3 both of them plotted versus the Valensi number (Va).

Equations (7.7),(7.10) and (7.11) were used to compare the axial velocity profile, wall shear stress at the axial mid-plane and the instantaneous pressure drop across the channel for the cases R_1 and R_2. The results of these comparisons are discussed next.

7.1.3 Comparison with Numerical Simulation

Axial Velocity

The regenerator cases (R_1 and R_2) were chosen to validate the code against the analytical solution. Fig. (7.4) shows a plot of the normalized axial velocity (U/U_{max}) vs. the nondimensional transverse distance (y/a) for the case R_1 Re_{max}= 75 and Va =2.5 at different velocity phase angles (from 30° to 360° with 30° increment). The symbols are used for the analytical solution (Eq. 7.7) and the dotted lines are used for the numerical predictions. It should be appropriate to mention that the comparison was made at the axial mid plane ($x = L/2$) as shown in Fig. 7.1. The velocity profile exhibits the familiar parabolic profile due to the low frequecy (Valensi number) and is completly in phase with the input velocity. The agreement between the analytical solution and the numerical prediction is excellent. Fig. 7.5 shows a similar plot for the case R_2,Re_{max}= 12000 and Va= 400. Here one can observe the effect of the high Va on the velocity profile, by the presence of a small Stoke's layer near the wall and with the flow field

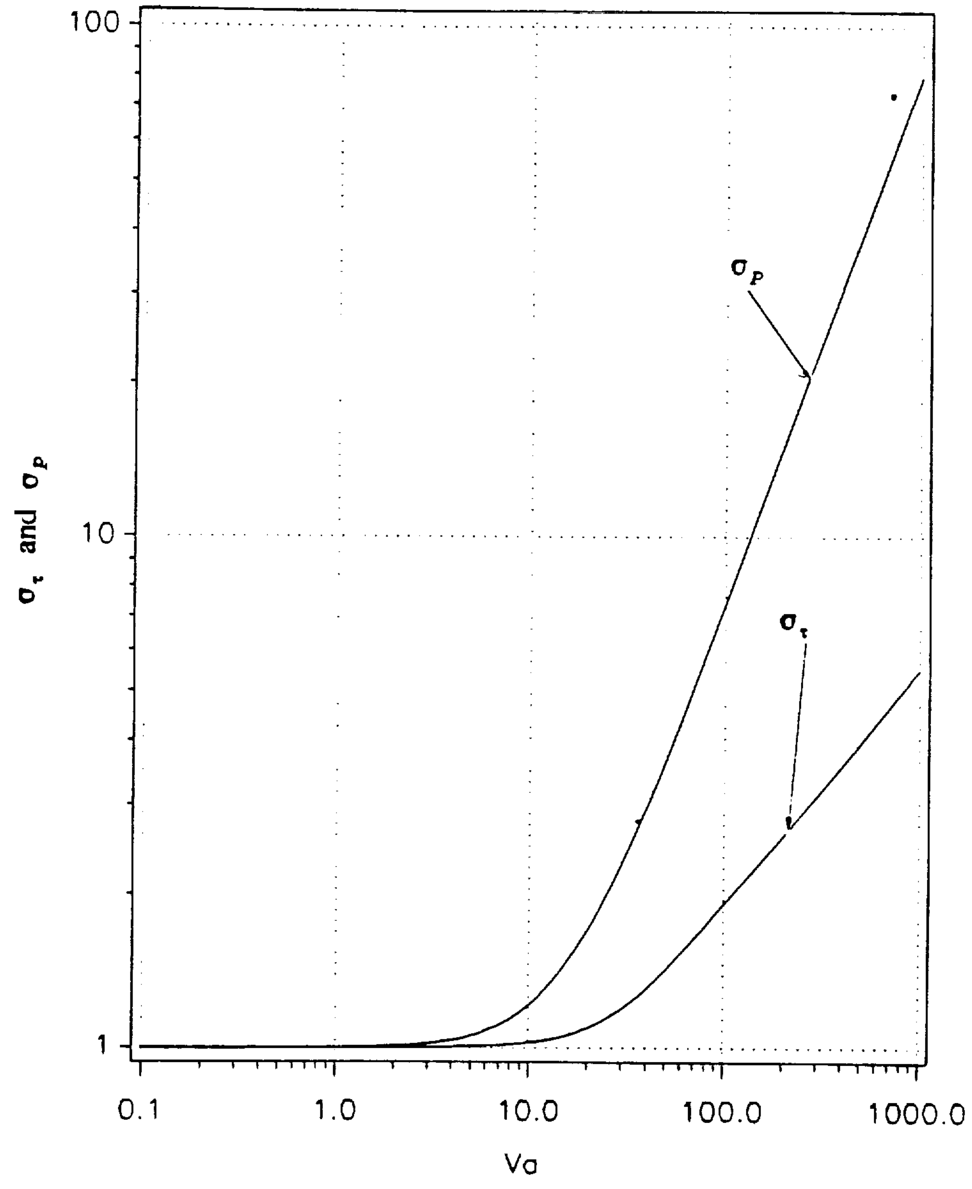

Figure 7.2. Shear stress and Pressure drop augmentation factors, σ_τ and σ_P respectively for oscillating flow between parallel-plates channel.

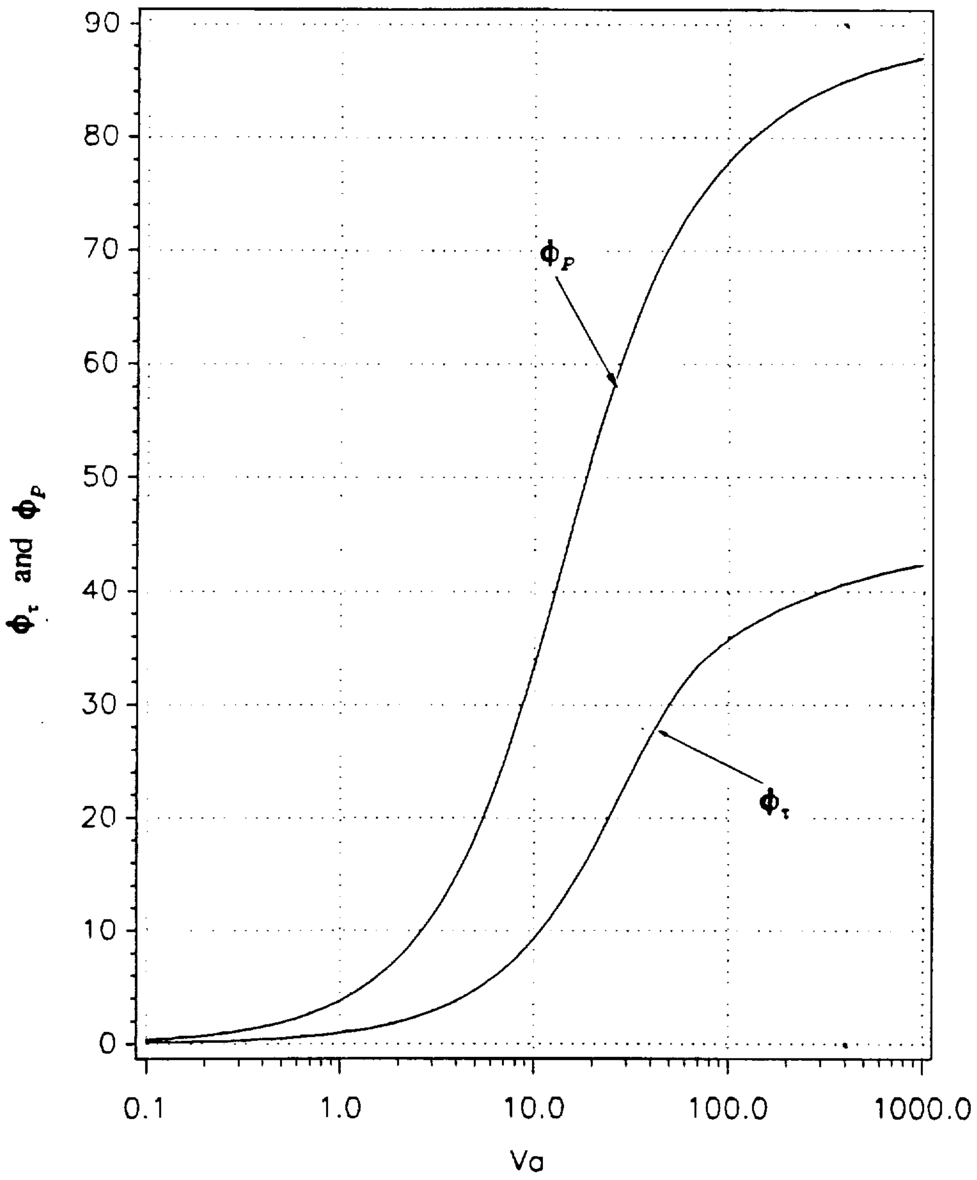

Figure 7.3. Shear stress and Pressure drop lead phase angles, ϕ_τ and ϕ_P respectively for oscillating flow between parallel-plates channel.

almost uniform in the channel core. The rationale behind this phenomena being that the flow reversal (switch in the flow direction) takes place before the viscous effects have time to diffuse down along the radius. Also it can be observed from the Figure (7.5) the flow reversal is also captured very accurately by the numerical code even for high Va. Again it can be seen that the agreement with the analytical solution is excellent.

Wall shear stress and Pressure Drop

Figures (7.6) and (7.7) shows the normalized wall shear stress versus the velocity phase angle at the axial mid plane for the cases R_1 and R_2 respectively. The normalization factor chosen was the coefficient of the sine function in Eq. (7.9). The symbols denote the analytical result (Eq. 7.9) the solid line represents the numerical predictions. When the Valensi number is low, the τ_w (wall shear stress) is in phase with the inlet velocity phase angle and its magnitude is exactly equal to the steady state value. But for high Va (case R_2, Fig. 7.7) the τ_w is not only 45° out of phase with the inlet velocity but also its magnitude is augmented four times the steady state value.

Figures 7.8 and 7.9 show similar figures for the normalized pressure drop along the channel plotted versus the velocity phase angle , again the symbols are for the analytical solution (Eq. 7.12) and the solid line for the numerical prediction. Fig. 7.8 is for the low valensi number case (R_1) and Fig. 7.9 for the high Va case (R_2). But unlike the wall shear stress the pressure drop for high Va is 90° out of phase with the inlet velocity and its magnitude is 40 times the steady state value.

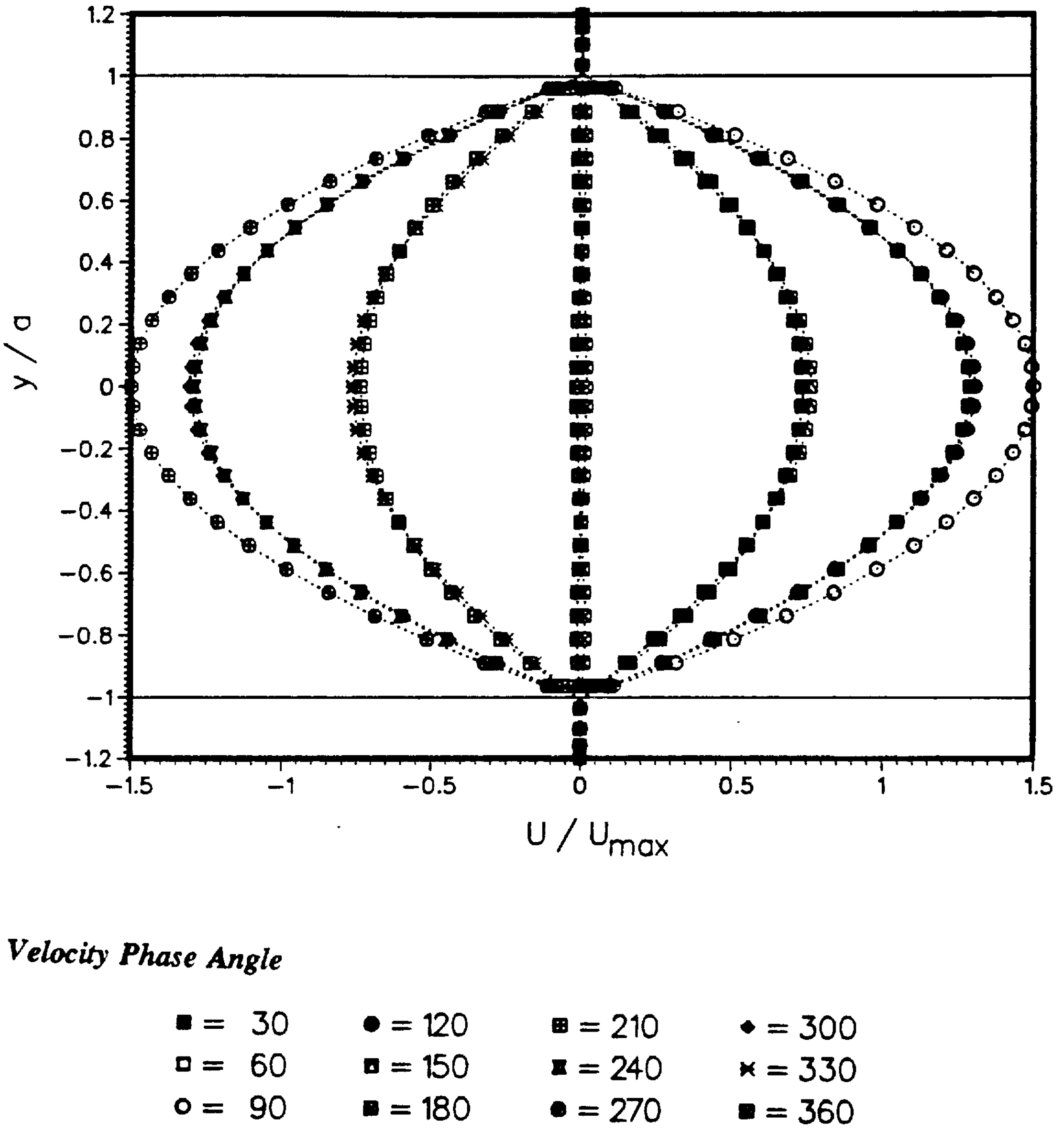

Figure 7.4. Comparison between analytical and numerical velocity profiles at different velocity phase angles for the conjugate heat transfer problem, Case R_1 : Re_{max}=75 and Va=2.5.
[Symbols : Analytical-Kurzweg ;; Dotted Lines : Numerical]

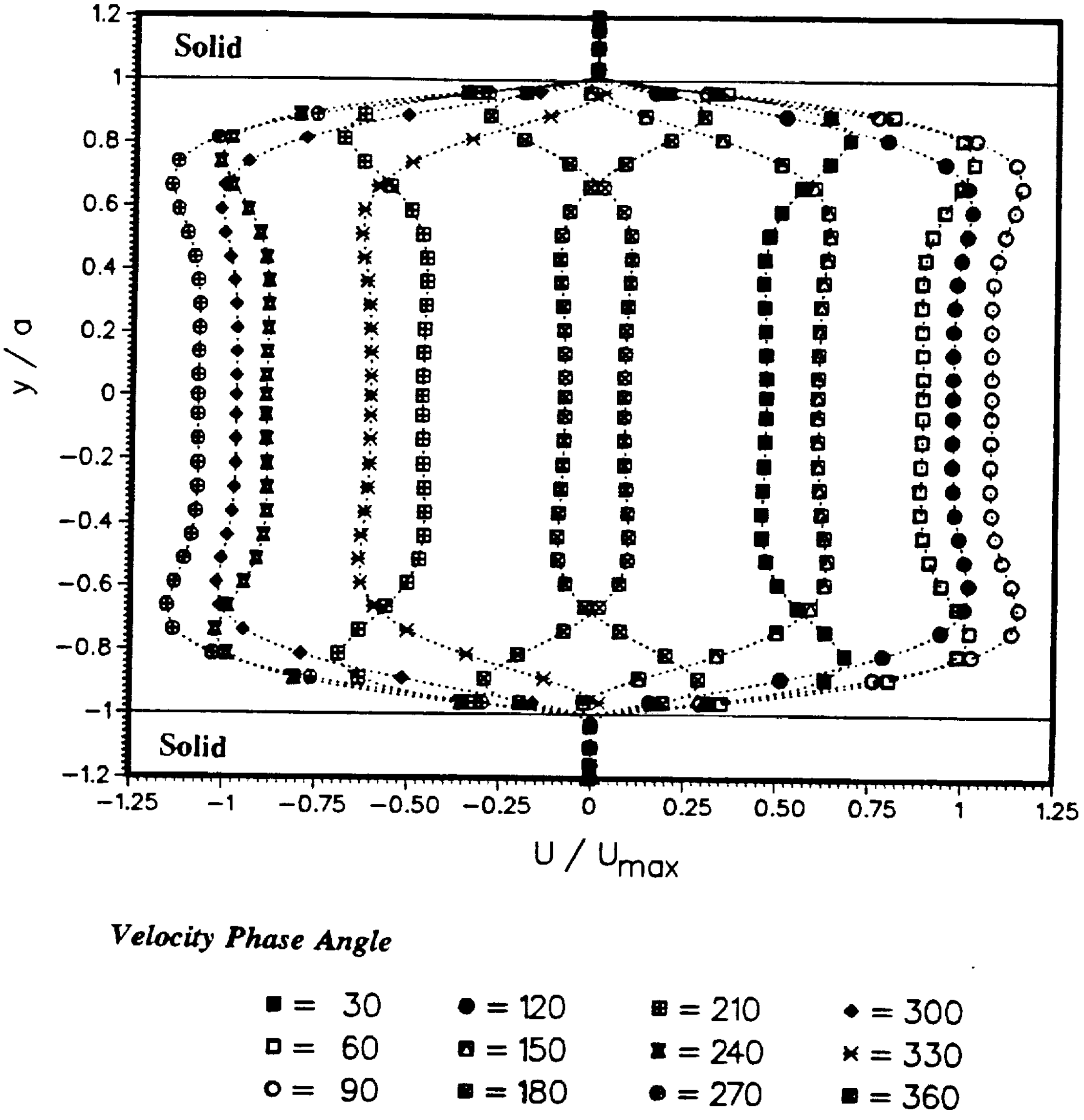

Figure 7.5. Comparison between analytical and numerical velocity profiles at different velocity phase angles for the conjugate heat transfer problem, Case R_2 :Re_{max}=12000 and Va=400.
[Symbols : Analytical-Kurzweg ;; Dotted Lines : Numerical]

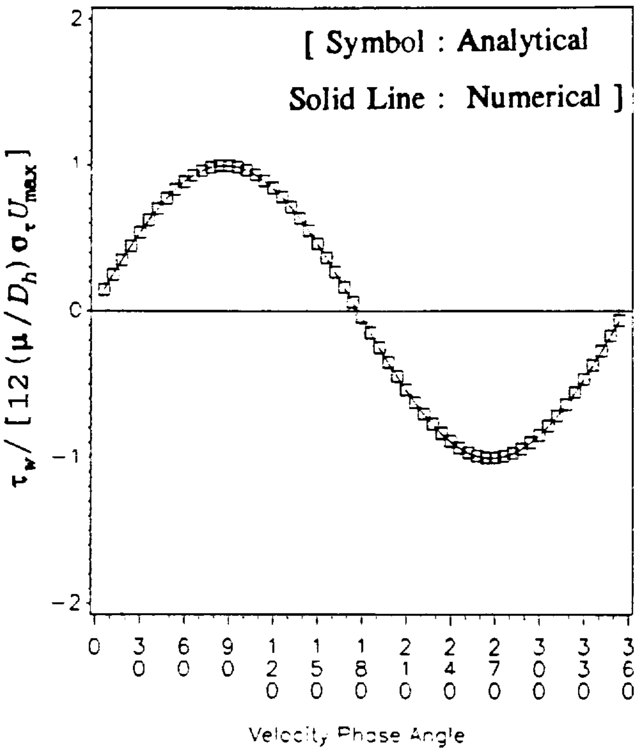

Figure 7.6. Comparison between Analytical and Numerical normalized Wall shear stress (τ_w) versus the velocity phase angle for Case R_1 : Re_{max} = 75 and Va = 2.5.

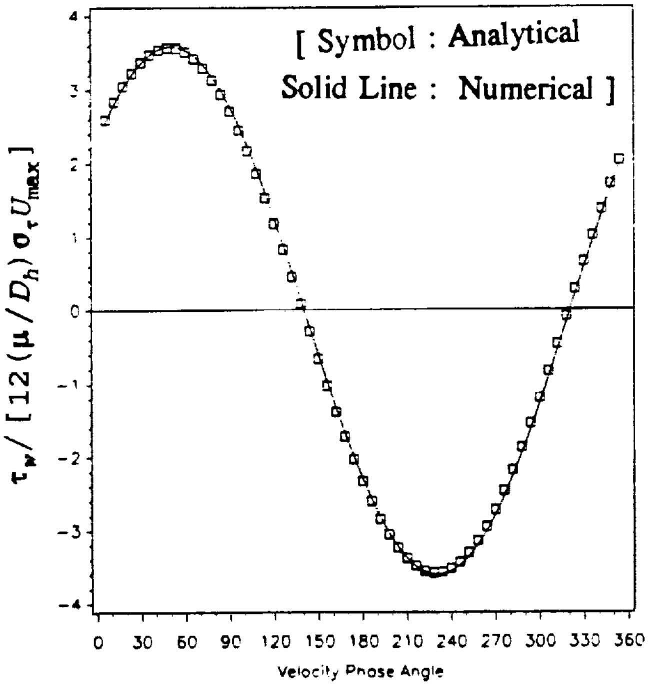

Figure 7.7. Comparison between Analytical and Numerical normalized Wall shear stress (τ_w) versus the velocity phase angle for Case R_2 : Re_{max} = 12000 and Va = 400.

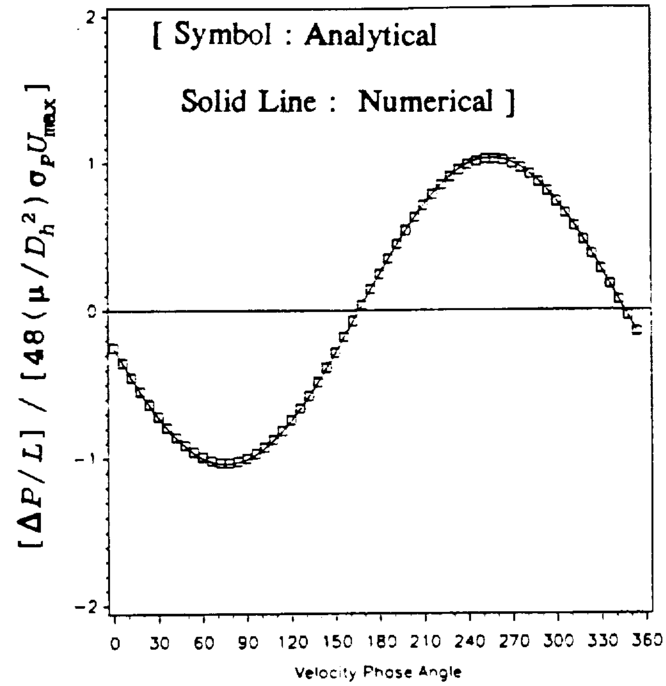

Figure 7.8. Comparison between Analytical and Numerical normalized Pressure Drop ($\Delta P/L$) versus the velocity phase angle for Case R_1 : Re_{max} = 75 and Va = 2.5.

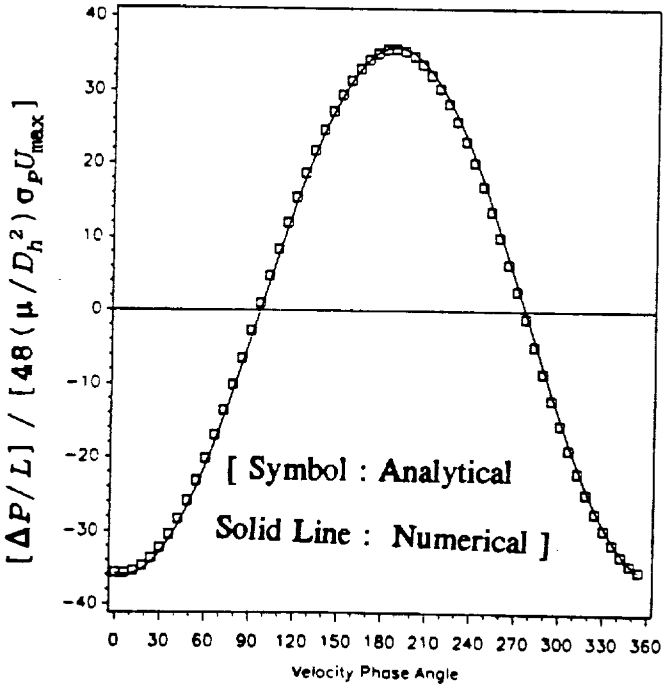

Figure 7.9. Comparison between Analytical and Numerical normalized Pressure Drop ($\Delta P/L$) versus the velocity phase angle for Case R_2 : Re_{max} = 12000 and Va = 400.

7.2 Comparison with Experimental Data

This section is concerned with the comparison of the numerically predicted solutions with the experimental work carried out at the University of Minnesota. For the sake of clarity a brief description of the oscillatory flow rig at the University of Minnesota is also included.

7.2.1 Description Of the Experimental Setup

The experimental study by the researchers at University of Minnesota was initiated to help understand the thermo-mechanical energy losses in the free piston Stirling engines in order to come out with better designs. Their preliminary survey suggested, a better understanding and characterization of the laminar to turbulent flow transition in oscillatory flows (see Sueme and Simon,1988). The initial efforts were concerned with understanding the mechanisms by which transition takes place and generally characterizing the fluid mechanics of oscillatory flows. Recently (see Seume et al.,1992), detailed measurements were carried out at a particular operating point,namely that of the heater tubes of NASA's Space Power Research Engine(SPRE). The velocity measurements were taken at four axial stations located along the test section as shown in Fig. (7.10). Figure (7.10) also demonstrates the flow oscillation in the test section 9or tube) being affected by the piston-rod assembly. The test section is a circular pipe connected by smooth nozzles at both ends; the smooth contour of the nozzles ensures no flow separation upon entry. One end of the test section is connected to the flow delivery section the other end opens out to the room. The inflow conditions at the two ends are nearly symmetric and

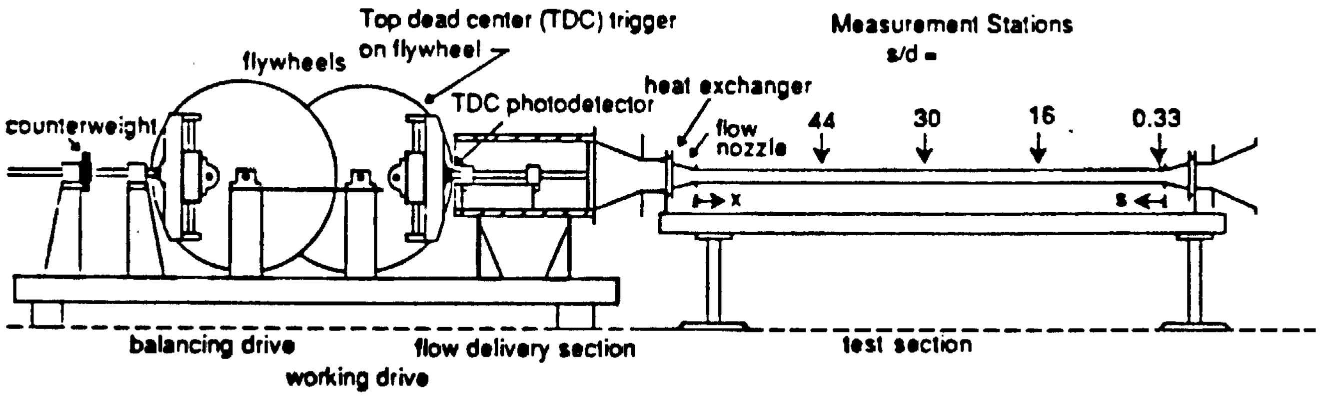

Figure 7.10. Side view of the oscillating flow rig at the University of Minnesotta. (Taken from Seume et. al.,1992)

the axial locations are represented by s/d where s is the distance from the open end of the test section and it is also the complement of x/d (s/d=1-x/d, where x is the distance from the drive end of the test section). The Table 7.1 below gives the dimensionless operating parameters for a typical heater tube of the Stirling engine, the experimental test and the numerical simulation.

Table 7.1 : Experimental and Numerical operating parameters.

Parameters	SPRE Heater	Experiment Test	Numerical Sim.
$Re_{\max}$	11700	11840	11840
Va	80.0	80.2	80.2
A_r	1.03	1.22	1.22
L/D_h	71.0	60.0	60.0

7.2.2 Experimental Observations

The preliminary experimental results carried out for different non dimensional parameters identified transition from laminar to turbulent flow by two mechanisms :

- Convective triggering by the incoming turbulent fluid.
- Instability of the developing boundary layer prior to the arrival of the convected turbulent fluid.

Based on this observations a semi-empirical transition model has been proposed (see Simon et. al.,1992) which accounts for the transition from laminar to turbulent flow effected by convective triggering of the incoming turbulent slug. The model is still in its seminal stages and hopes to improve the predictions for the skin friction and heat transfer coefficient by identifying the laminar and turbulent portions of the cycle at a given axial location. Further discussion of the model is beyond the scope of this study and can be found in Simon et al (1992).

7.2.3 Numerical results and Comparison

In order to correctly verify the numerical predictions care must be taken to accurately simulate the experimental conditions. Figures (7.11a) to (7.11d) shows how the friction factor compares against the experimental findings at the four axial locations, $x/d=$ 0.33,16,30,44 and the comparisons were made for the results obtained from the first oscillation cycle (i.e. the velocities have not settled to their quasi-steady states). The reason why the first oscillation cycle was chosen because the turbulent flow profiles, as was observed in the experiments, showed a cycle to cycle independence. That is, upon flow reversal the fluid was stagnant in the whole tube or had no history of the effects from previous cycle. A probable reason is due to the high mixing (turbulent diffusivity) capacities of turbulent flows, the velocity gradient near the wall were effectively smoothed out. Hence when the mean flow decelerates to zero velocity, the complete flow field in the tube also achieves no motion. Unlike in laminar flows, where due to relatively low diffusion the near wall velocity can be substantial compared to the core flow near flow reversal thus exhibiting a cyclic dependency. The experiments suggest a transient behavior in the sense that as the cycle begins slug (uniform inlet profile) fluid accelerates as a inviscid (flat velocity profile) flow close to the centerline of the tube having a growing boundary layer on the wall. These conditions are identical to when the fluid accelerates from rest in the beginning of first cycle even though the experimental data points are obtained after the flow has achieved a statistically steady state.

During the laminar portion of the cycle the friction factors predicted numerically at the four axial positions compare very well with the experimental data as shown in the Figures (7.11a)-(7.11d). The experimental data depart or show higher friction factors than the computed data after a particular velocity phase angle at each of the axial position except x/d=0.33. This phenomenon is attributed to the convective triggering of the boundary layer from laminar to turbulent flow due to the arrival of the turbulent slug. Whereas at x/d=0.33 which is close to the inlet the boundary layer is very thin and stable preserving its laminar state throughout the cycle, but as we go further down along the tube the growing boundary layer becomes very sensitive to the turbulent core and transitions to turbulent flow, resulting in higher skin friction coefficient. The reason for the high friction factor for the numerical results is that after the flow becomes turbulent the fully-developed turbulent flow correlations were used. This was done to test an empirical turbulence model (Simon et. al.,1992) for oscillatory flows to see how the predictions compare with the experimental result for the complete cycle. Also at x/D_h =0.33 the calculated friction factor are over predicted compared to the experimental data due to different inlet geometry and being close to the inlet sensitive to the "entrance" effects. But as one goes down the tube "entrance" effects subside and predictions improve expectedly.

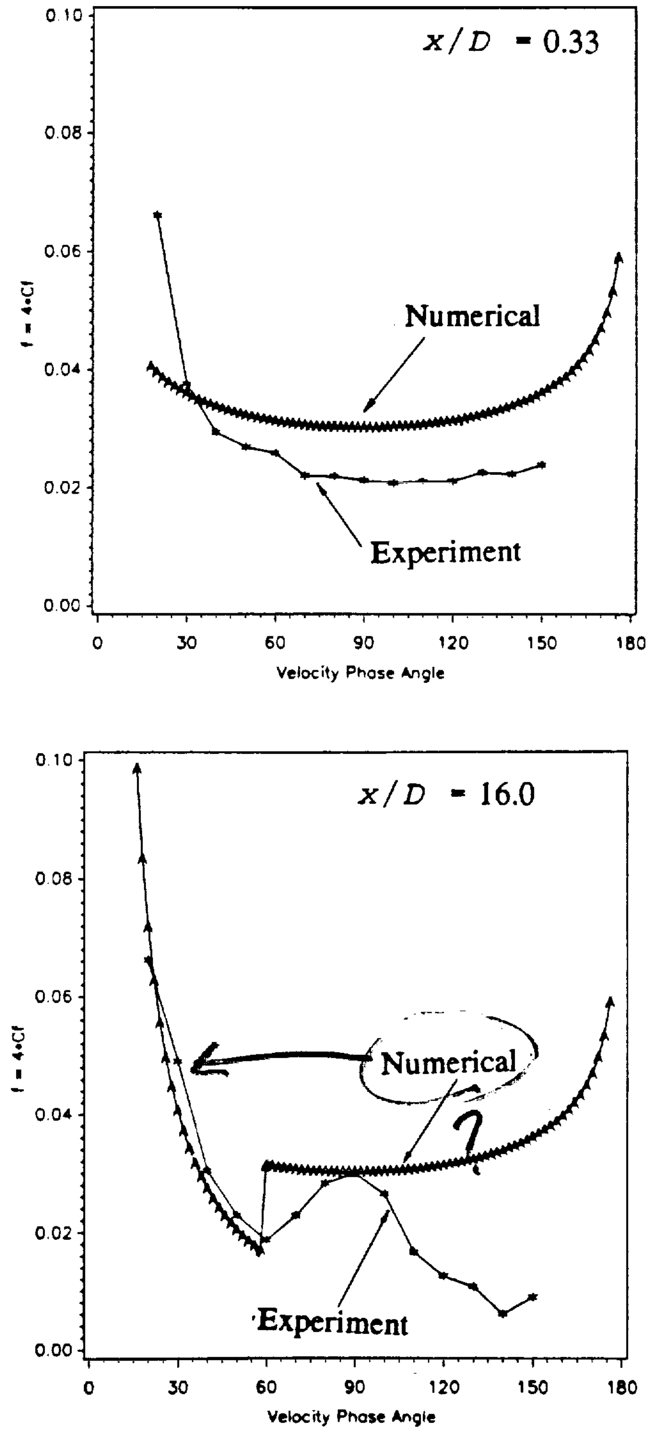

7.11 (a)

7.11 (b)

Figure 7.11 (a),(b),(c),(d). Comparison between Experimental and Numerical Moody friction factor plotted versus velocity phase angle at four different axial locations, namely,at $x/D = 0.33, 16.0, 30.0, 44.0$ respectively.

ORIGINAL PAGE IS
OF POOR QUALITY

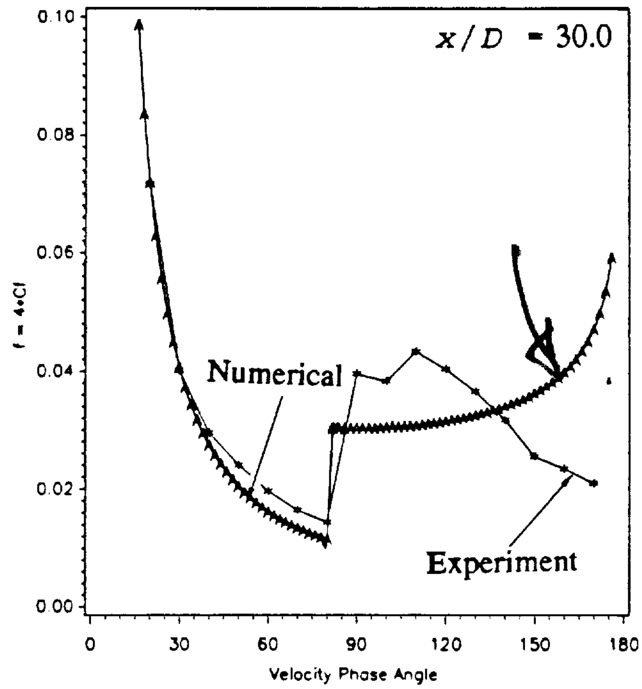

7.11 (c)

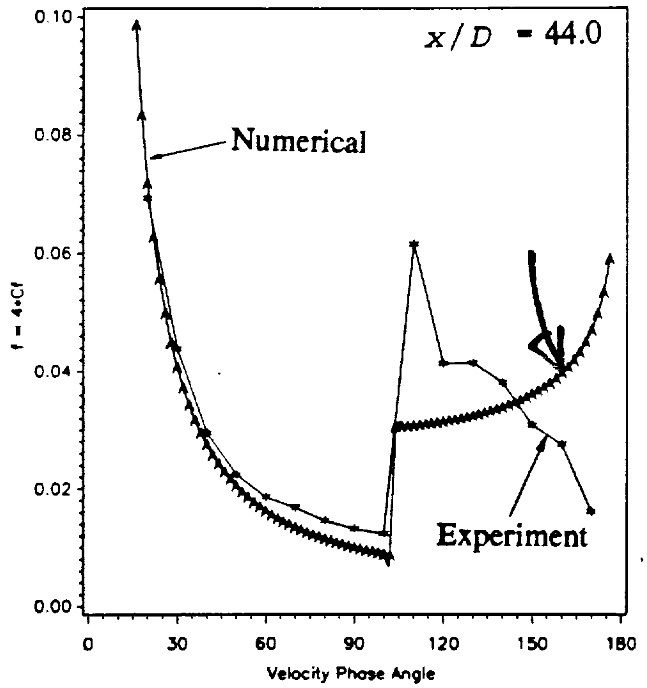

7.11 (d)

Figure 7.11 (a),(b),(c),(d). Comparison between Experimental and Numerical Moody friction factor plotted versus velocity phase angle at four different axial locations, namely,at $x/D = 0.33, 16.0, 30.0, 44.0$ respectively.

7.2.4 Brief Summary

The experimental setup has been described in sufficient detail and a basis for comparison with the numerical computations derived. The rationale for using transient as opposed to quasi steady computed data was explained since the experimental data was collected after the flow inside the tube achieved a statistically steady state or no cyclic variations. Finally the accuracy of the code is corroborated by good agreement with the experimental data in the laminar portions of the cycle.

7.3 Friction Factor and Entrance Effects

The pressure drop required to set the fluid in motion is dependent on the so called friction factor (C_f) which is a nondimensional wall shear stress (τ_w). In the design of heat exchanger it is very important to optimize between the thermal and friction losses. The C_f is one such quantity which gives an estimate of the pumping power required to set the fluid in motion in an heat exchanger. The C_f is defined as:

$$C_f = \frac{\tau_w}{(1/2)\cdot\rho\cdot U_i^2} \tag{7.15}$$

Here U_i is the average instantaneous velocity across the cross section of the channel. Hence it shoots to infinity at the flow reversal instants of the cycle (0°, 180° and 360°) by the above definition since the average instantaneous velocity is zero at these points in a oscillation cycle.

Figures 7.12, 7.13 and 7.14 plots the normalized friction factor versus the dimensionless axial distance at different velocity phase angles for the Cases C_2, C_5 and H_2 respectively. Only curves for half oscillation cycle (0° to 180°) is shown (excluding the flow reversal points) due to the symmetry (in time and space) and the definition of C_f. The friction factor is normalized by the *instantaneous* full developed steady state laminar friction factor correlation (.i.e. $C_f Re_i = 16$). In this particular half of the cycle the flow enters from the left end of the tube and exits at the right end of the tube (x/D_h = 0 to x/D_h = 60 or 70). From these figures the effect of Re_{max}, Va and A_r can be seen and these are described next.

The Re_{max} and A_r together control the magnitude or level of the friction factor and any instant of the cycle. From Fig. 7.12 and 7.13 representing cases C_2 and C_5 one can see that the C_f value is higher for case C_5 than for case C_2 because of the low A_r even though the $Re_{\max}$ is lower for case C_2. This is can be attributed to the fluid inertia associated with the smaller fluid penetration into the tube, hence more pumping power has to be introduced in the case of low A_r. In contrast the heater case H_2 has lower values of friction factor because of the high A_r (see Fig. 7.14). Although for the same value of relative amplitude of fluid displacement (A_r) the magnitude of the friction factor increases with $Re_{\max}$.

At some instants of the oscillation cycle the friction factor is negative, as can be seen from Figures 7.12-7.14 at 150° velocity phase angle. Though it is unrealistic for the C_f to be negative it simply means that the viscous forces augments the pressure forces. The negative value is caused by "backflow" at the walls or the velocities in a small viscous region close to the wall are flowing in a direction opposite to the primary flow direction. This situation is typical of high Va flows such as the cases C_2, C_5 and H_2, where the viscous effects are concentrated near a small region close to the wall (Stoke's layer) with an inviscid core. The "backflow" or flow reversal at the wall occurs in the decelerating portion of the cycle and happens earlier for higher Va which can be deduced from the Figures 7.12-7.14. It should be noted here that the "backflow" at the wall is characteristic of laminar oscillatory flows and does not exist when the flow is turbulent. The effect of flow reversal can also be noticed at the tube exit (x/D_h = 60 or 70) during the accelerating portions of the cycle (30°) wherein the friction factor drops to value lower than the asymptotic value. Another effect of Valensi number (Va) is the *amplitude* of the friction factor at any axial location decreases with the v_a (see Figures 7.12-7.14). The friction factor at any axial location is made up of a mean value plus a harmonic component, the amplitude here refers to the amplitude of the harmonic function.

The "entrance" effects are directly related to the A_r value. Since it is difficult to define fully developed flow in an unsteady situation it is difficult to define an "entrance" length for oscillatory flows using the standard definition used for steady or unidirectional flows. But for low A_r such as case C_5 (Fig. 7.13) the friction factor is almost constant along the length of the tube at any given time except for a small region close to the entrance. And, this small length of the tube (the "entrance" length) where the friction factor drops from infinity to the constant asymptotic value, grows longer as the cycle advances in time. Therefore the "entrance" length behaves unsteadily and for the case C_5 reaches a maximum value of 25 diameters ($x/D_h = 25$). Whereas for Cases C_2 and H_2 (Figures 7.12 and 7.14) the friction factor does not reach to an asymptotic value at any instant of the cycle hence an "entrance" length is hard to define. The reason C_f does not reach a asymptotic value can be ascribed to the high operating A_r values. But the drop in the value of friction factor from infinity to a lower value occurs over a small length for all the cases suggesting that the "entrance" effects are almost negligible. This observation is in contrast to steady flows where the "entrance" length increases with the Reynolds number.

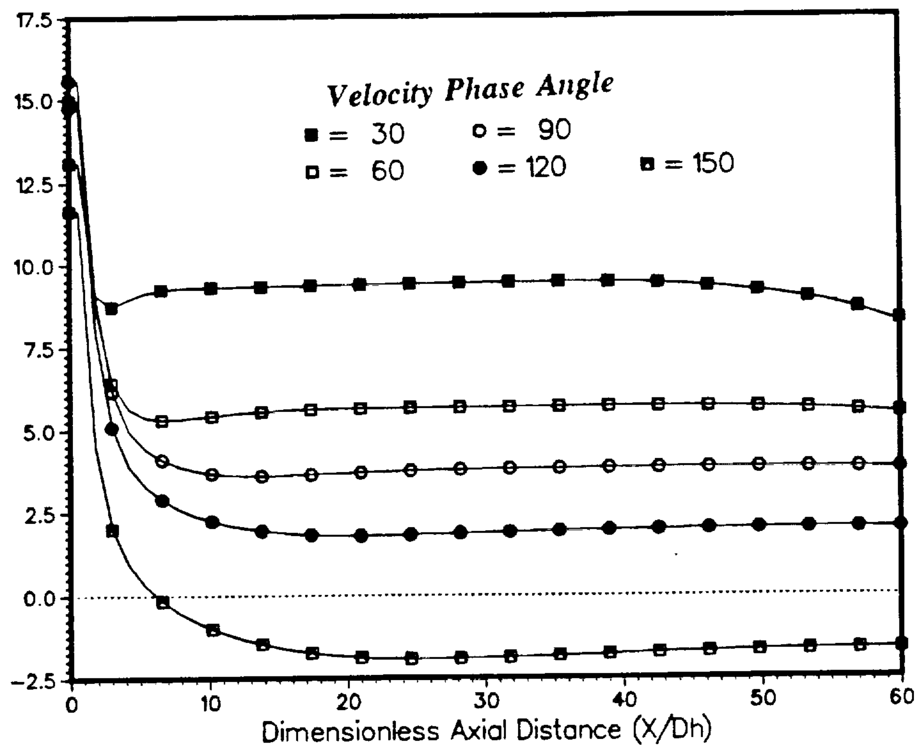

Figure 7.12. Normalized friction factor (C_f) versus the dimensionless axial distance at different velocity phase angles.
Case C_2 :: Re_{max}=30000, Va=350 and A_I=0.714.

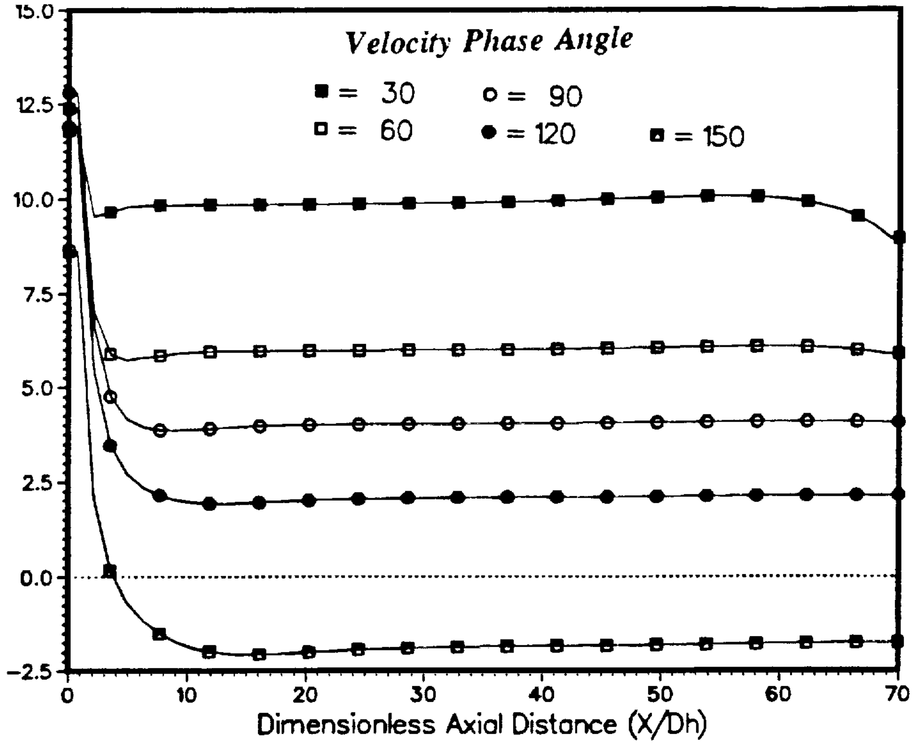

Figure 7.13. Normalized friction factor (C_f) versus the dimensionless axial distance at different velocity phase angles.
Case C_5 :: Re_{max}=20000, Va=400 and A_I=0.357.

Amplitude ↗ V ↗ $\left(\frac{\partial P}{\partial x}\right)$ ↗ ↗

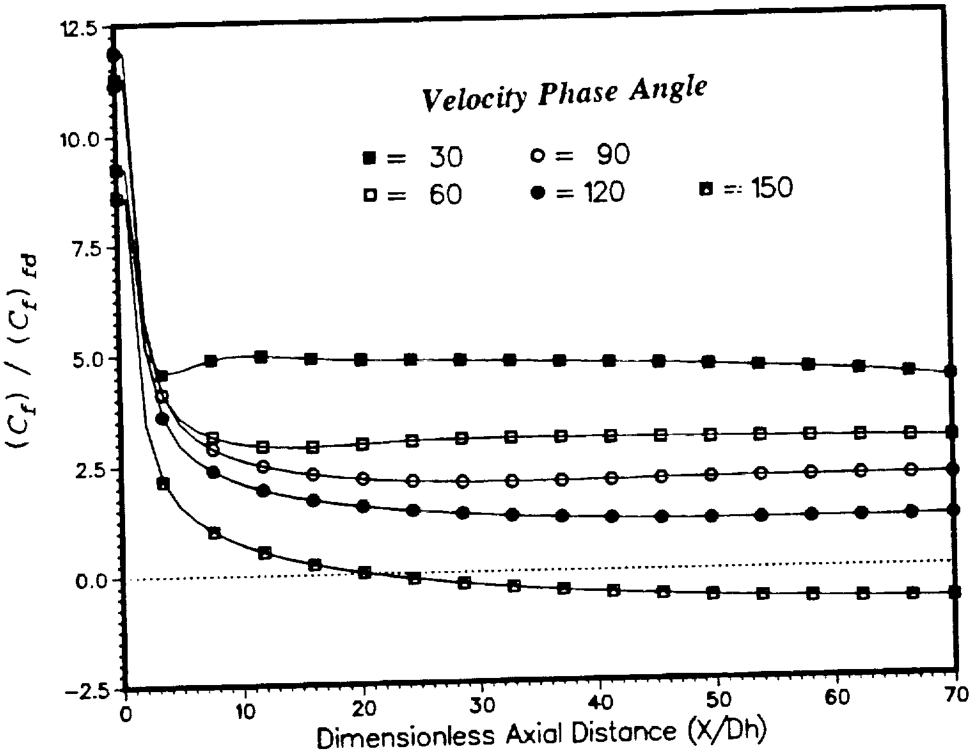

Figure 7.14. Normalized friction factor (C_f) versus the dimensionless axial distance at different velocity phase angles.
Case H_2 :: Re_{max}=16500, Va= 88 and A_r=1.34.

CHAPTER VIII

OSCILLATING FLOW HEAT TRANSFER

Once the momentum and continuity equations are solved for then the energy equation can be solved for the thermal field. In this chapter the results of the thermal analysis for the individual components of the Stirling engine are presented. First, the thermal analysis for the regenerator which is a conjugate heat transfer type problem is presented. In the section the code validation aspect is also covered. Second, the results for the heater and cooler are presented with two different type of boundary conditions (Symmetric and Asymmetric Inflow) are discussed and presented.

8.1 Conjugate Heat Transfer and Code Validation

In this section the conjugate heat transfer phenomena occurring in the regenerator of the Stirling engine is discussed. A comparison of the numerical predictions with the analytical results for the temperature profile is also made.

8.1.1 Kurzweg Analysis (Analytical Solution)

For the two-parallel-plates channel with solid walls and connected at the end to two reservoir at different temperatures (see Fig. 7.1), Kurzweg derived the solution for the temperature profile within the channel and the solid. This phenomenon is very similar to the one occurring in the regenerator of a Stirling engine. In the Stirling engine the regenerator is placed between the cooler and the heater which ensures a temperature gradient between the ends of the regenerator throughout the cycle. In the first half of the cycle the flow enters from the hot end and heat is absorbed by the regenerator and in the next half cycle when the flow enters from the cold end the absorbed heat is released to the cold fluid. Thus regenerator acts as a heat source or heat sink during a complete cycle.

The temperature profile for along the channel for a fully developed velocity was derived by Kurzweg (1985a) for the geometry show in Figure 7.1. He assumed the temperature profile to be given by:

$$T(x,y,t) = [T_x + \gamma\, a\, g(\eta)\, e^{i\omega t}] \qquad (8.1)$$

Here the term T_x is the constant linear temperature gradient along the channel i.e. the temperature is assumed to be varying across the channel (normal y direction) superimposed on a constant axial temperature. And the function $g(\eta)$ captures the variation in the normal direction and for the fluid region is given by $g_f(\eta)$:

$$g_f(\eta) = K_1 cosh\,(\sqrt{iPr}\,\alpha\,\eta) + \frac{\lambda Pe}{\alpha^4 Pr(Pr-1)} + \frac{iPe}{\alpha^2(Pr-1)} f(\eta) \qquad (8.2)$$

and for the solid portion is given by $g_s(\eta)$:

$$g_s(\eta) = K_2 \cosh\left[\sqrt{i\sigma Pr}\,\alpha\,(\epsilon - \eta)\right] \tag{8.3}$$

The constants K_1 and K_2 are:

$$K_1 = \frac{-\lambda Pe}{\alpha^4\,(Pr-1)\,Pr\cosh\left[\sqrt{iPr}\,\alpha\right]}\left\{\frac{\kappa\sqrt{Pr}\,\tanh\left[\sqrt{i\alpha}\right] + \sqrt{\sigma}\,\tanh\left[\sqrt{i\sigma Pr}\,\alpha\,(\epsilon-1)\right]}{\kappa\tanh\left[\sqrt{iPr}\,\alpha\right] + \sqrt{\sigma}\,\tanh\left[\sqrt{i\sigma Pr}\,\alpha\,(\epsilon-1)\right]}\right\} \tag{8.4}$$

$$K_2 = \frac{K_1\cosh\left[\sqrt{i\,Pr}\,\alpha\right] + \dfrac{\lambda Pe}{\alpha^4\,Pr\,(Pr-1)}}{\cosh\left[\sqrt{i\sigma Pr}\,\alpha\,(\epsilon-1)\right]} \tag{8.5}$$

8.1.2 Numerical Predictions and Comparison

Cases R_1 and R_2 are the test cases used to compare the numerical predictions for the conjugate heat transfer problem with the Kurzweg analysis (1985a) presented above. The operating parameters for these cases are listed in Table 8.1. Since the solution for the temperature profile (Eqs. 8.1-8.5) are based on the flow being driven by a sinusoidally varying pressure gradient they have to be modified to account for the sinusoidal velocity input boundary conditions.

Table 8.1: Test cases investigated for the conjugate heat transfer.

TEST CASE	Re_{max}	Va	L/D_l	T_{wall}	T_{west}	T_{east}	A_r
R_1	75	2.5	60	n/a	274	273	0.250
R_2	12000	400	60	n/a	274	273	0.250

Essentially this involves two changes, first there will be a phase difference (ϕ_T) added to the time variable (ωt) and the function $f(\eta)$ in Eq. (8.2) should be replaced by $f_n(\eta)$ found from Eq. (7.8). The rationale behind this was explained in the fluid flow section. With these modifications the analytical temperature profile for a sinusoidal velocity input is given by:

$$T(x,y,t) = [\, T_x + \gamma a g(\eta)\, e^{(i\omega t + \phi_T)}\,] \tag{8.6}$$

Where $g(\eta)$ is got from Eq. (8.2) or Eq. (8.3) depending on the fluid or the solid portion respectively. As mentioned earlier the function $f(\eta)$ should be replaced by the function $f_n(\eta)$ given by eq. (7.8). The phase difference is given by:

$$\phi_T = 180^o + \phi_U \tag{8.7}$$

The ϕ_U is gotten from eq. (7.6) and the 180° addition is due to the fact that the temperature gradient (γ) used by Kurzweg is opposite in sign to the one used by the numerical simulation.

Figure 8.1 shows the temperature profile for case R_1, Re_{max}= 75 and Va= 2.5. The instantaneous temperature ($T - T_x$) or more appropriately the instantaneous temperature fluctuation is plotted versus the normalized distance from the centerline to the wall (y direction) at different velocity phase angles (from 30° to 360° with 30° increment). The symbols are used for the analytical solution and the dotted line for the present work, the profiles were compared at the axial mid plane ($L/2$) so that the entrance effects are negligible. Since the Valensi number (Va) is low the profile exhibits the familiar parabolic shape as found in the steady state solution. Also the temperature

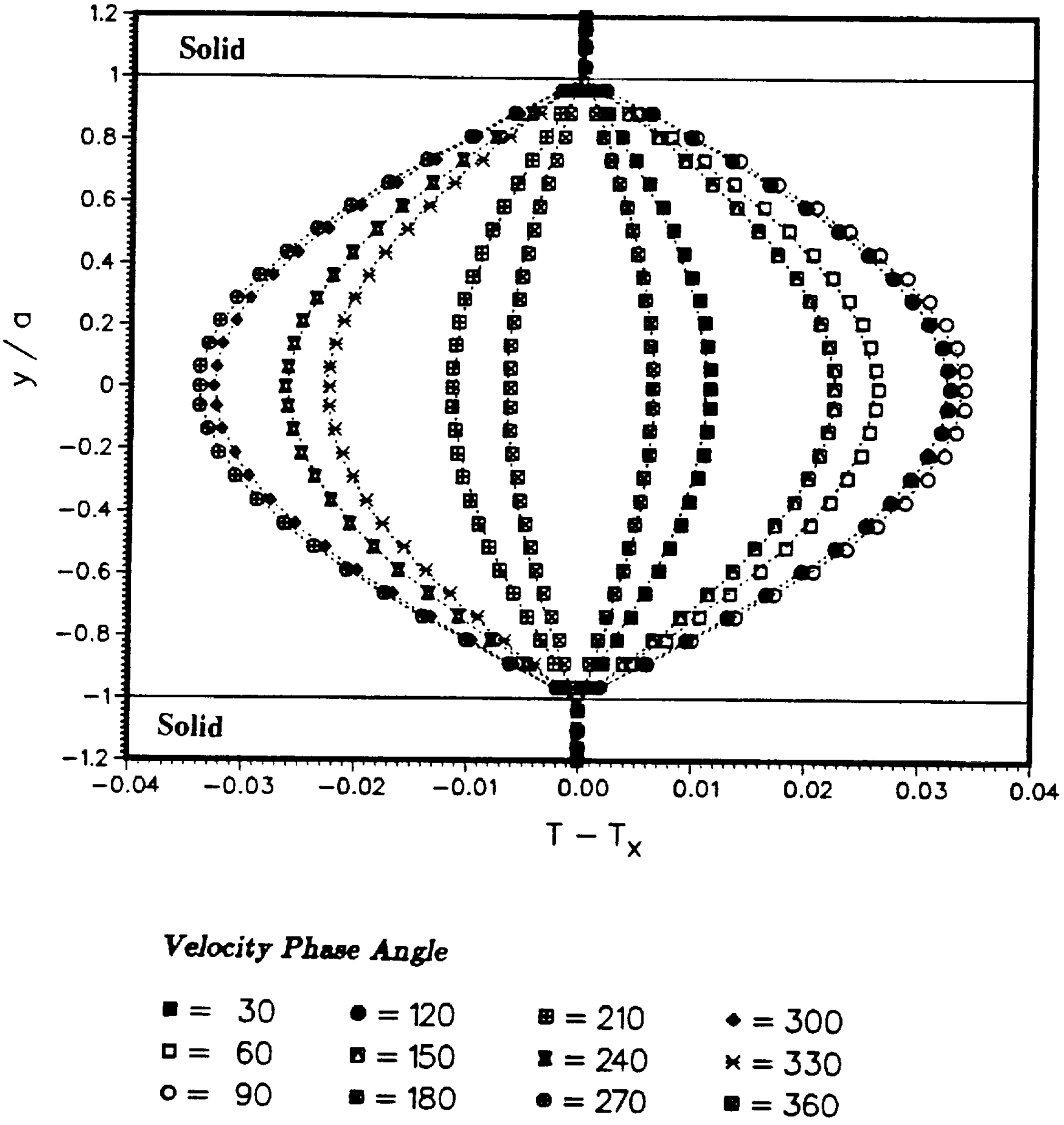

Figure 8.1. Comparison between analytical and numerical temperature profiles at different velocity phase angles for the conjugate heat transfer problem, Case R_1 :Re_{max}=75 and Va=2.5.
[Symbols : Analytical-Kurzweg ;; Dotted Lines : Numerical]

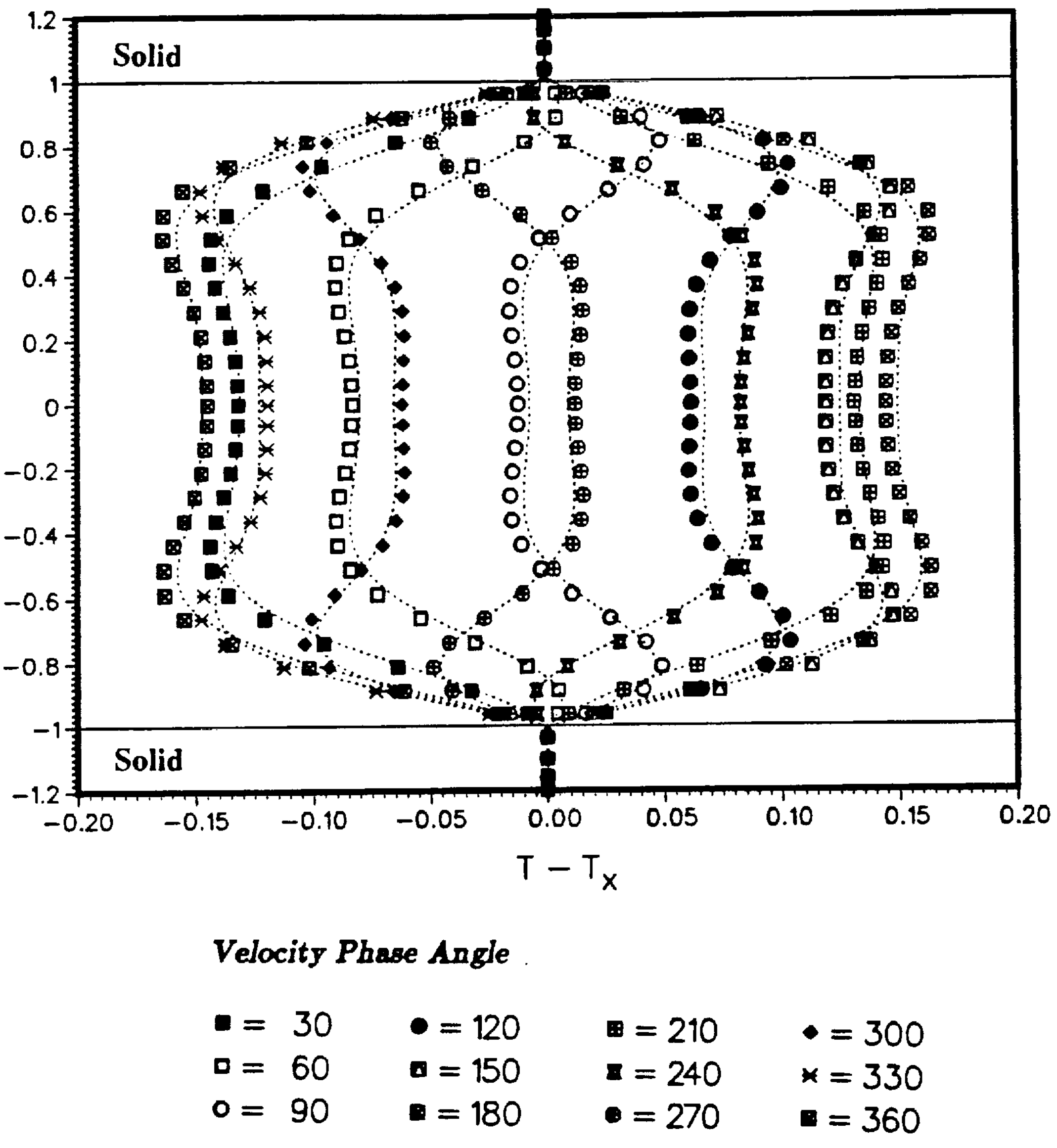

Figure 8.2. Comparison between analytical and numerical temperature profiles at different velocity phase angles for the conjugate heat transfer problem, Case R$_2$: Re_{max}=12000 and Va=400.
[Symbols : Analytical-Kurzweg ;; Dotted Lines : Numerical]

gradient at the wall changes sign with the flow reversal or the wall heat flux is in phase with the mean or inlet velocity. The temperature fluctuation is almost zero in the solid because of the high heat capacity of the solid hence the constant K_2 in Eq. (8.3) tends to zero with the result that $g_s(\eta)$ is zero for the whole cycle. Otherwise for low Va and low σ (ratio of heat capacities of the solid and fluid) the temperature fluctuations within the solid is as high as in the fluid.

Figure 8.2 shows a similar figure for case R_2, Re_{max}= 12000 and Va= 400 which is a high Va case. Some interesting points to notice about this case are the presence of an inviscid core just like in the velocity plots due to the high frequency and the sharp temperature gradient at the wall which is out of phase with the incoming fluid. Also the temperature fluctuation is zero within the solid due to both the high heat capacity of the solid and the high Va. In fact one of the effects of high frequency on the temperature fluctuations in the solid (for a low heat capacity) is to bring the fluctuations down to zero. But due to both these factors present in this particular case it is difficult to isolate which has a more pronounced effect on the temperature distribution. Further the temperature fluctuation for case R_2 is more ($\mp$0.17) than for case R_1 ($\mp$0.035) which is a direct of the frequency or the presence of an inviscid core.

Form Figures 8.1 and 8.2 one can clearly see that the agreement between the analytical solution and the numerical predictions are excellent. The reason for the poor agreement for the high Va case than the low Va can be attributed to the limitation of the machine in evaluating complex numbers algebra. Therefore special limiting procedures had to be performed on Eq. (8.2)-(8.5) so as to simplify them.

8.2 Symmetric Temperature Inflow

The results for the heat transfer in circular tubes for a symmetric temperature inflow conditions with constant wall temperature are presented now. This type of heat transfer situation is close to what is found in the cooler and heater tubes of a Stirling engine. Table 8.2 lists all the cases investigated which cover a wide range of Re_{max}, Va and A_r. All the cases beginning with "C" stand for the cooler conditions and "H" for the heater conditions. In all the cases the flow enters the tube from the west end of the tube for the first half cycle (0° to 180°), and then reverses and enters from the east end of the tube for the next half cycle (180° to 360°). In the case of symmetric inflow the flow enters the tube with the same constant temperature (enthalpy) for both half cycles. All the calculations were done for 52x52 grid and the runs were made on a Cray YMP 8/8128 (sn 1040). Each run took approximately 1000s of CPU time for each cycle and at least 3 cycles were needed for cyclic convergence or for the temperature profile to settle down from one cycle to the other. The computaional domain with the appropriate boundary conditions is sketched in Fig. (8.3), due to symmetry the computations were done only for half of the tube.

8.2.1 Temperature Profiles

Figures 8.4 and 8.5 are 3D plots for the nondimensional temperature profiles for the whole tube for two cooler cases with the same A_r. The nondimensional temperature ($|(T-T_w)/(T_{in}-T_w)|$) is plotted against the pipe radius and the axial distance at different velocity phase angles (from 0° to 180° with 30° increment). Since the temperature inflow is symmetric the other half cycle is a mirror image of the events

Table 8.2: Test cases investigated for symmetric temperature inflow.

TEST CASE	$Re_{\max}$	Va	L/D_l	T_{wall}	T_{west}	T_{east}	A_I
C_1	15000	175	60	325	340	340	0.714
C_2	30000	350	60	325	340	340	0.714
C_3	60000	700	60	325	340	340	0.714
C_4	10000	200	70	325	340	340	0.357
C_5	20000	400	70	325	340	340	0.357
C_6	40000	800	70	325	340	340	0.357
H_1	8250	44	70	650	620	620	1.340
H_2	16500	88	70	650	620	620	1.340
H_3	33500	176	70	650	620	620	1.340

occurring in the first half. The direction of the flow is pointed by the thick bold arrow at any instant of time.

Fig. 8.4 shows the cooler case C_2 ($Re_{\max}$= 30000, Va= 350, L/D_h= 60 and A_r= 0.714), the flow enters with constant temperature (340 °K) and gets cooled due to the presence of a cold wall maintained at a constant temperature T = 325 °K. One can see as the cycle proceeds the thermal front advances into the tube but due to the high Va the profile across the radius does not develop into the familiar parabolic shape. The cooling process occurring is very complex due to the presence of cold and hot regions, at the beginning of the cycle (0°) the fluid is cooler at the entrance (for this part of the cycle) x/D_h = 0 than at the exit x/D_h = 60. The presence of these cold and hot "spots" effects the heat transfer mechanism in the tube as the flow proceeds along the tube. If one looks at the trace of the centerline (r=0) throughout the half cycle (0° to 180°), the temperature drops to a minimum at some axial location at any point in the cycle and then monotonically increases due to the presence of the hot spot ahead (in the axial direction). During the course of the cycle as the thermal front advances this temperature minimum moves further down the tube or closer to the exit and the A_r being less than 1, this minimum temperature stays within the tube. Further due to the high Va the temperature gradient at the wall (r= ± 0.05) is very steep suggesting a high wall heat flux.

Fig. 8.5 shows a similar 3D plot for case C_1 ($Re_{\max}$= 15000, Va= 175, L/D_h= 60 and A_r= 0.714), the cooling mechanism is similar to the one described for case C_2 except for few perceptible differences. The Valensi number (Va) for this case being lower than case C_2 the hot temperature core is thinner than the previous case which makes

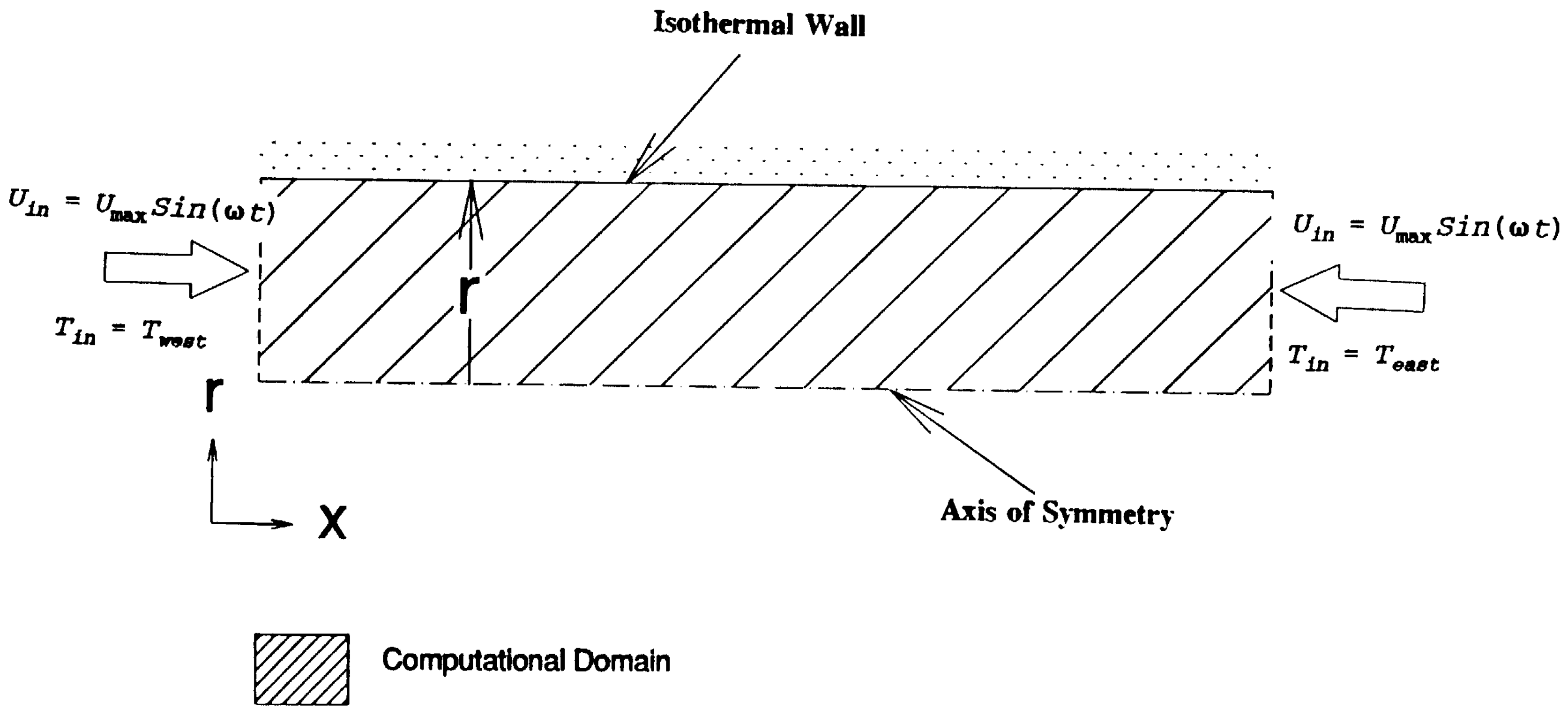

Figure 8.3. Geometry for flow inside Circular tube showing the computaional domain and Symmetric temperature inflow conditions.

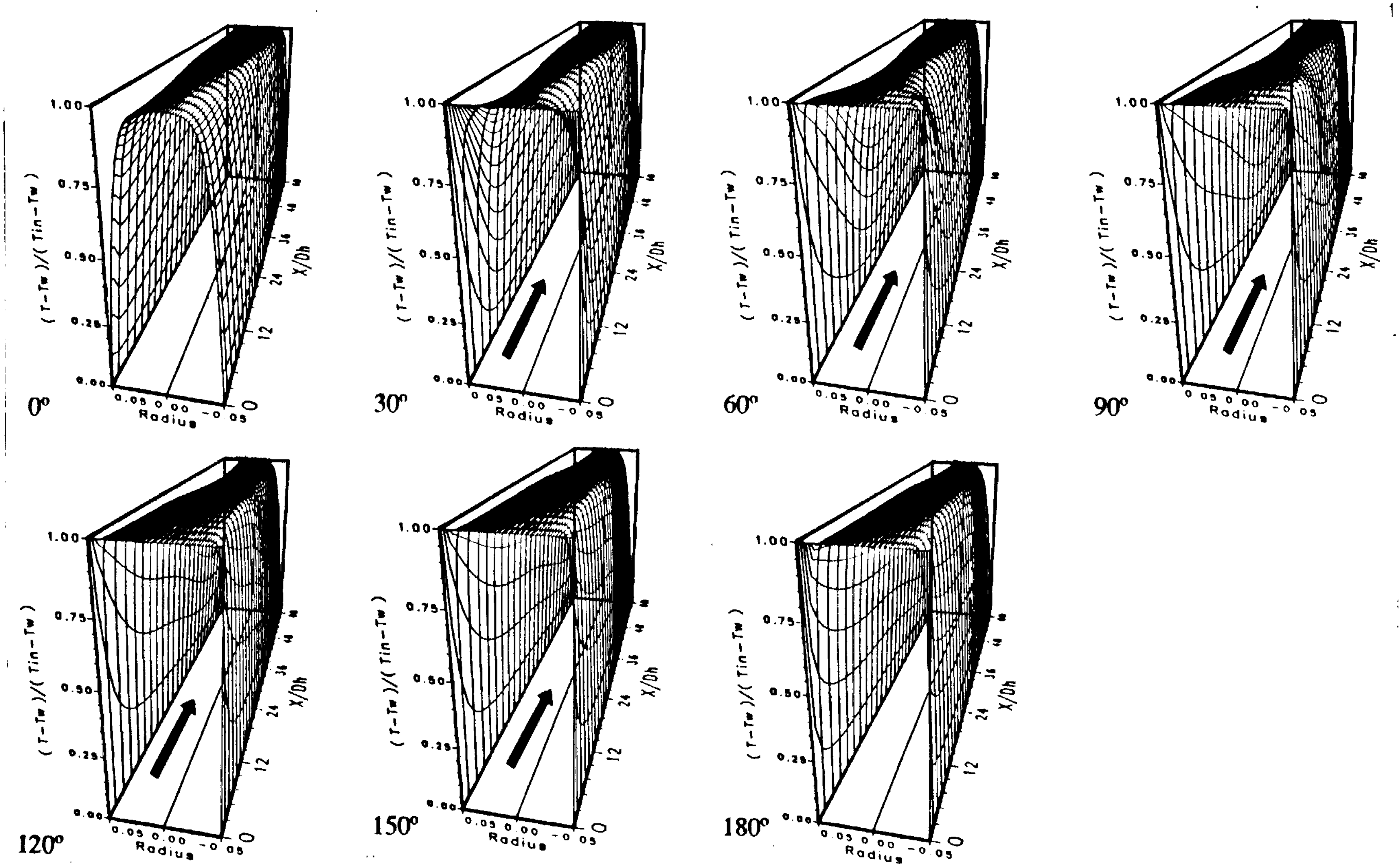

0°

30°

60°

90°

120°

150°

180°

Figure 8.4 Three-Dimensional normalized temperature plots at different velocity phase angles for the circular pipe symmetric temperature inflow problem:
Case C_2: Re_{max} = 30000 and Va = 350.

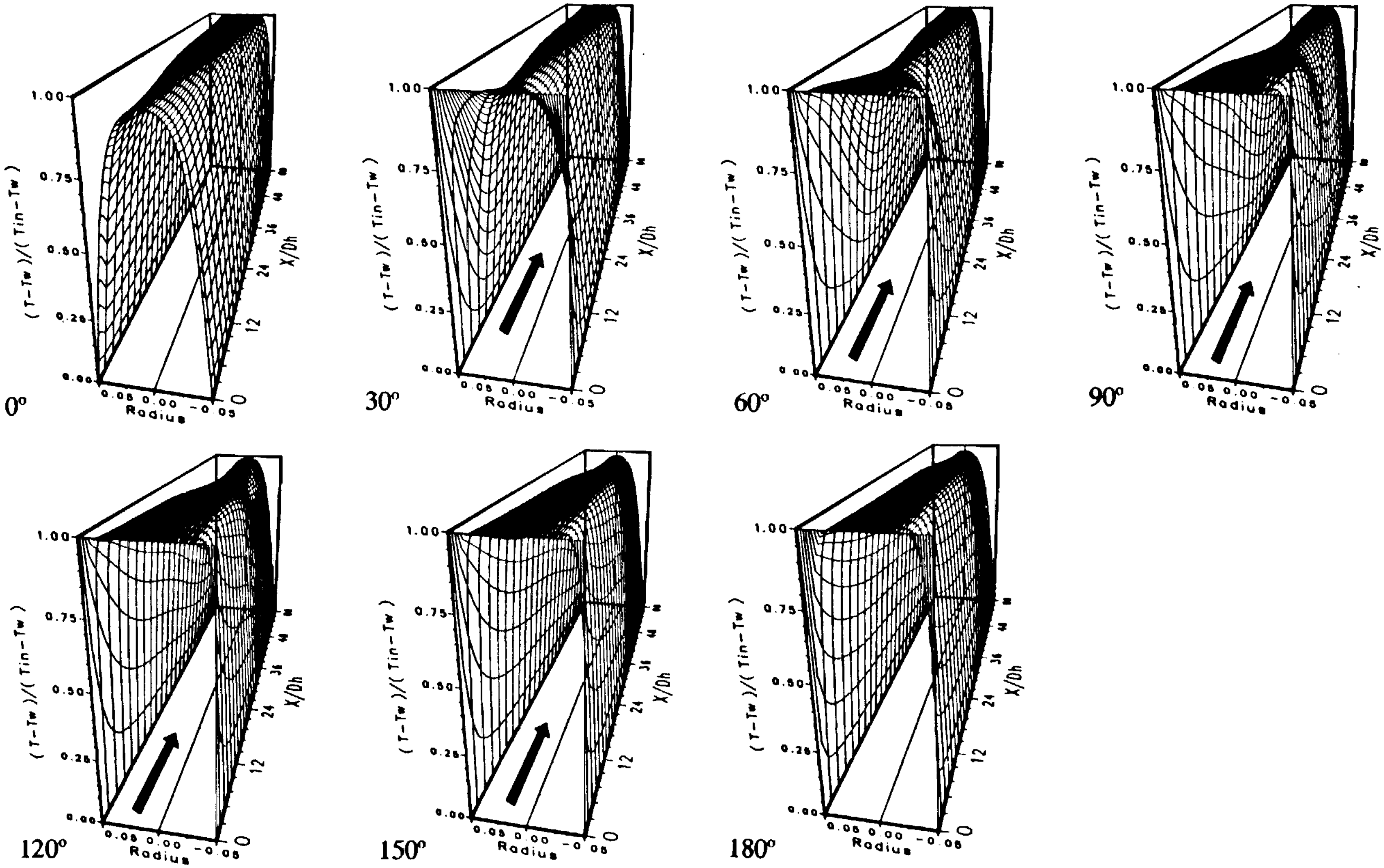

0° 30° 60° 90°

120° 150° 180°

Figure 8.5 Three-Dimensional normalized temperature plots at different velocity phase angles for the circular pipe symmetric temperature inflow problem:
Case C_1: $Re_{max} = 15000$ and $Va = 175$.

the temperature profile to be closer to a parabola (e.g. see at 0° velocity phase angle at x/D_h =0). Also the temperature gradient of the wall is less steeper thus implying a lower wall heat flux. Figures 8.4 and 8.5 one can notice the effect of same A_r by the maximum penetration distance of the thermal front into the tube which is the same, despite the wall heat flux being different. The temperature profiles are effected due to different Va.

Figures 8.6 and 8.7 are 3D plots for cases H_2 (Re_{max}= 16500, Va= 88, L/D_h= 70 and A_r= 1.34) and C_5 (Re_{max}= 20000, Va= 400, L/D_h= 70 and A_r= 0.357) respectively. Each case is for different A_r and case H_2 is representative of the operative conditions of a heater in the Stirling engine where case C_5 was chosen to isolate the effect of the relative amplitude of fluid motion. Once again the nondimensional temperature is plotted against axial distance (x/D_h) and the radius of the tube (r). In Fig. 8.6 which is the heater case H_2, one can observe that as the cycle proceeds the thermal front has penetrated the whole axial distance and the cold "spot" which exists at the exit (x/D_h= 70) is pushed out completely from the tube (at 90°). Whereas for the case C_5 shown in Fig. 8.7 the hot "spot" (since it is run as a cooler) exists throughout the half cycle. Also one can notice that lower the Valensi number (Va) the more parabolic the profile is ahead of the thermal front (or the inviscid hot or cold temperature core is thinner for low Va.

8.2.2 Contour Plots

In this section the temperature contours for three of the cases listed in Table 8·2 ~~7.X~~ will be presented and discussed. These contour plots augments the discussion presented in the temperature profile section (see above).

Figure 8.8 shows the temperature contours at different velocity phase angles for

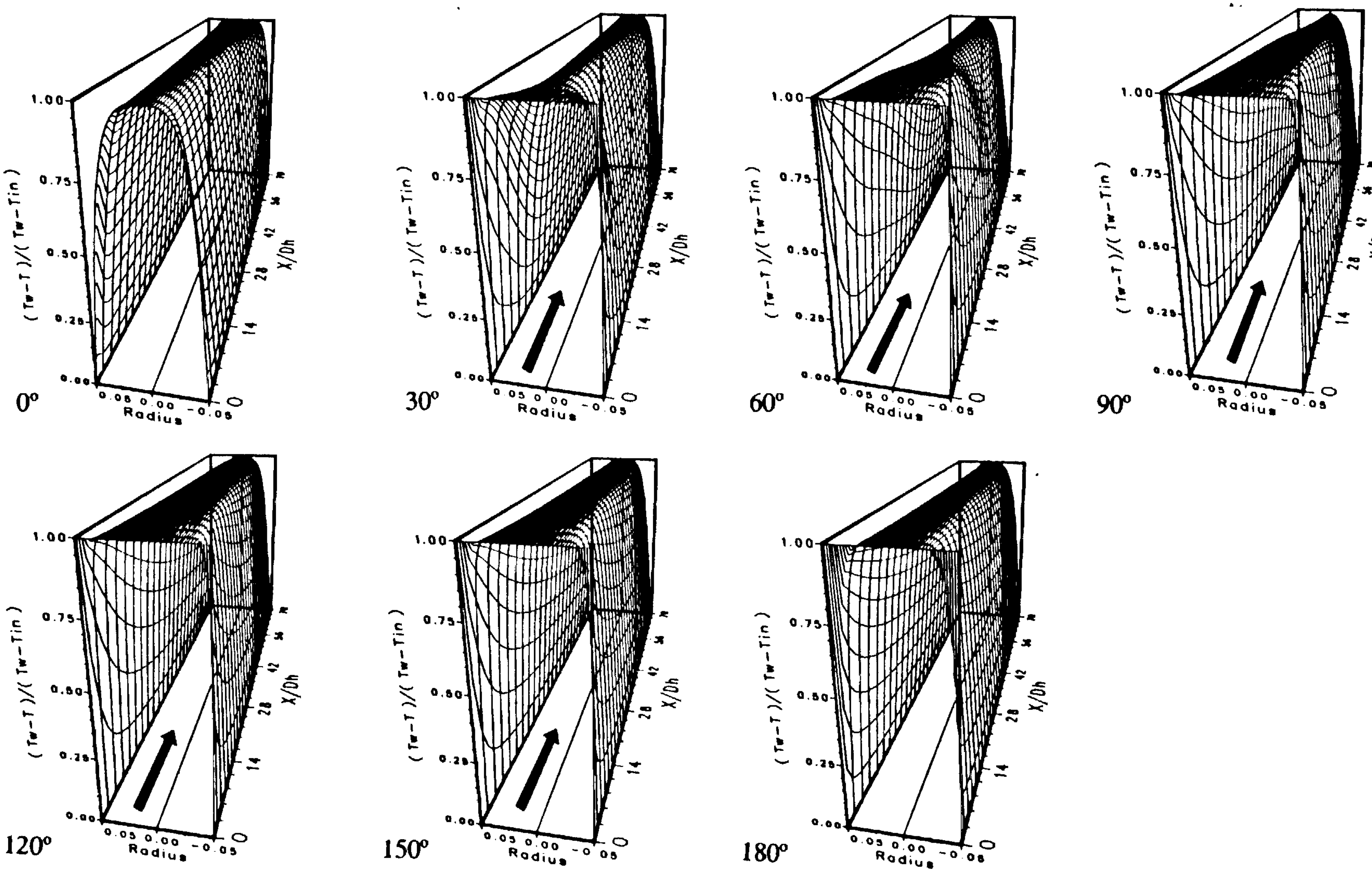

Figure 8.6 Three-Dimensional normalized temperature plots at different velocity phase angles for the circular pipe symmetric temperature inflow problem:
Case H_2: Re_{max} = 16500 and Va = 88.

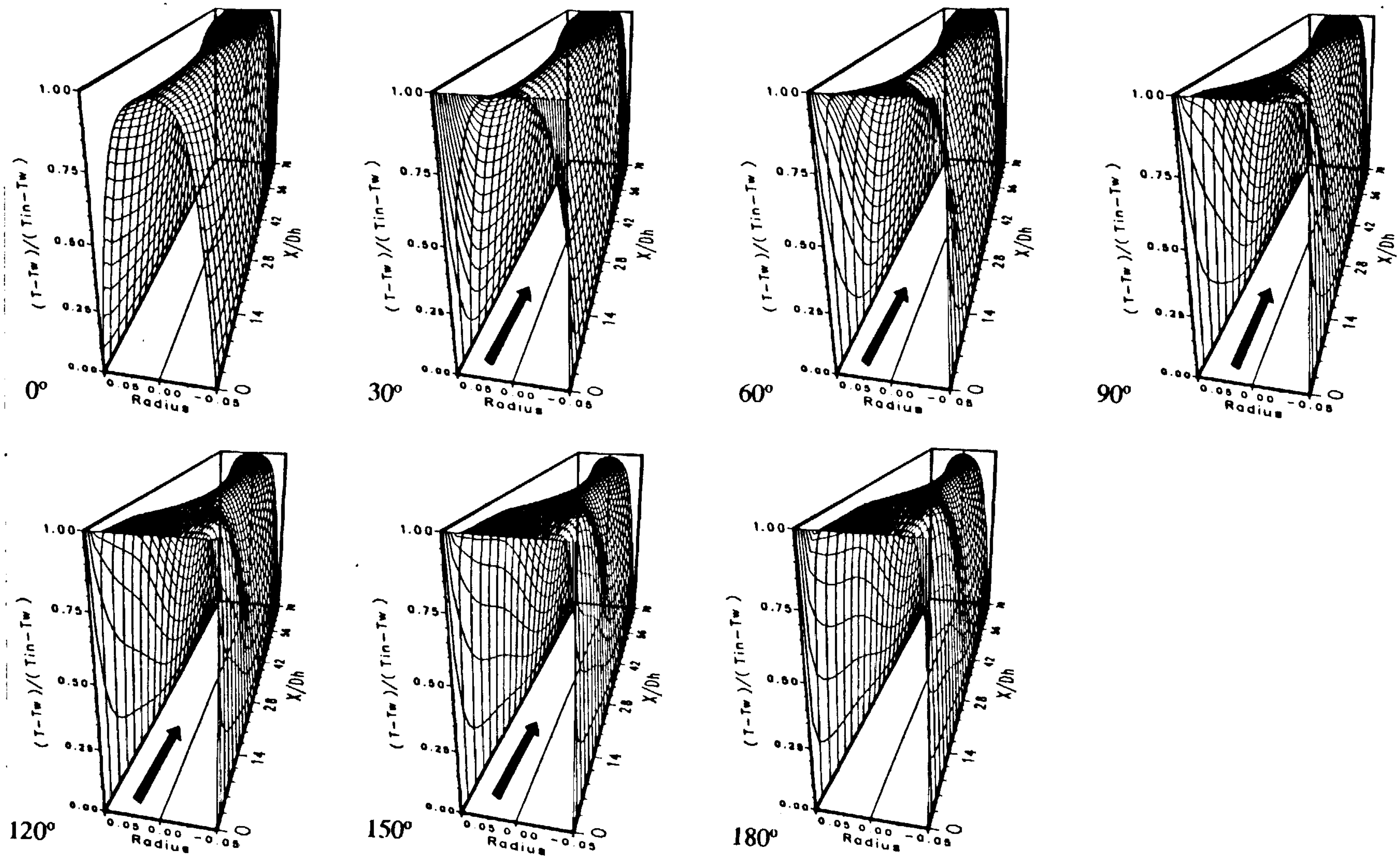

Figure 8.7. Three-Dimensional normalized temperature plots at different velocity phase angles for symmetric inflow temperature problem.
Case C_5 : $Re_{max} = 20000$ and $Va = 400$

case C_2 (A_r = 0.714). Again the contours are shown only for half of the cycle (0° to 180°) due to symmetrical inflow conditions with the hot fluid entering the tube (at T= 340 °K) while the wall is maintained at a colder temperature (at T= 325 °K). At the beginning of the cycle (0°) one can see the presence of hot fluid in the core of the tube (bigger at the east/left end of the tube) due to the history of hot fluid from the previous cycle. As the cycle proceeds during the acceleration portion (0° to 90°) advances down the tube and continues to advance during the deceleration portion of the cycle (90° to 180°) although at a slower rate. On the other hand the residual hot front from the previous cycle is retreating out of the tube during the acceleration portion of the cycle and disappears completely during the deceleration portion of the cycle (90° to 180°). The presence of two hot fronts (one close to the entrance and the other close to the exit), in most of the cycle, is attributed to the Re_{max} being less than 1.

Figure 8.9 shows the temperature contours for the heater case H_2 (A_r = 1.34). The contours are shown only for half a cycle (0° to 180°) with cold fluid (heater) entering the tube (T = 620 °K) while the wall being maintained at a hotter temperature (T = 650 °K). In this case the cold front advances into the tube from the left end during the acceleration portion of the cycle and continues to advance during the deceleration portion of the cycle. Whereas the residual cold front present at the right end of the tube (at 0°) is pushed out of the tube during the acceleration portion and disappears completely during the deceleration portion of the cycle. It is interesting to note that the core of cold fluid in the tube is thinner than the case C_2 (Fig. 8.8) due to lower Va.

Figure 8.10 shows the temperature contours for the cooler case C_5 (A_r = 0.357).

Again, due to symmetrical inflow conditions the temperature contours are shown only for half a cycle. The hot fluid enters the tube at $T = 340$ °K while the wall is maintained at a colder temperature (at $T = 325$ °K) so as to allow the incoming fluid to cool. Just like in the previous two cases the entering hot thermal front advances into the fluid during the acceleration portion and continues to advance but at a slower rate during the deceleration portion of the cycle. Further the residual hot front concentrated near the exit (right end) retreats out of the tube as the cycle advances but, contrary to the previous two cases, does not disappear completely from the tube at end of the half cycle. This can be attributed to the very low value of A_r (0.357). Despite the high Va the hot fluid core is thinner at the axial center of the tube than at the ends of the tube which is due to the very low A_r. Since the hot thermal front does not penetrate completely into the tube this means that around the axial center of the tube (away from the ends) the heat transfer mechanism is dominated by molecular conduction than by convection. This implies that heat transfer rate is very poor away from the ends.

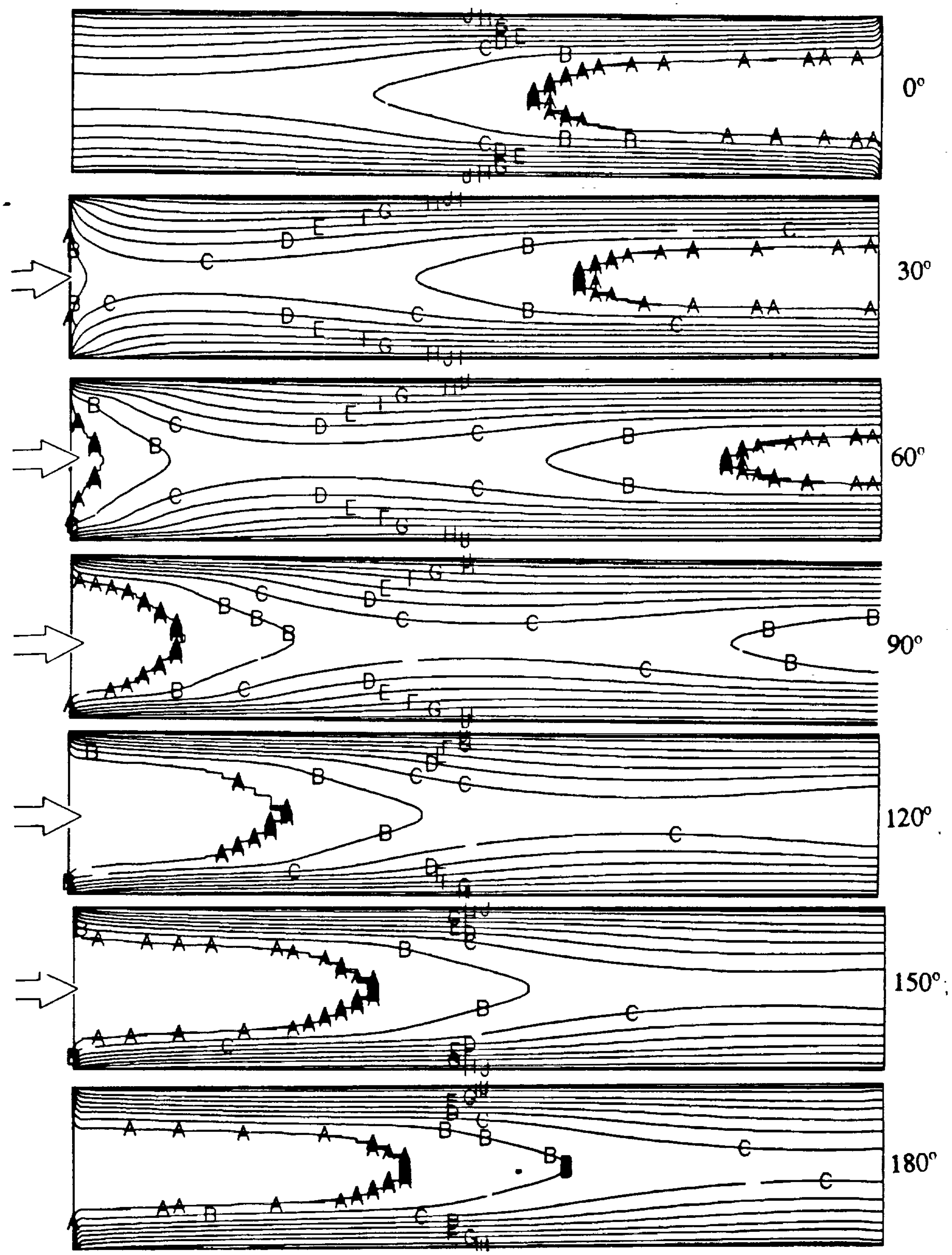

Figure 8.8. Temperature contours at different velocity phase angles for the symmetrical temperature inflow problem: Case C_2 $Re_{max} = 30000$ and $Va = 350$.

[A: 340.00, B: 339.99, C: 339.92, D:339.70, E: 339.10
F: 337.50, G: 335.00, H: 330.00 , I:327.50, J: 326.50]

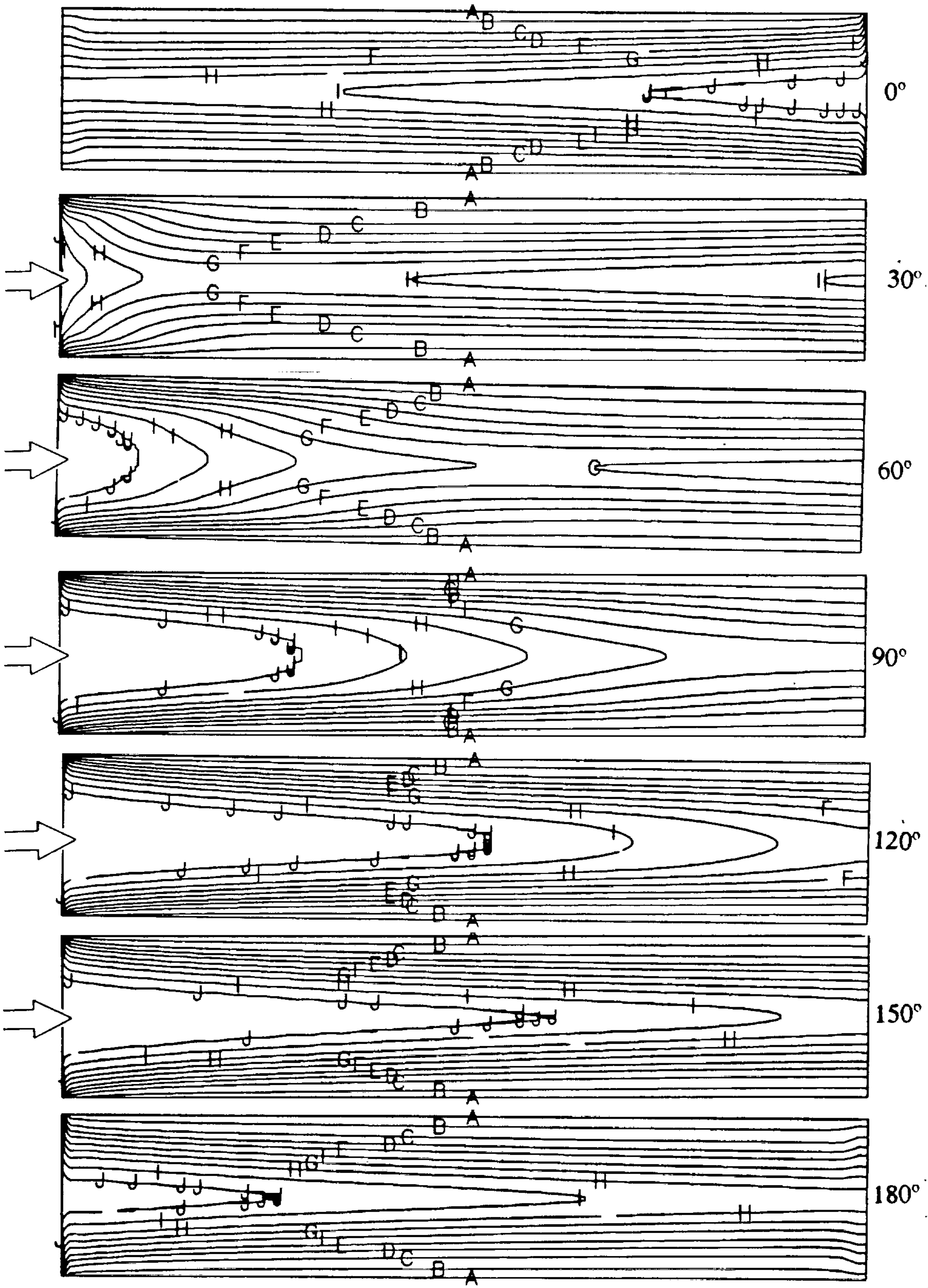

Figure 8.9. Temperature contours at different velocity phase angles for the symmetrical temperature inflow problem: Case H_2 Re_{max} = 16500 and Va = 88.

[A: 649.50, B: 640.00, C: 630.00, D: 625.00, E: 622.50
F: 620.90, G: 620.30, H: 620.08 , I: 620.01, J: 620.00]

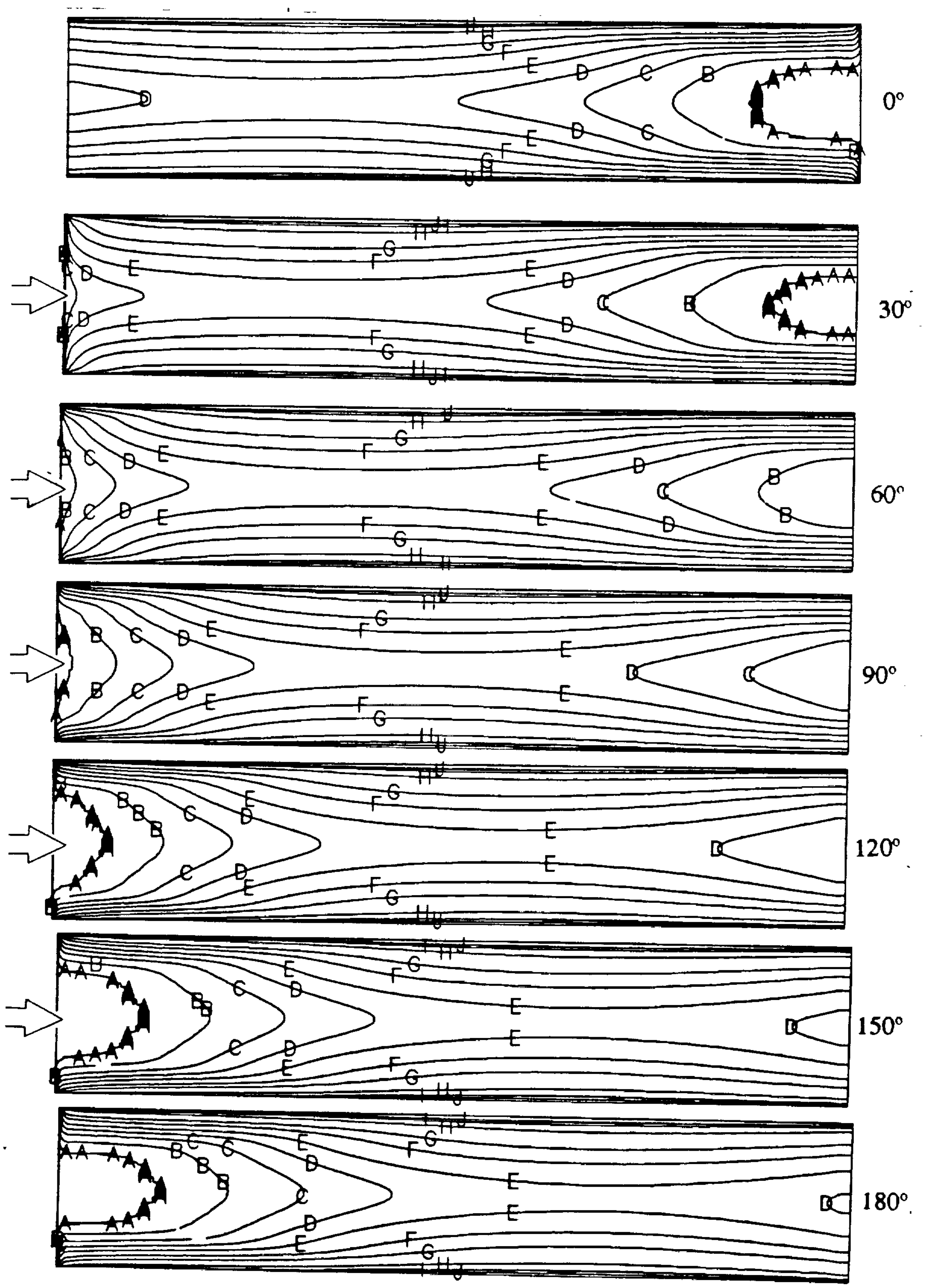

Figure 8.10. Temperature contours at different velocity phase angles for the symmetrical temperature inflow problem: Case C_5 $Re_{max} = 20000$ and $Va = 400$.

[A: 340.00, B: 339.99, C: 339.92, D:339.70, E: 339.10
F: 337.50, G: 335.00, H: 330.00 , I:327.50, J: 326.50]

8.2.3 Section Average Temperature (T_a)

Figures 8.11-8.13 shows the normailzed section average temperature (T_a) across the cross-section of the tube versus the dimensionless axial distance (x/D_h) at different velocity phase angles for three cases. The section average temperature is a area weighted temperature across the tube and is defined as:

$$T_a = \frac{\int TdA}{A} \tag{8.8}$$

Here dA is an element of cross-section area, and A is the total cross-sectional area of the tube or channel. All the figures (8.11-8.13) are shown only for half of the oscillation cycle due to the symmetrical inflow.

Figure 8.11 shows the normalizd T_a versus x/D_h for the cooler Case C_2 (Va =350) at different velocity phase angles. At the beginning of the cycle (0°) most of the fluid is hot at x/D_h =60 and cold at x/D_h =0 due to the hotter fluid leftover from the prvious half-cycle. As the flow accelerates the fluid cools rapidly due to the presence of the cold wall and the cold fluid present close to the entrance (x/D_h =0), and this temperature drop continues till it reaches a minimum value at certain axial locations (see curves for 30°,60°,90°) after which it increases monotonically down the tube. This minimum value keeps changing its axial location as the cycle goes on. But the level of temperature keeps dropping after the minimum temperature axial location and can be easily seen from the Figure 8.11 at x/D_h =60. The displacement of the minimum T_a is dependent on value of A_r too. From Figure 8.12 which is for case H_2 (Va =88) this minimum value moves out of the tube as the cycle advances due to A_r being greater than

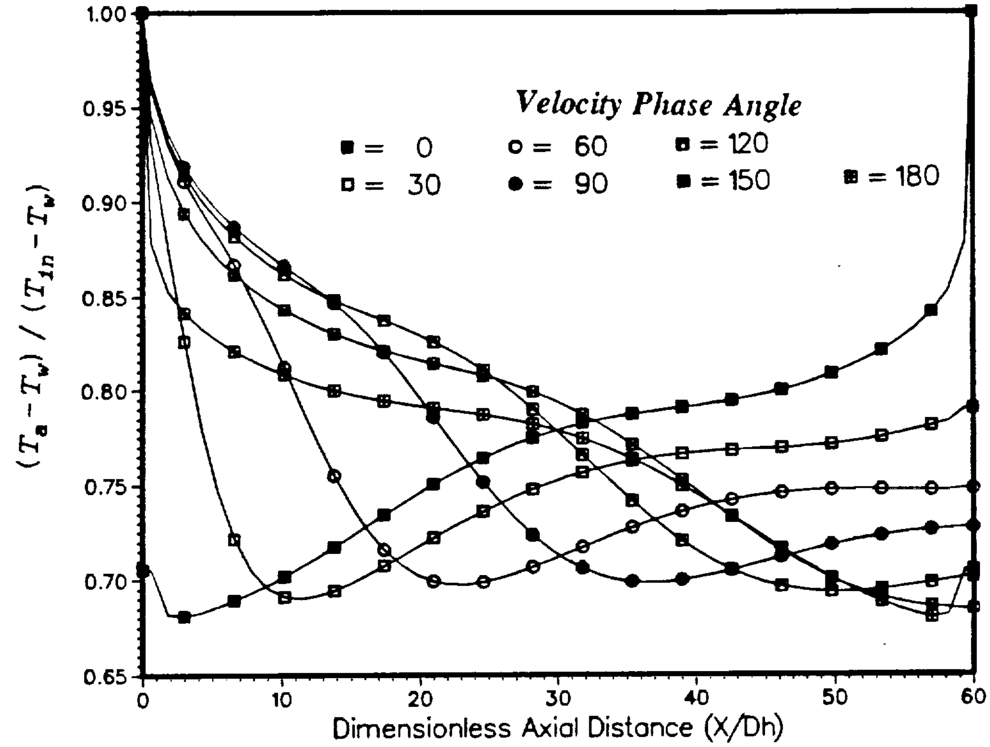

Figure 8.11. Normalized Section average temperature (T_a) versus the dimensionless axial distance (x/D_h) at different velocity phase angles. Case C_2 :: Re_{max}=30000, Va=350 and A_r=0.714.

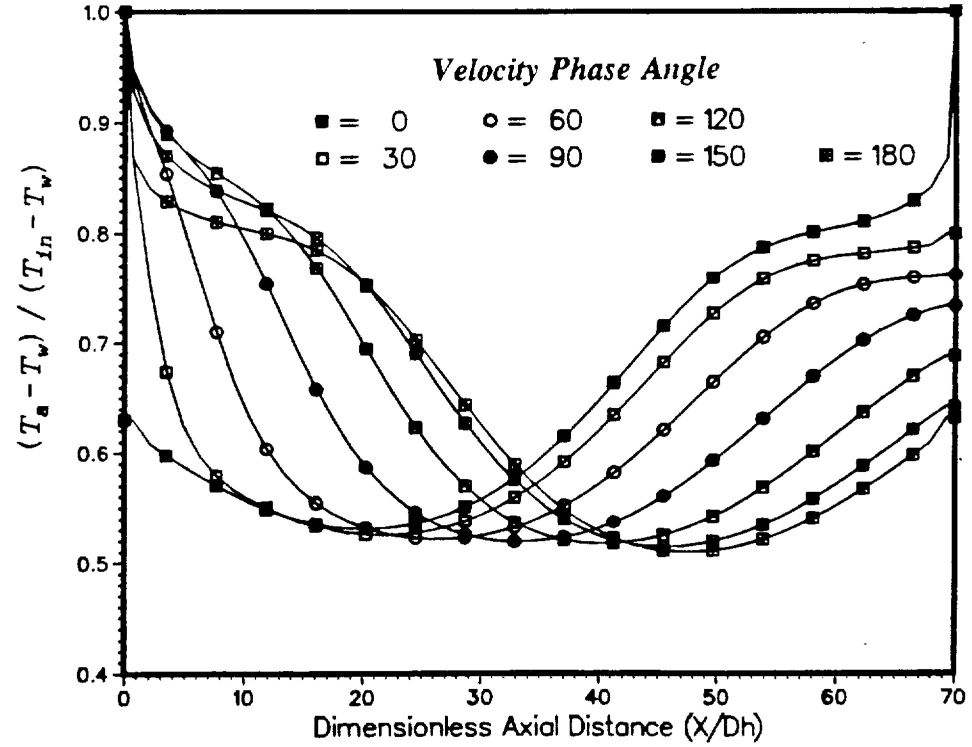

Figure 8.12. Normalized Section average temperature (T_a) versus the dimensionless axial distance (x/D_h) at different velocity phase angles. Case C_5 :: Re_{max}=20000, Va=400 and A_r=0.357.

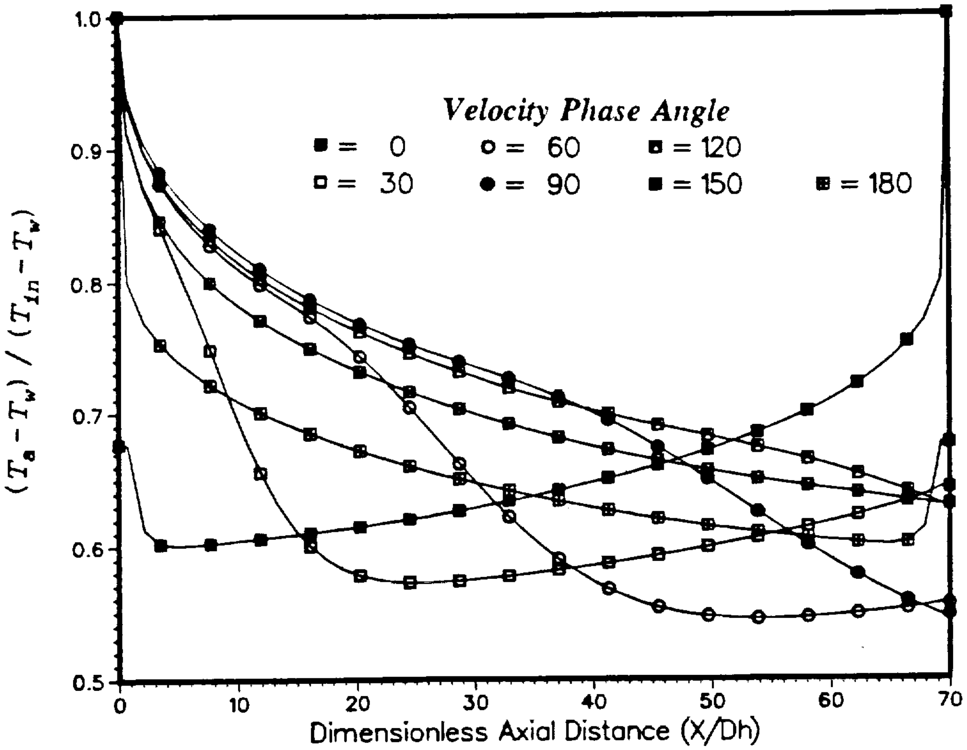

Figure 8.13. Normalized Section average temperature (T_a) versus the dimensionless axial distance (x/D_h) at different velocity phase angles.
Case H_2 :: Re_{max}=16500, Va= 88 and A_x=1.34.

one. The "minimum" temperature for the heater should actually be read as the maximum temperature as the normalized T_a is plotted instead of the true temperature. In the heater Case H_2 the basic heat transfer mechanism is the same as described above for case C_2 but the direction of heat transfer reversed since the function is to heat the fluid. The Valensi number (Va) effects the amplitude or temperature fluctuation at any given axial location with time. The heat transfer mechanism behaves similarly for the same A_r.

8.2.4 Bulk Temperature

The use of the bulk temperature is very prevalent in the design of heat exchangers. Also known as the mixing cup temperature it is a velocity weighted temperature defined as:

$$T_b = \frac{\int \rho UTdA}{\rho_m U_m A} \qquad (8.9)$$

Here ρ_m and U_m are the mean density and velocity respectively. The mean velocity is given by the mathematical expression:

$$U_m = \frac{\int UdA}{A} \qquad (8.10)$$

In oscillatory due to "backflow" or conuterflow at the walls at high Va this definition breaks down apart from the fact that the mean velocity goes to zero at 0°, 180° and 360° giving rise to unpysical values for the bulk temperature. Due to these discrepencies some researchers (Patankar and Oseid, 1992) have used the modulous of the velocity in Eq. (8.9) instead of the true velocity. With this change the Bulk temperature (T_b) definition is now given as:

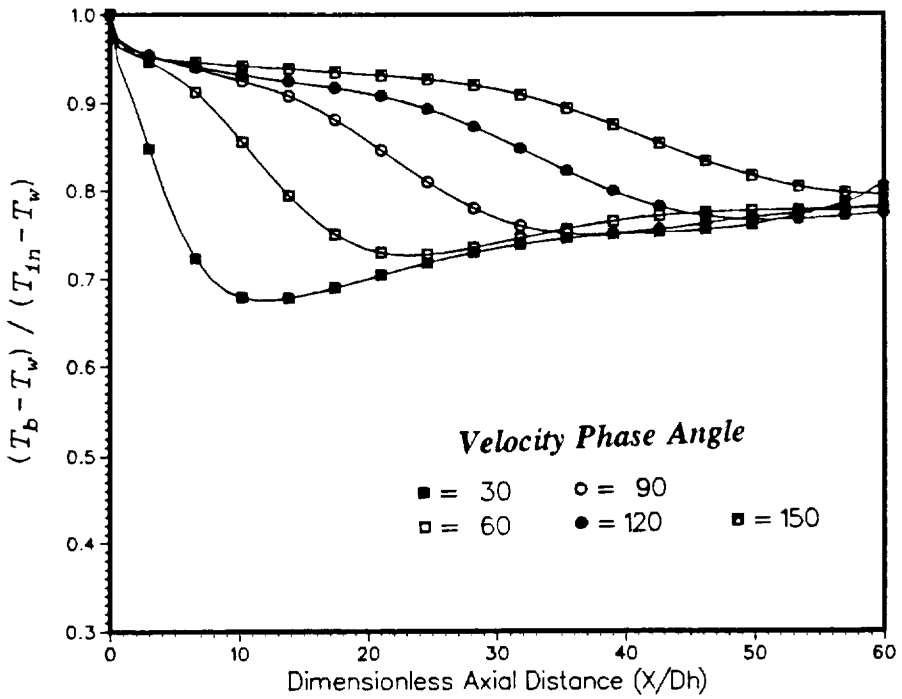

Figure 8.14. Normalized Bulk temperature (T_b) versus the dimensionless axial distance (x/D_h) at different velocity phase angles. Case C_2 :: Re_{max}=30000, Va=350 and A_r=0.714.

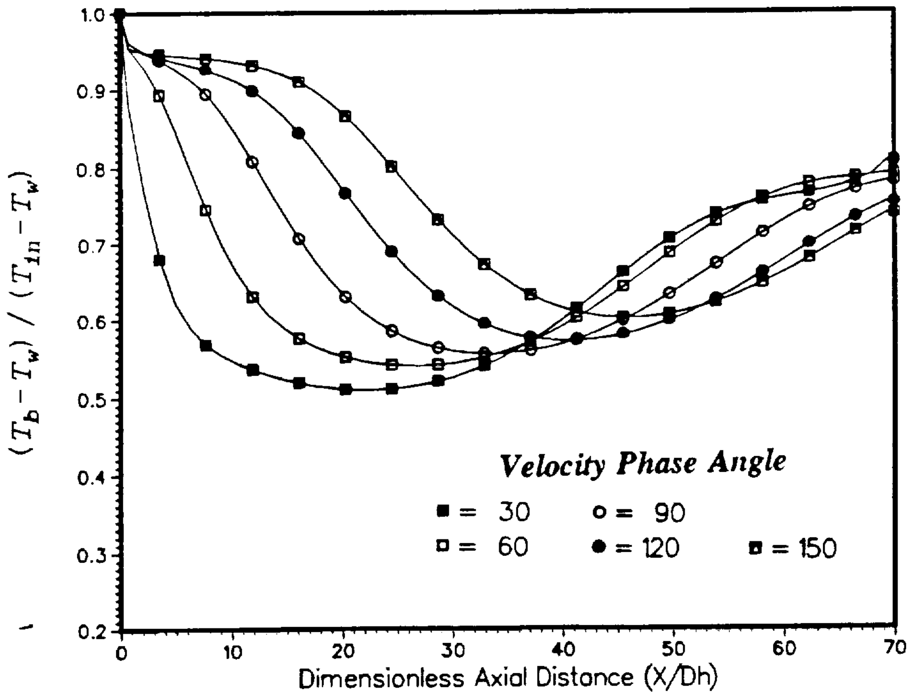

Figure 8.15. Normalized Bulk temperature (T_b) versus the dimensionless axial distance (x/D_h) at different velocity phase angles. Case C_5 :: Re_{max}=20000, Va=400 and A_r=0.357.

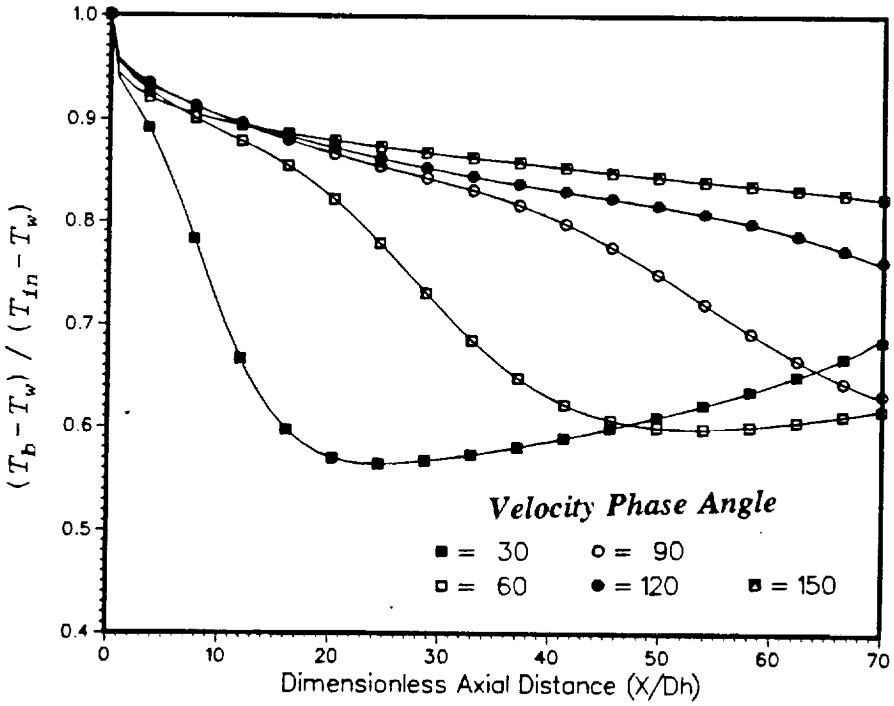

Figure 8.16. Normalized Bulk temperature (T_b) versus the dimensionless axial distance (x/D_h) at different velocity phase angles.
Case H_2 :: Re_{max}=16500, Va= 88 and A_r=1.34.

$$T_b = \frac{\int \rho |U| T dA}{\rho_m U_m A} \qquad (8.11)$$

Figures 8.14-8.16 plots the normalized bulk temperature profiles versus the dimensionless axial distance (x/D_h) at different velocity phase angles for the Cases C_2, C_5 and H_2 respectively. Once again the Cases were chosen such that they represent different A_r values as the effects and transfer mechanisms are similar for the same A_r value. The behaviour of the T_b is similar to the trend of T_a except for few differences. These differences can be observed by comparing Figures 8.13 and 8.16 which are for the same heater Case H_2, the amplitude of the bulk temperature (T_b) is different from the amplitude of section average temperature (T_a) fluctuation at any fixed axial location and even the magnitude of normalized value is different. This differences are of relatively minor consequence compared to the phase difference that arises between the T_b and the wall heat flux (q_w'') and which will be shown later in the chapter. The presence of a phase difference is due to the definition of T_b (Eq. 8.11) where the product of the local axial velocity (U) and temperature (T) is taken to evaluate T_b. And, when the Va is high there is phase difference between the velocity and temperature such that their inntegrated product over a cross-sectional area is different, i.e a situation where the T_b is zero can arise if U and T are 90° out of phase.

8.2.5 Wall heat Flux ($\dot{q}_w''$)

The wall heat flux ($\dot{q}_w''$) is the parameter which governs the effectiveness of ay heat exchanger. Figures 8.17-8.19 plots the $\dot{q}_w''$ normalized with the maximum inlet enthalpy ($\rho U_{\max} C_p T_{in}$) versus x/D_h at different velocity phase angles for the three Cases C_2, C_5 and H_2 representing different A_r's. The negative wall heat flux values indicates that the direction of heat transfer is from the fluid to the wall, i.e the fluid gets cooled. The general trend is the wall heat flux increases along the length of the tube at instant of the cycle and then increases to a maximum or minimum value (depending upon whether it's a cooler or heater case) along the length of the tube and then starts to decrease or increase for the rest of the channel length.

Since the wall heat flux is an important design parameter an attempt has been made to correlate the $\dot{q}_w''$ as a function of A_r, $Re_{\max}$, Va, and x/D_h for all the test cases investigated. The correlation process consisted of two important steps:

- In the first the advantage of symmetric inflow conditions was taken. That is, the correlation effort was concentrated for only half oscillation cycle.
- The second step involved Fourier analyzing the data for one half oscillation cycle (0° to 180°) and then correlate the resulting harmonics.

The correlations were done using curve fitting software and was sufficiently tuned to handle multiple curve such as arising in oscillatory flows. The correlation arrived at has the form:

A look at the above correlation reveals that $\dot{q}_w''$ consists of a mean value ($\dot{q}_m''$)

$$\frac{\dot{q}_w''}{\dot{q}_n''} = \dot{q}_m'' + \dot{q}_2'' \cdot Sin(2\omega t + \Phi_2) \qquad (8.12)$$

and an even harmonic component. $\dot{q}_2''$ is the amplitude of the harmonic component and Φ_2 phase difference relative to the mean or inflow velocity and $\dot{q}_n''$ is a heat flux normalization factor used. As it can be seen the variation of wall heat flux is mathematically and literally complex in oscilatory flows. All the coefficients are functions of all the nondimensional parameters and are mathematically found to be:

$$\dot{q}_n'' = \frac{\sqrt{Va} \cdot Re_{max}{}^{0.1}}{0.312 - 0.1 \cdot A_r^3} \; \{ 1 + 5.5\times10^{-5} \cdot e^{-4A_r} \cdot (0.5 - A_r) \cdot (x/D_h)^2$$

$$+ \; [0.84 + (1.051/\sqrt{A_r})] \cdot (A_r - 0.5) \cdot (1 - A_r) \sqrt{x/D_h} \qquad (8.13)$$

$$+ \; [0.21 + 0.1437 \cdot \ln(A_r)] \cdot (x/D_h)^{-1.5} \}$$

The mean wall heat flux ($\dot{q}_m''$) takes the following form:

$$\dot{q}_m'' = (1.16) \cdot \left[-1 + 0.15 \cdot (x/D_h) + 7.5 \sqrt{x/D_h} \right] \qquad (8.14)$$

and the other coefficients are:

$$\dot{q}_2'' = -0.2 + 3.0\times10^{-31} \cdot e^{-(x/D_h)} + [1/(0.26 + 0.073A_r)] \cdot (x/D_h)^{-0.5} \qquad (8.15)$$

$$\Phi_2 = 262.4 - 24.86 \cdot [\ln(A_r)]^2 - e^{[-1.854 - 2.6 \cdot A_r^2 \cdot \ln(A_r)]} \cdot (x/D_h)^2 \cdot$$

$$\{ 1 + e^{[-4.756 - 2.4 \cdot A_r^2 \ln(A_r)]} \cdot (x/D_h) \} \qquad (8.16)$$

The above equation is valid for the first half oscillation cycle (0° to 180°) for the

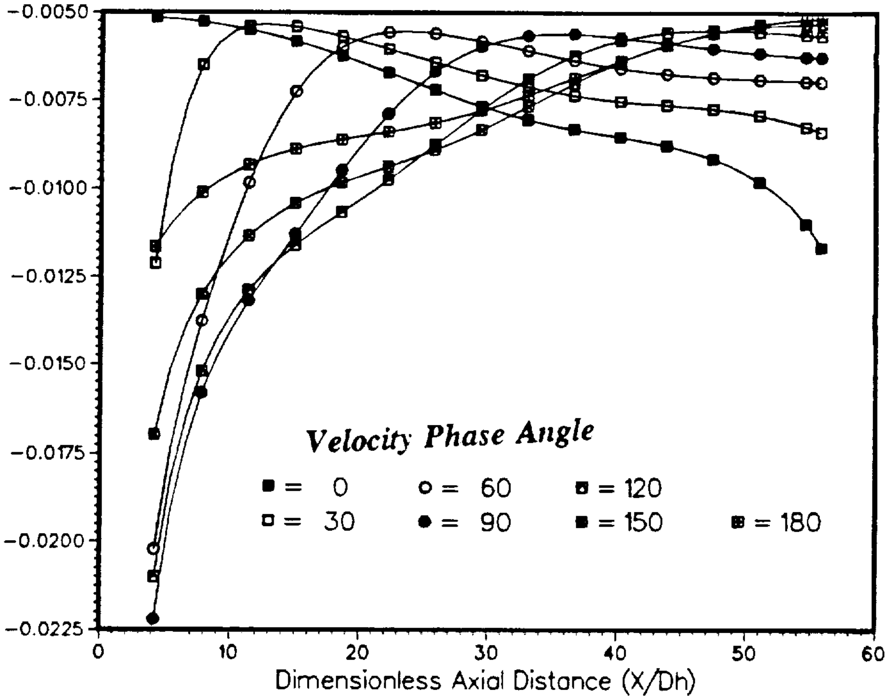

Figure 8.17. Normalized Wall heat flux ($\dot{q}_w''$) versus the dimensionless axial distance (x/D_h) at different velocity phase angles. Case C_2 :: Re_{max}= 30000, Va= 350 and A_r= 0.714.

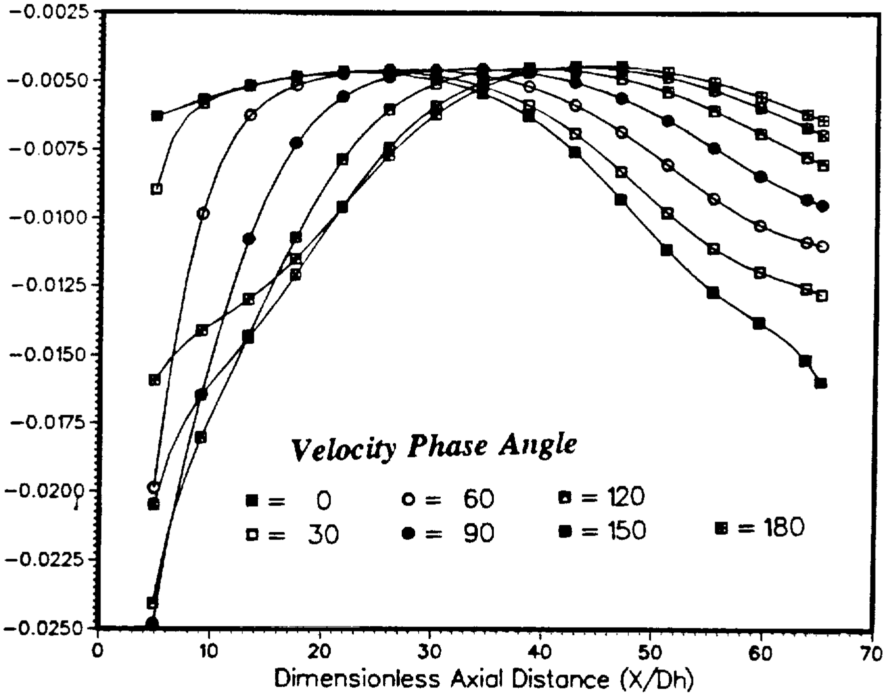

Figure 8.18. Normalized Wall heat flux ($\dot{q}_w''$) versus the dimensionless axial distance (x/D_h) at different velocity phase angles. Case C_5 :: Re_{max}= 20000, Va= 400 and A_r= 0.357.

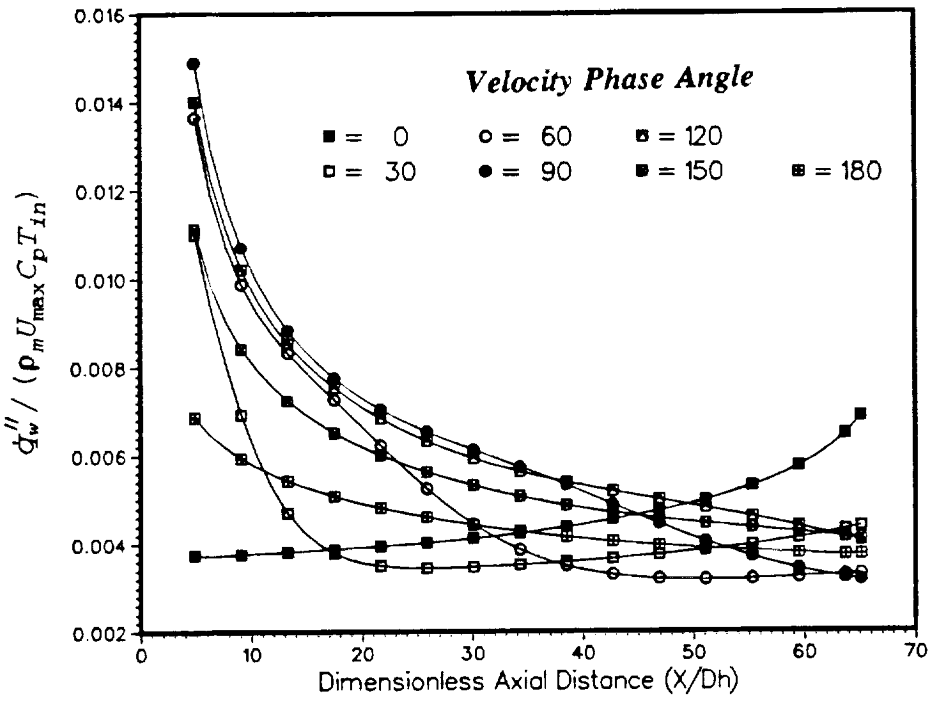

Figure 8.19. Normalized Wall heat flux ($\dot{q}_w''$) versus the dimensionless axial distance (x/D_h) at different velocity phase angles. Case H_2 :: Re_{max}= 16500, Va= 88 and A_x= 1.34.

second half oscillation period the same equation is to be used but with x/D_h being replaced by [L - x/D_h] in all the above equations.

It can be seen that the correlation coefficients take a very complicated functions of A_r and x/D_h . The above equation was used to validate the numerically calculated wall heat fluxes $\dot{q}_w''$. Figures 8.20-8.22 shows plots the ratio of numerical wall heat flux to the wall heat flux calculated using the correlation (Eq. 8.12) at select velocity phase angles for the cases C_2, C_5 and H_2. From the figures it can be concluded that the that the correlation predicts the numerical $\dot{q}_w''$ within 10% for the three cases for the velocity phase angles shown. The prediction is especially good near the centre of the pipe, the relatively poor prediction for low A_r values (see Fig. 8.23) has been caused by optimizing trying to optimize the correlation for higher A_r values (Cases C_2 and H_2).

8.2.6 Heat Transfer Coefficient

The heat transfer coefficient is usually represented by the Nusselt's number (Nu) which is defined as:

$$Nu = \frac{[\dot{q}_w''] \cdot D_h}{[\Delta T]\, k} \tag{8.17}$$

Here the ΔT is the reference temperature difference can be based either on section average temperature (T_a) or the bulk temperature (T_b) that is ΔT=[T_w - T_a] or [T_w - T_b].

Since the heat transfer coefficient is the variable used in most heat exchanger design, care should be taken as to how it is defined. As mentioned earlier the T_a and

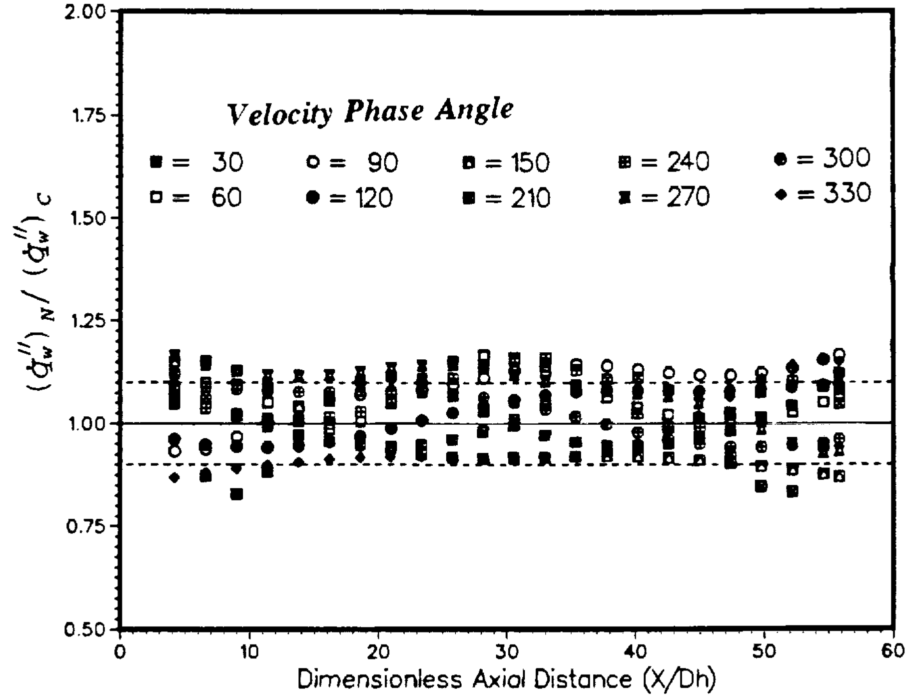

Figure 8.20. Ratio of Numerical Wall heat flux to the correlated wall heat flux versus the dimensionless axial distance (x/D_h) at different velocity phase angles.
Case C_2 :: Re_{max} = 30000, Va = 350 and A_r = 0.714.

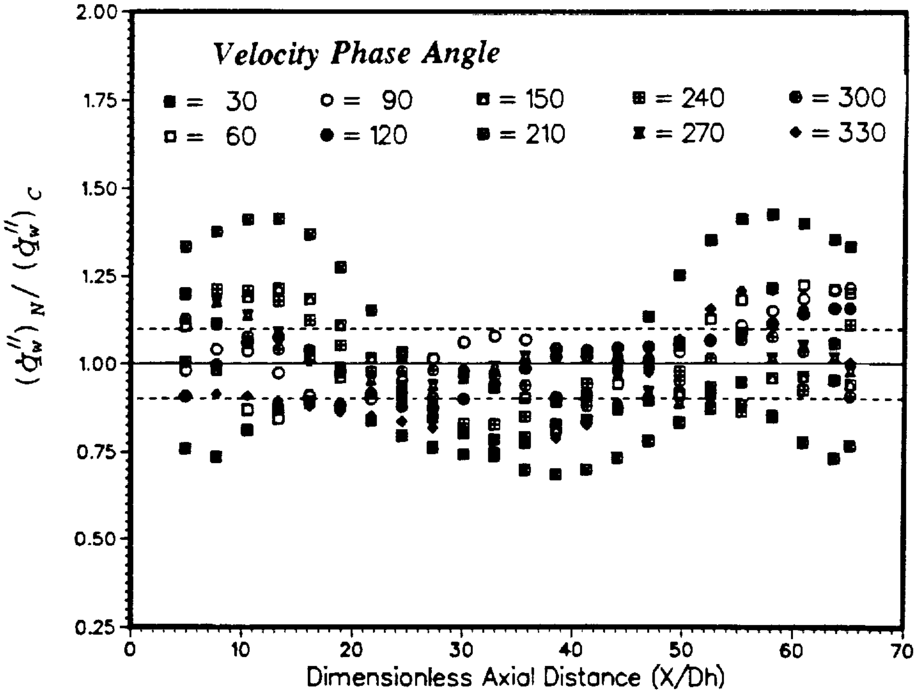

Figure 8.21. Ratio of Numerical Wall heat flux to the correlated wall heat flux versus the dimensionless axial distance (x/D_h) at different velocity phase angles.
Case C_5 :: Re_{max} = 20000, Va = 400 and A_r = 0.357.

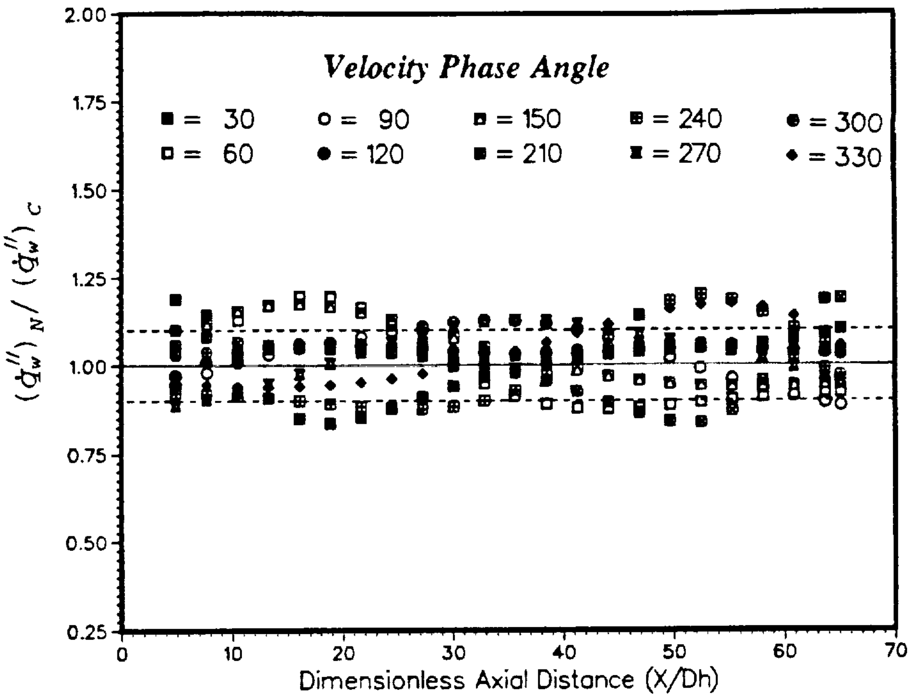

Figure 8.22. Ratio of Numerical Wall heat flux to the correlated wall heat flux versus the dimensionless axial distance (x/D_h) at different velocity phase angles.
Case H_2 :: Re_{max}= 16500, Va= 88 and A_r= 1.34.

T_b behave very different from each other in oscillatory flows thus making it very ambiguous as to how the temperature difference should be taken to evaluate the heat tansfer coefficient. This fact is demonstrated by the Figures 8.24a and 8.24b, in the former figure the Nusselt's number based on T_a while in the latter it is based on T_b for the Case C_2. When the section average temperature (T_a) is used the the wall heat flux, Nusselt's number and T_a are all in phase with each other. Whereas when T_b (Bulk temperature) is used they are all out of phase with each other (see Fig. 8.24b). Moreever, when T_b is used the Nusselt's number shoots to infinity at flow reversal points (0°, 180° and 360°). It should be noted that the two plots show symmetry in time i.e. the thermal cycle is repeated twice for one flow cycle, this due to the inflow temperature symmetry and the plots are made at the channel mid-plane.

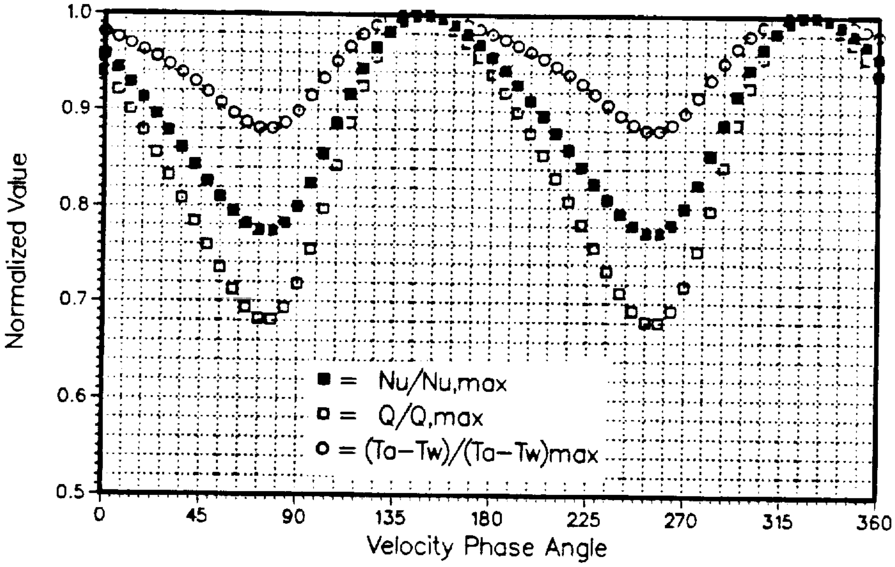

Figure 8.23a. Normalized values for Nusselt's number (*Nu*), Wall heat flux ($\dot{q}_w''$) and Temperature Difference ($\Delta T = T_a - T_w$) based on the *section average* temperature.

Case C_2 :: Re_{max} = 30000, Va = 350 and A_r = 0.714.

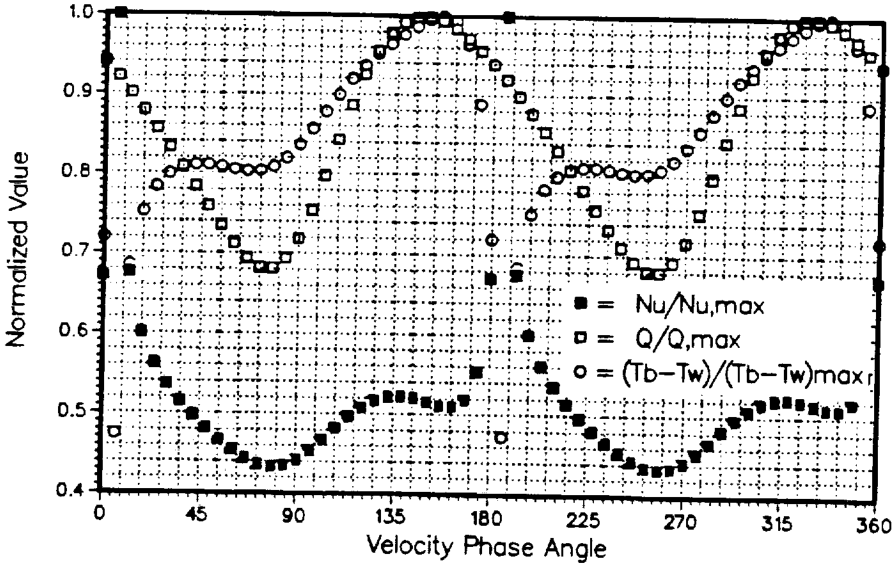

Figure 8.23b. Normalized values for Nusselt's number (*Nu*), Wall heat flux ($\dot{q}_w''$) and Temperature Difference ($\Delta T = T_b - T_w$) based on the *bulk* temperature.

Case C_2 :: Re_{max} = 30000, Va = 350 and A_r = 0.714.

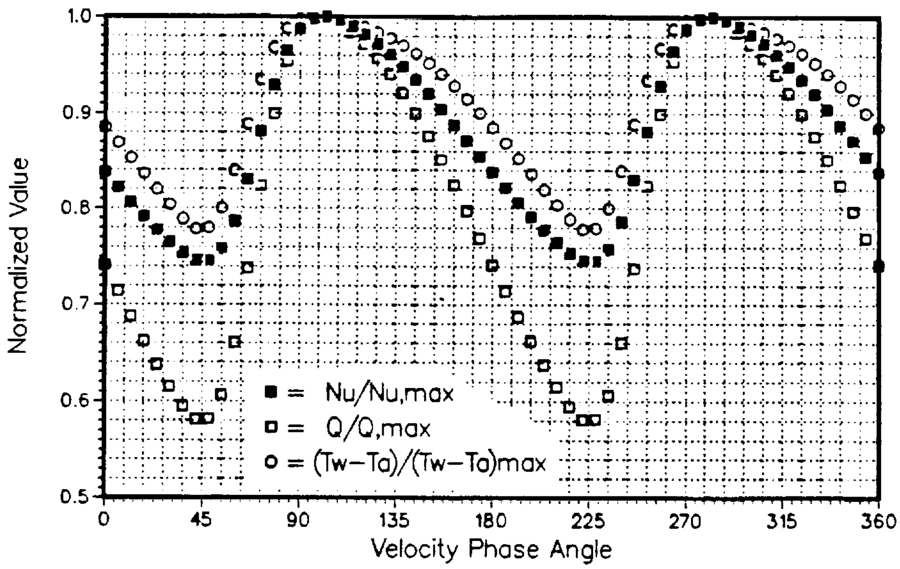

Figure 8.24a. Normalized values for Nusselt's number (Nu), Wall heat flux ($\dot{q}_w''$) and Temperature Difference ($\Delta T = T_a - T_w$) based on the *section average* temperature.
Case H_2 :: $Re_{max} = 16500$, $Va = 88$ and $A_r = 1.34$.

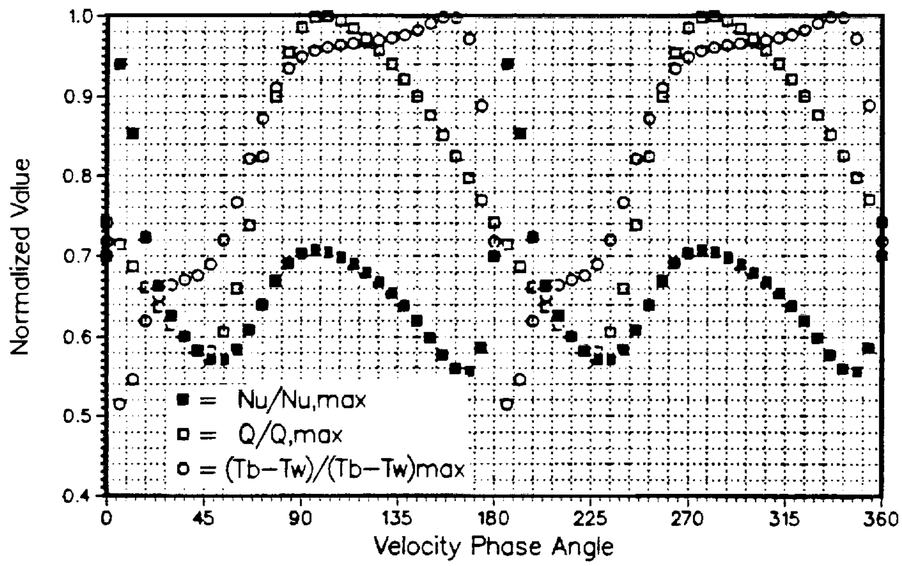

Figure 8.24b. Normalized values for Nusselt's number (Nu), Wall heat flux ($\dot{q}_w''$) and Temperature Difference ($\Delta T = T_b - T_w$) based on the *bulk* temperature.
Case H_2 :: $Re_{max} = 16500$, $Va = 88$ and $A_r = 1.34$.

8.3 Asymmetric Temperature Inflow

In this situation the flow enters the tube with a different temperature from one-half cycle to the other. In the Stirling engine heat exchangers this is the type of temperature boundary condition one encounters due to the fact the heat exchangers are arranged connected together. Table 8.3 list the cases investigated under the heater and cooler conditions as can be seen these are similar to the symmetric temperature inflow condition cases except for the inlet temperatures.

The asymmetric temperature inflow heat transfer situation is complicated by the presence of an additional driving potential or the presence of axial heat conduction. Figure 8.25 shows an schematic representation of the cooler with asymmetric inflow temperature boundary conditions. In the first period (0° to 180°) the hot fluid (T_h) enters from the left end of the tube and the second half period (180° to 360°) it enters with a colder temperature (T_c) from the right end, with the wall being maintained at a colder temperature (T_w) than the either of the inflow temperature (i.e. $T_w < T_c < T_h$). The heat transfer mechanism has two driving temperature potentials, ($T_c - T_w$) and ($T_h - T_c$) and depending upon which driving potential is greater the heat transfer mechanism is accordingly effected. In the present study, both ($T_c - T_w$) > ($T_h - T_c$) and ($T_c - T_w$) < ($T_h - T_c$) have been investigated, from Table 8.3 it can be seen that the former condition exists for the heater Cases HA_1, HA_2 and HA_3 and the latter for the cooler Cases CA_1, CA_2 and CA_3. The presence of axial driving potential plays a very important role especially in oscillatory flows where the axial heat transport is greatly augmented (See Kurzweg, 1985a) due to flow oscillation. And if the flow is

Table 8.3: Test cases investigated for asymmetric temperature inflow.

TEST CASE	$Re_{\max}$	Va	L/D_l	T_{wall}	T_{west}	T_{east}	A_r
CA_1	15000	175	60	325	350	330	0.714
CA_2	30000	350	60	325	350	330	0.714
CA_3	60000	700	60	325	350	330	0.714
HA_1	8250	44	70	650	630	610	1.340
HA_2	16500	88	70	650	630	610	1.340
HA_3	33500	176	70	650	630	610	1.340

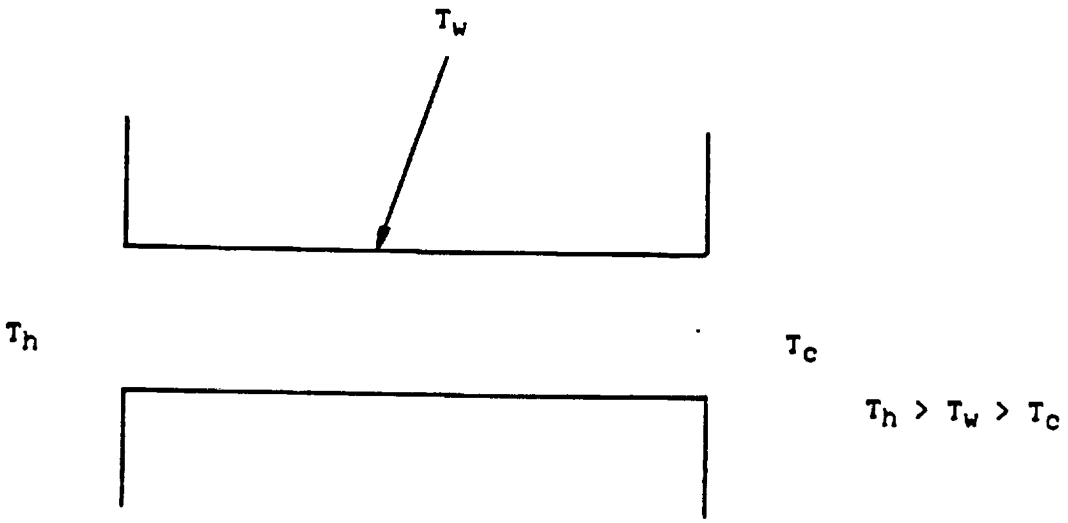

Figure 8.25. Asymmetrical temperature inflow boundary conditions representation for the heater.

at a high Va, additional complications can arise due to the backflow at the wall thus generating a additional temperature potential between the Stoke's layer and the central core of the fluid.

Keeping the above observations in mind the temperature profiles for two representative Cases are discussed next.

8.3.1 Temperature Profiles

Figures 8.26 (a),(b) and 8.27 (a),(b) shows the 3D temperature profiles for the Cases CA$_2$ ($Re_{\max}$ =30000, Va = 350, A_r =0.714, T_{west} = 350 °K, T_{east} = 330 °K) and HA$_2$ ($Re_{\max}$ =16500, Va = 88, A_r =1.340, T_{west} = 630 °K, T_{east} = 610 °K) at different velocity phase angles. In the discussion to be presented next the inflow temperature from the west (left) end of the tube T_{west} will be referred as T_h (Hot end) and the inflow temperature from the east (right) end of the tube T_{east} will be referred to as T_c (Cold end). Since the inflow is asymmetric with time the profiles are shown for the complete cycle.

Figure 8.26 (a),(b) shows the 3D temperature profile plots for Case CA$_2$ (Va = 350) in the whole tube for every 30° increment of the oscillation cycle (30°,60°,90°,..., 360°). In the first half cycle (0° to 180°) [Fig. 8.26a] hot fluid with temperature T_h = 350 °K enters from the west end of the tube and in the next half cycle (180° to 360°) [Fig. 8.26b] the flow enters from the east end with a lower temperature T_c = 330 °K with the wall being maintained at the lowest temperature T_w = 325 °K. At the beginning of the cycle the flow enters from the hot end with T_h (350 °K) with most of

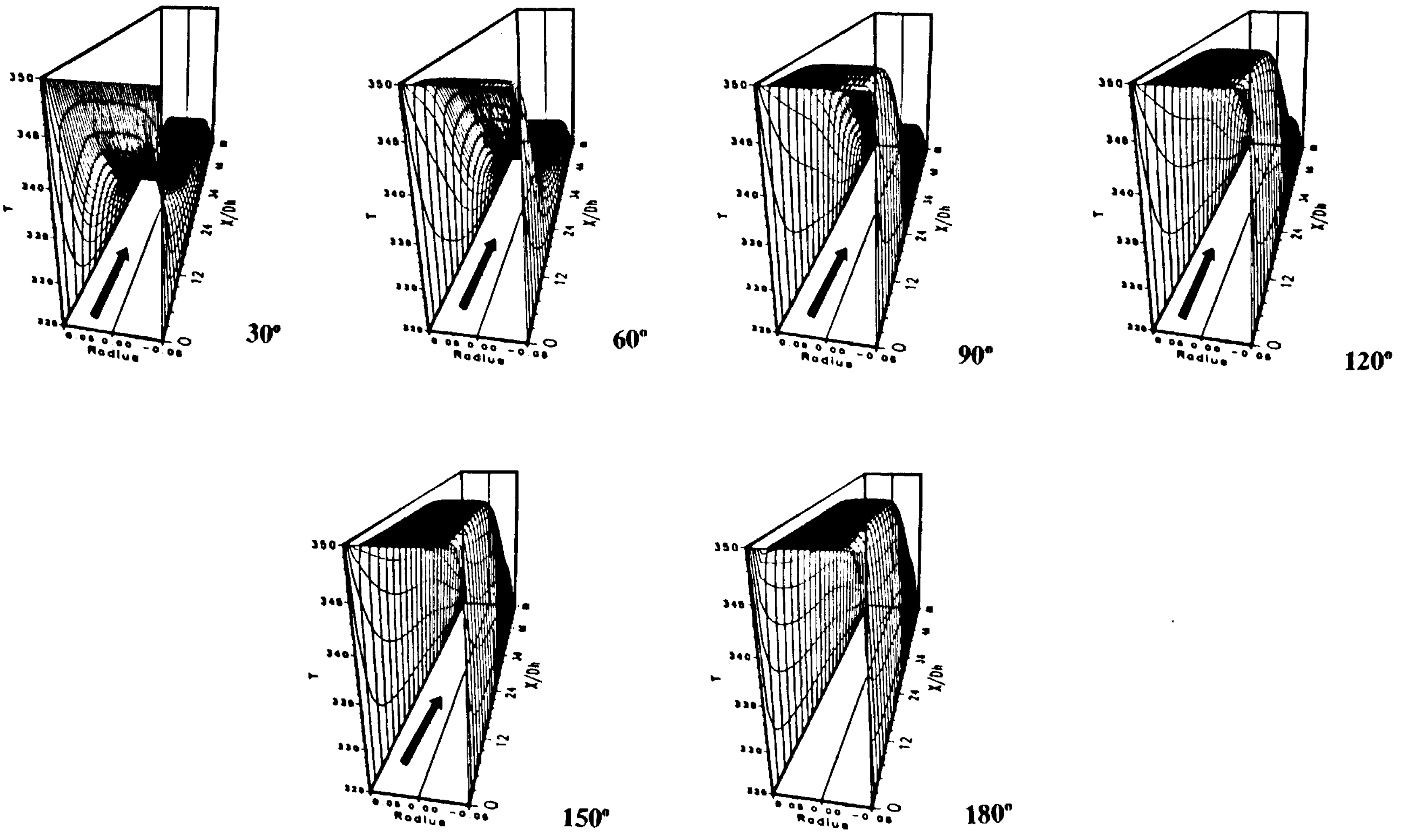

Figure 8.26a. Three-Dimensional Temperature plots at different velocity phase angles for asymmetric temperature inflow problem.
Case C_2 :: Re_{max}= 30000, Va= 350, A_r= 0.714, T_h =350 °K and T_c =330 °K.

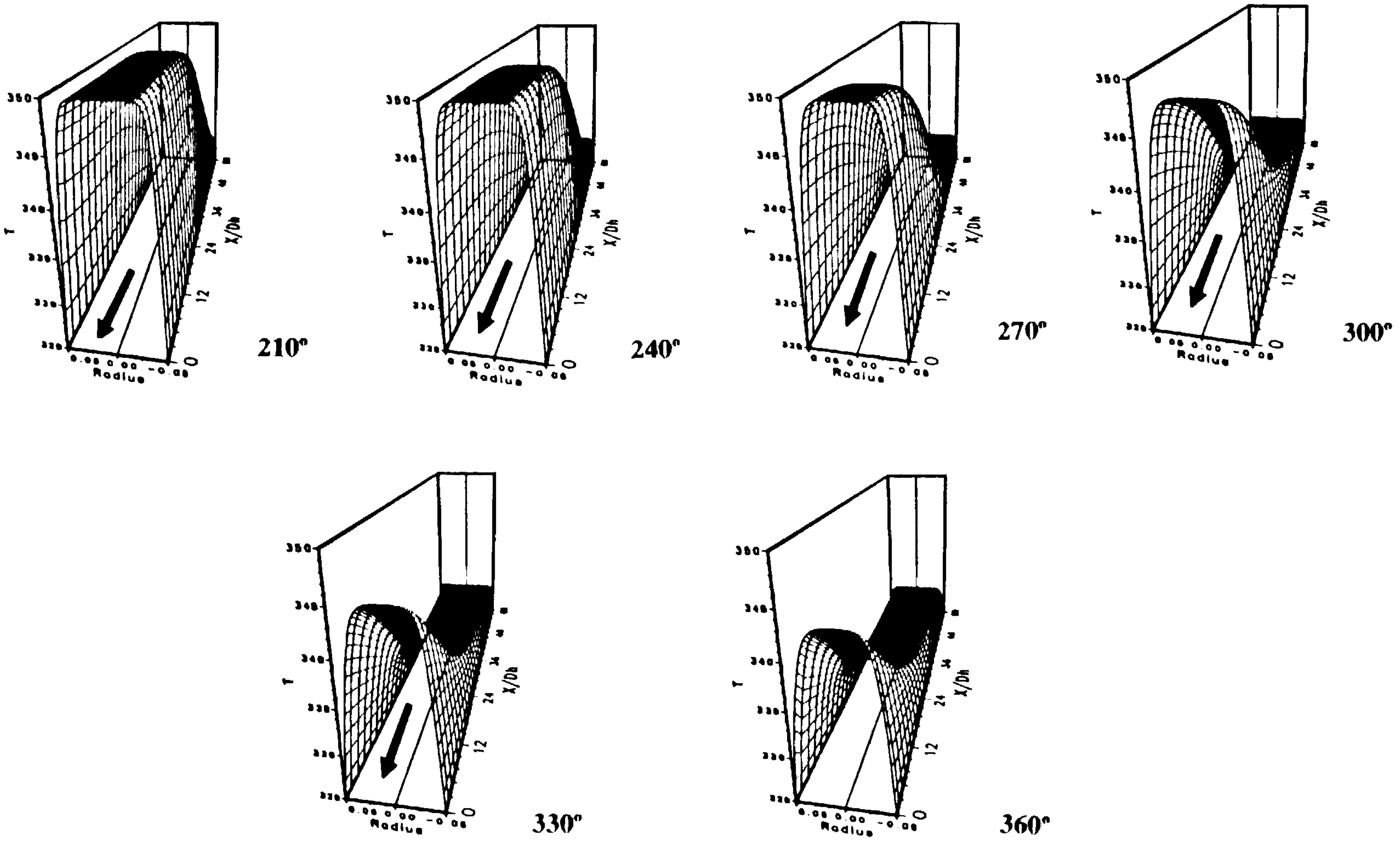

210°

240°

270°

300°

330°

360°

Figure 8.26b. Three-Dimensional Temperature plots at different velocity phase angles for asymmetric temperature inflow problem.[contd.]
Case C_2 :: Re_{max}= 30000, Va= 350, A_r= 0.714, T_h =350 °K and T_c =330 °K.

the tube at a colder temperature due to the temperature history of the previous cycle. When the cycle begins most of the fluid in the tube is at a colder temperature T_c (330 °K) due to the temperature history effect of the previous cycle. Then the hot thermal front advances into the tube from the west end of the tube (x/D_h =0) as the cycle proceeds (60°) pushing the cold thermal front out of the tube (x/D_h =60), just like in the symmetric inflow situation. But due to the presence of the driving potential (T_h - T_c) the hot thermal front does not appear till late in the accelerating phase (60°). The effect of high Va can be seen by the presence of thick hot central core and due to (T_c - T_w) < (T_h - T_c), the temperature of the thick central core never falls below T_c (330 °K) in the whole cycle despite the presence of a much colder wall (T_w = 325 °K). Further the effect of this driving potential can be seen forward of the hot thermal front where the temperature of the core drops almost quasi-linearly to the temperature of the cold front (see Fig. 8.26a at 60°,90°). As the hot thermal front advances into the tube in time the fluid ahead of it (near x/D_h =60) gets cooled by the colder wall but due to the weaker driving potential (T_c - T_w) the temperature does not fall below T_c. When the flow reverses (after 180° velocity phase angle) and starts from the right end of the tube (x/D_h =60) most of the fluid in the tube is now at the hotter temperature T_h (350 °K). Also the driving potential (T_h - T_c) now acts in a direction opposite to the flow direction, thereby the hot fluid present near the left end of the tube (x/D_h =0) cools rapidly as the second half cycle proceeds (210° to 360°). Hence it aids the cooling process done by the colder wall temperature.

Figures 8.27a and 8.27b shows the 3D temperature profiles for Case HA2,$Re_{\max}$

=16500, Va = 88, A_r =1.340, T_{west} = 630 °K, T_{east} = 610 °K and T_w = 650 °K. In this case the longitudinal temperature driving potential (T_w - T_c) is greater than the axial temperature driving potential (T_h - T_c). Hence the heat transport from the wall dominates over the axial heat transport. In the first half of the cycle (0° to 180°) the flow enters from the west or "hot" end with T_h = 630 °K and the next half cycle (180° to 360°) the flow reverses and enters from the east or "cold" end. Figure 8.27a shows the temperature profiles for the first half cycle, as can be seen the effect of the advancing thermal front appears quickly at around 60° velocity phase angle. Prior to that the flow within the tube is cooler than the incoming fluid due to the temperature history of colder fluid entering from the "cold" end (see Fig. 8.27b at 360°). Because of high A_r the front starting from x/D_h =0 advances into the tube and continues to advance as the cycle proceeds. Since the flow is in the same direction as the axial driving potential (T_h - the whole tube gets heated up to more than the incoming fluid temperature at the end of the half cycle (180°). When the flow reverses (180° to 360°) thereby opposing this axial temperature driving potential the heating process is not as effective as for the previous half cycle (see Figure 8.27b) despite a high longitudinal temperature driving potential. Therefore at 360° one can observe that the flow actually "cools" at the exit (in this situation x/D_h =0) rather than increase in the temperature.

Hence it can be concluded that the axial temperature driving potential plays a crucial role in the effectiveness of the heat exchanger during the whole complete cycle.

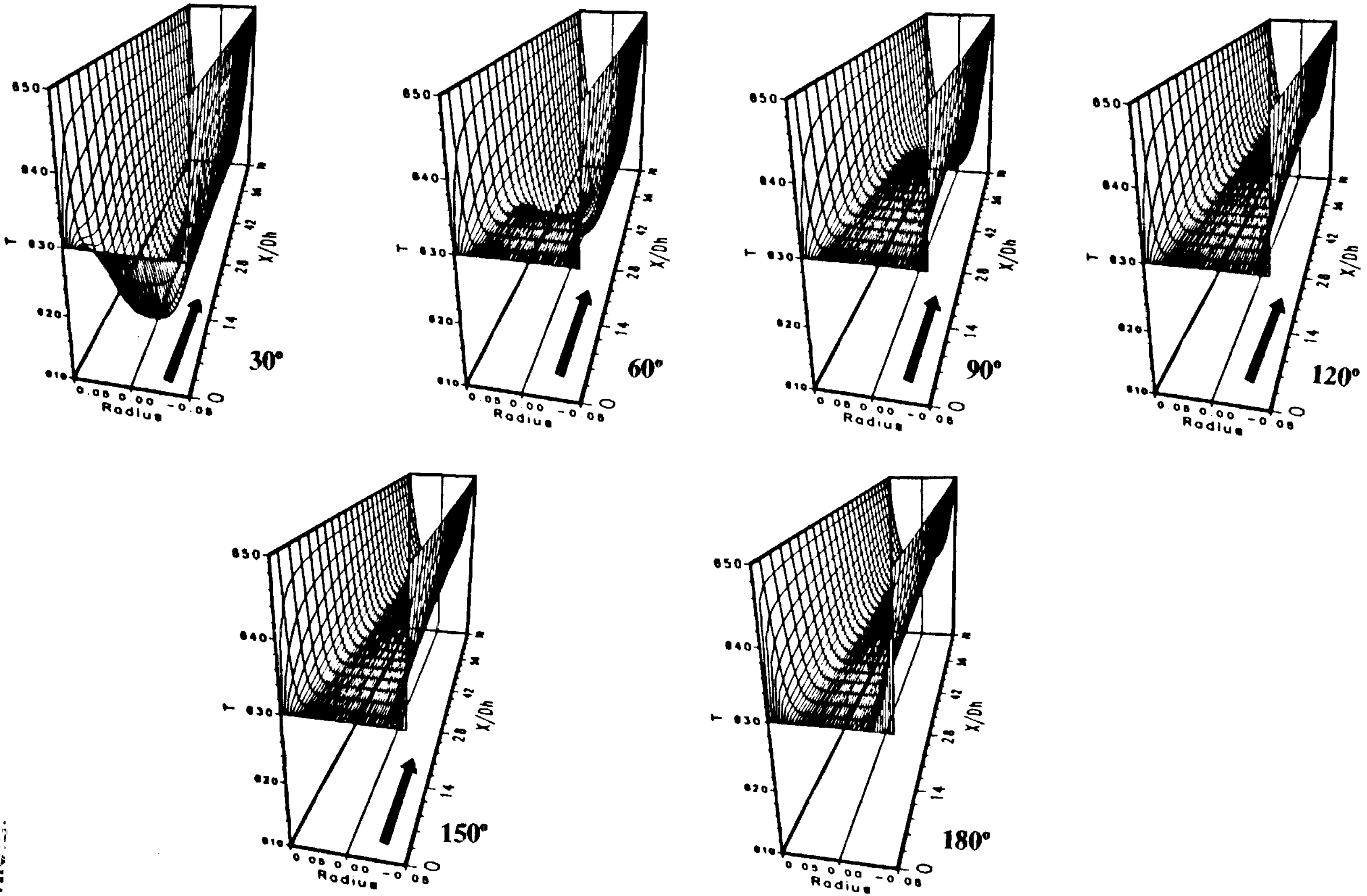

Figure 8.27a. Three-Dimensional Temperature plots at different velocity phase angles for asymmetric temperature inflow problem. Case H_2 :: Re_{max}= 16500, Va= 88, A_r= 1.34, T_h =630 °K and T_c =610 °K.

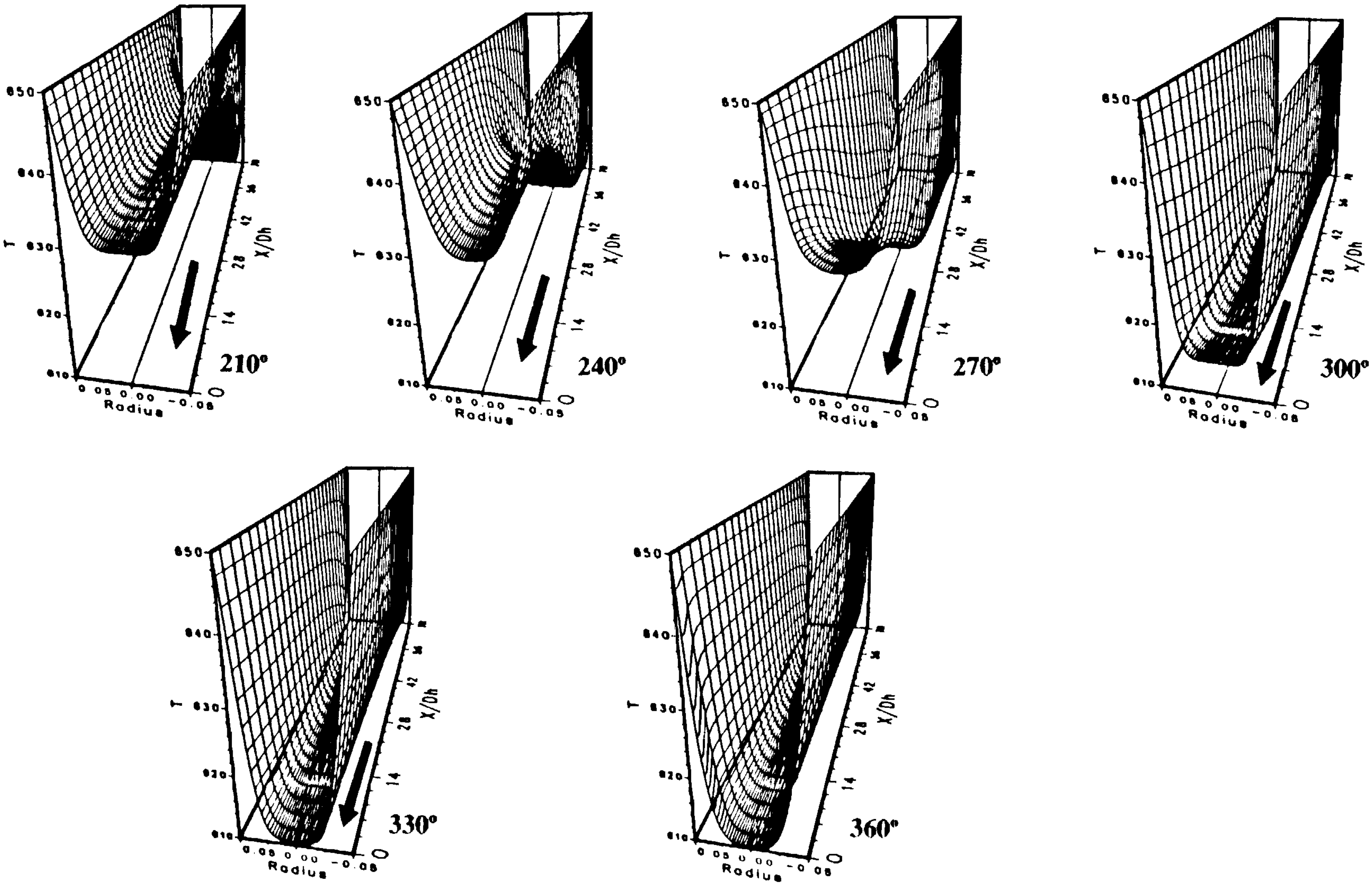

Figure 8.27b. Three-Dimensional Temperature plots at different velocity phase angles for asymmetric temperature inflow problem.[contd.]
Case H_2 :: Re_{max}= 16500, Va= 88, A_r= 1.34, T_h =630 °K and T_c =610 °K.

CHAPTER IX

CONCLUSIONS

A summary of the computational results for the flow and thermal analysis in three different components of the Stirling engine, namely, Regenerator, Cooler and Heater are presented next. The cases investigated are summarized in Table 6.1 and they represent the operating conditions of NASA Space Power Research Engine in terms of $Re_{\max}$, Va, L/D_h, and A_r. In actual engine operating conditions, all the cases examined (except for Case R_1) should go through the laminar/transition/turbulent flow regimes throughout the cycle. This study was focussed on the effects of oscillatory flow under laminar flow conditions with constant thermophysical properties.

Cases R_1 and R_2 resemble the Regenerator and have been modeled using the conjugate heat transfer problem with a two-parallel-plates channel. Cases C_1, C_2 and C_3 as well as H_1, H_2 and H_3 are modeled using the circular pipe geometry with isothermal wall, resembling the Cooler and Heater respectively.

The conclusions from the computations are as follows:

- The fluid flow and heat transfer for regenerator (Case R_1) are quasi-steady i.e. the velocity and temperature profiles are parabolic and in phase. For high Va (Case R_2) "backflow" or flow reversal takes place near the wall during the decelerating portions of the cycle resulting in flat temperature and velocity profiles in the core of the channel. In these situation the viscous effects are restricted to a small region next to the wall and is known as the Stoke's layer.
- The Cases R_1 and R_2 were not only used to study the foil type regenerator but also to validate the numerical code by comparing the computational results with the analytical solution under similar operating conditions. The comparison was not trivial because the analytical work was based on oscillatory pressure boundary condition for an infinite channel, while the computational work was done for a finite channel with sinusoidally varying velocity boundary condition. The numerical results compared very well with the reformulated analytical results.
- For oscillatory flows in parallel-plates-channel the wall shear stress (τ_w) and pressure drop (Δp) are augmented by almost factors of 5 and 80 respectively, as the Va increases. Also they are out of phase with the velocity by 45° and 90° as the Va increases.
- The instantaneous entrance length is controlled by the A_r value. For high A_r

values (H_1-H_3 & C_1-C_3) it is difficult to define a fully developed flow conditions as the instantaneous friction factor does not settle with the axial distance. But in general the entrance effects are restricted to a small region into the channel.

- The heat transfer results show for the cooler and heater with symmetric temperature inflow conditions show that the heat transfer coefficient (at the channel mid-plane) goes through two cycles per each flow cycle. Also, at high V_a the temperature profile is out of phase with the velocity profile.
- The heat transfer mechanism are controlled by the temperature "history" effects which reveals itself by the presence of "hot" and "cold" spots during the cycle.
- The usual definition of the heat transfer coefficient in the case of oscillatory flows is ambiguous and limited due to the way the temperature difference is determined. The common practice of using the bulk or mixing cup temperature (T_b) as the reference for evaluating the temperature difference breaks down due to the flow reversal close to the wall during parts of the cycle for high V_a, especially for laminar flows. This ambiguity was resolved in the study by using the absolute value of the velocity in the definition of bulk temperature and then evaluate the heat transfer coefficient.
- Using the section average temperature (T_a) as the reference temperature for the temperature difference, the wall heat flux, temperature difference,

and the Nusslet's number are all in phase with each other and out of phase with the velocity. The above quantities are all symmetric about 180° at the channel axial mid-plane otherwise the shape is different from the first half cycle to the second half cycle.

- Using the bulk temperature as the reference temperature the wall heat flux and the temperature difference are out of phase with each other (accordingly Nusselt's number) and with the velocity. Also, the temperature difference passes through zero and accordingly, the Nusselt number shoots to infinity.
- The asymmetric inflow temperature conditions has a drastic effect on the heat transfer mechanism. The two temperature driving potential (one axial and the other longitudinal) control the direction of the heat transfer mechanism.

9.1 Scope for Further Research

The primary objective of this research was to investigate the thermal field in a two dimensional simulation of the Stirling engine heat exchangers. The analysis presented in this study was done independently for each of the Stirling engine. The present study can be augmented by:

- Connecting the components together, i.e., the regenerator, cooler and heater in one direct two dimensional simulation to better understand the effects of oscillating flow in each component.

- adding compressibility effects by introducing the two pistons found in the engine and thus facilitate a complete two dimensional engine simulation.
- introducing empirical turbulence model into the code to simulate the transition from laminar to turbulent flow and thus improve the predictions for engine losses.

BIBLIOGRAPHY

Ahn, K.H. and Ibrahim, M.B. (1992): "Laminar/Turbulent Oscillating Flow in Circular Pipes", Int. J. Heat and Fluid Flow, Vol. 13, No. 4, pp. 340-346, December 1992.

Devalba, M. and Rispoli, F. (1991): "The Oscillating Fluid Flow Effects on the Stirling Engine Heat Exchanger Design", 5th International Stirling Engine Conference, 8-10 May, 1991. Dubrovnik, Yugoslavia, ISEC-91044, pp. 195-210.

Hashim, W. (1992): "Effect of Flow Oscillations on Friction Factor and Heat Transfer Coefficient in a Channel With Sudden Change in Cross Section", M.S. Thesis, Cleveland State University, Cleveland, OH, March 1992.

Ibrahim, M.B., Tew, R.C. and Dudenhoefer, J.E. (1989): "Two Dimensional Numerical Simulation of a Stirling Engine Heat Exchanger", NASA Technical Memorandum 102057, 1989. Cleveland: Lewis Research Center.

Ibrahim, M.B., Tew, R.C. and Dudenhoefer, J.E. (1990): "Further Two-Dimensional Code Development for Stirling Engine Components", Proc. 25th Intersociety Energy Conversion Engineering Conf., Reno, Nevada, Vol. 6, pp. 329-335.

Gideon D. (1986): "Mean-Parameter Modeling Oscillating Flow", Journal of Heat Transfer, Vol. 108, pp. 513-518, August 1986.

Kaviany, M. (1986): "Some Aspects of Enhanced Heat Diffusion in Fluids By Oscillation", Int. J. Heat Mass Transfer, Vol. 29, No. 12, pp. 2002-2006, 1986.

Kaviany, M. (1990): "Performance of a Heat Exchanger based on Enhanced Heat Diffusion in Fluids by Oscillation: Analysis", Journal of Heat Transfer, Vol. 112, pp. 49-55, February 1990.

Köhler, W.J. (1990): Numerical Prediction of Turbulent Oscillating Flow and Associated Heat Transfer, Ph.D. Thesis, University of Minnesota, Minneapolis,MN, January 1990.

Kurzweg, U.H (1985a): "Enhanced Heat Conduction in Oscillating Viscous Flows Within Parallel-Plate Channels", J. Fluid Mechanics, Vol. 156, pp. 291-300.

Kurzweg, U.H (1985b): "Enhanced Heat Conduction in Fluids Subjected to Sinusoidal Oscillations", Journal of Heat Transfer, Vol. 107, pp. 459-462, May 1985.

Kurzweg, U.H. and Chen, J. (1988): "Heat Transport along an Oscillating Flat Plate", Journal Of Heat Transfer, Vol. 110, pp. 789-790.

Kwan. C.F. (1992): Compressibility Effects on the Periodic Unsteady Flows, M.S. Thesis, Cleveland State University, OH, June 1992.

Ozawa, M. and Kawamoto, A. (1991): "Lumped-Parameter modeling of Heat Transfer Enhanced by Sinusoidal Motion of Fluid", Int. J. Heat Mass Transfer, Vol. 34, No. 12, pp. 3083-3095, 1991.

Patankar, S.V. (1980) : Numerical Heat Transfer and fluid Flow, Hemisphere Publishing Corp., 1980.

Patankar, S.V. and Oseid, K. (1992): "Numerical Prediction of the Heat Transfer in Transitional and Turbulent Oscillatory Flows", Progress Report submitted to NASA Lewis Research Center, August 1992.

Perić, M. and Scheuerer, G. (1989): "CAST—A Finite Volume Method For Predicting Two-Dimensional Flow and Heat Transfer Phenomena", GRS Technische Notiz SRR-89-01, September 1989.

Richardson, E.G. (1928): Proc. Phys. Soc. London, Vol. 40, pp. 206, (1928).

Richardson, E.G. and Tyler, E. (1929): "The Transverse Velocity Gradient Near the Mouths of Pipes in Which an Alternating Continuous Flow of Air is Established", Proc. Phys. Soc. London, Vol. 42, pp. 1-15.

Schlichting, H. (1982): Boundary Layer Theory, 6th. Edition, McGraw-Hill Book Company, New York.

Seume, J., Friedman, G. and Simon, T.W. (1992): "Fluid Mechanics Experiments in Oscillatory Flow", NASA Contractor Report 189128, Vol. I-II, March 1992. Cleveland: Lewis Research Center.

Sexl, T. (1930): "Über den Von E.G. Richardson Entdeckten 'Annulareffekt'", Zeitschrift für Physik, Vol. 61, pp. 185-189.

Simon, T.W. and Seume, J.R. (1988): "A survey of Oscillating Flow in Stirling Engine Heat Exchangers", NASA Contractor Report 82108, March 1988. Cleveland: Lewis Research Center.

Simon, T.W., Ibrahim, M.B., Kannapareddy, M., Johnson, T. and Friedman, G. (1992): "Transition of Oscillatory Flow in Tubes: An Empirical Model for Application to Stirling Engines", Proceedings of the 27th Intersociety Energy Conversion Engineering Conference, August 3-7, San Diego, CA, Vol. 5, pp. 495-502, 1992.

Uchida, S. (1956): "The Pulsating Viscous Flow Superposed on the Steady Laminar Motion of Incompressible Fluid in a Circular Pipe", Zeitschr. Angew. Phys. (ZAMP), Vol. 7, pp. 403-422, 1956.

Watson, E.J. (1983): "Diffusion in Oscillatory Pipe Flow", J. Fluid Mech., Vol. 133, pp. 233-244, 1983.

Yuan, Z. and Dybbs A. (1992): "Oscillating Flow and Heat Transfer in a Stirling Engine Regenerator", HTD-Vol. 193, Fundamentals of Heat Transfer in Porous Media, ASME 1992.

Zhao, L.D., Zhu, G.J., Cao, Y.Z. and Zhu, D.G. (1991) : "Some Aspects of Enhanced Heat Transfer in Laminar Oscillatory Viscous Flows Within Capillary Bundle", 4th International Symposium on Transport Phenomena in Heat and Mass Transfer, July 14-19, Sydney, Australia, Vol. 3, pp. 1046-1057, 1991.

Notre Dame
Dr. Yang
Oscillating Flow
Rig

APPENDIX A

GENERALIZED SYSTEM OF PARTIAL DIFFERENTIAL EQUATIONS SOLVED

In the following equations the parameter n controls the coordinate axes system. The cartesian system can be retrieved by taking n=0 and substituting $r=y$ in the following equations. The axisymmetric coordinate system is retrieved by putting n=1.

$$\frac{\partial U}{\partial x} + \frac{1}{r^n}\frac{\partial}{\partial r}(r^n V) = 0$$

$$\rho\frac{\partial U}{\partial t} + \rho U\frac{\partial U}{\partial x} + \rho V\frac{\partial U}{\partial r} = -\frac{\partial P}{\partial x} + \frac{\partial}{\partial x}\left(\mu\frac{\partial U}{\partial x}\right) + \frac{1}{r^n}\frac{\partial}{\partial r}\left(r^n\mu\frac{\partial U}{\partial r}\right) + \frac{\partial}{\partial x}\left(\mu\frac{\partial U}{\partial x}\right) + \frac{1}{r^n}\frac{\partial}{\partial r}\left(r^n\mu\frac{\partial V}{\partial r}\right)$$

$$\rho\frac{\partial V}{\partial t} + \rho U\frac{\partial V}{\partial x} + \rho V\frac{\partial V}{\partial r} = -\frac{\partial P}{\partial r} + \frac{\partial}{\partial x}\left(\mu\frac{\partial V}{\partial x}\right) + \frac{1}{r^n}\frac{\partial}{\partial r}\left(r^n\mu\frac{\partial V}{\partial r}\right) + \frac{\partial}{\partial x}\left(\mu\frac{\partial U}{\partial r}\right) + \frac{1}{r^n}\frac{\partial}{\partial r}\left(r^n\mu\frac{\partial V}{\partial r}\right) - n\left(2\mu\frac{V}{r^2}\right)$$

$$P = p + \frac{2}{3}\left[\mu\left(\frac{\partial U}{\partial x} + \frac{\partial V}{\partial r} + \frac{V}{r}\right)\right]$$

$$\rho\frac{\partial(C_pT)}{\partial t} + \rho U\frac{\partial(C_pT)}{\partial x} + \rho V\frac{\partial(C_pT)}{\partial r} = \frac{\partial}{\partial x}\left(k\frac{\partial T}{\partial x}\right) + \frac{1}{r^n}\frac{\partial}{\partial r}\left(k\frac{\partial T}{\partial r}\right) + \left(\frac{\partial p}{\partial t} + U\frac{\partial P}{\partial x} + V\frac{\partial P}{\partial r}\right) + \mu\Phi$$

APPENDIX B

DERIVATION OF PRESSURE CORRECTION EQUATION

In the step 3) of the SIMPLE algorithm described in section 5.5.1 it was mentioned that a pressure correction equation is needed to correct the velocities such that the continuity equation. This pressure correction equation is derived from the discretized continuity and momentum equation. The continuity equation (3.1) when discretized with respect to cartesian coordinate system yields:

$$\frac{\rho_P^0-\rho_P}{\delta t}\delta V + m_{x,e} - m_{x,w} + m_{y,n} - m_{y,s} = 0 \qquad \text{(B.1)}$$

eq. (B.1) is nothing but a mass balance over a control volume, substituting for the mass fluxes for the respective CV faces from eq. (5.6), one gets:

$$\frac{\rho_P^0-\rho_P}{\delta t}\delta V + \rho_e U_e \delta y - \rho_w U_w \delta y + \rho_n V_n \delta x - \rho_s V_s \delta x = 0 \qquad \text{(B.2)}$$

Since the velocities U^* and V^* obtained from the solution of the momentum equations in steps 1) and 2) of the SIMPLE algorithm were based on a guessed initial pressure field, the continuity equation (B.2) will not be satisfied yielding a mass source S_m:

$$\frac{\rho_P^0-\rho_P}{\delta t}\delta V + \rho_e U_e^* \delta y - \rho_w U_w^* \delta y + \rho_n V_n^* \delta x - \rho_s V_s^* \delta x = S_m \qquad \text{(B.3)}$$

Here the "*" indicates the newly found velocities from the momentum equations. To eliminate the mass source S_m, velocity corrections need to performed to enforce mass corrections, then the velocity corrected continuity equation becomes by definition:

$$\frac{\rho_P^0 - \rho_P}{\delta t}\delta V + \rho_e(U_e^* + U'_e)\,\delta y - \rho_w(U_w^* + U'_w)\,\delta y \tag{B.4}$$

$$+ \rho_n(V_n^* + V'_n)\,\delta x - \rho_s(V_s^* + V'_s)\,\delta x = 0$$

Subtracting eq. (B.3) from eq. (B.4) yields an equation for the velocity corrections, namely:

$$\rho_e U'_e \delta y - \rho_w U'_w \delta y + \rho_n V'_n \delta x - \rho_s V'_s \delta x = -S_m \tag{B.5}$$

Now the velocity corrections are related to the pressure corrections P'. The discretized momentum equations are used to couple the velocity and pressure. By linearizing the velocity corrections it can be related to the pressure corrections as:

$$U'_e = -\left(\overline{\frac{1}{a_P}}\right)_e (P'_E - P'_P) \tag{B.6}$$

$$U'_w = -\left(\overline{\frac{1}{a_P}}\right)_w (P'_P - P'_W) \tag{B.7}$$

$$V'_n = -\left(\overline{\frac{1}{a_P}}\right)_n (P'_N - P'_P) \tag{B.8}$$

$$V'_s = -\left(\overline{\frac{1}{a_P}}\right)_s (P'_P - P'_S) \tag{B.9}$$

Substituting eqs. (B.6)-(B.9) into equation (B.5) yields the so called pressure correction equation:

$$a_P P'_P = a_W P'_W + a_E P'_E + a_S P'_S + a_N P'_N - S_m \qquad \text{(B.10)}$$

a complete description of the coefficients can be found in Perić and Scheuerer (1989).

This pressure correction equation (B.10) has the same structure as the other discretized equations hence can be solved using the same matrix solver. The boundary conditions for the pressure correction equations are derived from the velocities at the boundary. The way this is achieved is by setting the velocity corrections at the appropriate CV boundary face to be zero.

Since the pressure and velocity are nonlinearly coupled the SIMPLE algorithm diverges if no underrelaxation is employed, in the present code the pressure is corrected by the following equation:

$$P_P^{**} = P_P^{*} + \alpha^P P'_P$$

where α^P is the underrelaxation factor for pressure and is usually in the range 0.2-0.4.